SOOT OXIDATION AND THE MECHANISMS OF OXIDATION-INDUCED FRAGMENTATION IN A TWO-STAGE BURNER FOR ETHYLENE AND SURROGATE FUELS

by

Hossein Ghiassi

A dissertation submitted to the faculty of
The University of Utah
in partial fulfillment of the requirements for the degree of

Doctor of Philosophy

Department of Chemical Engineering

The University of Utah

December 2015

The University of Utah Graduate School

STATEMENT OF THESIS APPROVAL

The thesis of **Hossein Ghiassi**

has been approved by the following supervisory committee members:

JoAnn S. Lighty	, Chair	**09/15/2015** Date Approved
Matti Maricq	, Member	**09/15/2015** Date Approved
Terry Ring	, Member	**09/15/2015** Date Approved
David Lignell	, Member	**09/15/2015** Date Approved
Eric G. Eddings	, Member	**09/15/2015**

and by **Milind Deo** , Chair/Dean of

the Department/College/School of **Chemical Engineering**

and by David B. Kieda, Dean of The Graduate School.

ABSTRACT

Studies on the evolution of soot particle size distributions during the process of soot oxidation were carried out in the two-stage burner by using a Scanning Mobility Particle Sizer (SMPS) for n-butanol/n-dodecane, methyl decanoate/n-dodecane, and ethylene flames. This experimental technique, along with measurements of flame temperature, gas-phase composition, surface functional groups, and soot nanostructure and morphology, allowed for identifying effective parameters during soot oxidation and the mechanisms associated with soot oxidation-induced fragmentation.

The results of increasing n-butanol and methyl decanoate in n-dodecane showed a reduced sooting propensity; however, it did not enhance soot oxidative reactivities. The result of image analysis technique demonstrated a strong dependence of soot oxidation rate on the initial soot nanostructure, whereas oxygen functionalities did not matter as much. The highest soot oxidative reactivity was found for the soot nanostructure with the minimum degree of orderliness. On the other hand, the lowest oxidative reactivity was observed for the soot with the nanostructure composed of large layer planes with either low or zero curvatures.

Soot oxidation-induced fragmentation was studied by using ethylene fuel. The mechanisms of soot oxidation-induced fragmentation were explored by following changes in mobility size, number and concentration, flame temperature, and gas-phase compositions. Results showed that the rate of fragmentation was inversely proportional to the peak temperature, and the onset of fragmentation depended on the presence of aggregates. In addition, two main mechanisms suggested in the literature, (i) aggregate break-up by burning bridges; (ii) primary particle break-up by O_2 diffusion, were tested with the aid of an image analysis technique. The results demonstrated that bridge sites were formed by less-ordered nanostructure, resulting in a faster burning rate, suggesting aggregate fragmentation by this mechanism. The effectiveness factor calculation was used to evaluate the feasibility of primary particle breakup by O_2 internal burning. It was shown the primary particle breakup for particles smaller than 10 nm becomes more probable by decreasing temperature and increasing O_2 partial pressure.

To those who devoted their lives to achieving and expressing values

CONTENTS

CHAPTERS

APPENDICES

NOMENCLATURE

A	Surface area of soot particles per unit volume of gas, [cm^2/cm^3]
Ar	Argon
B	Reactive sites in the basal plane
C_{O2}	Oxygen concentration $(\frac{mol}{cm^2})$
D_e	Effective diffusion $(\frac{cm^2}{s})$
D_K	Knudsen diffusion coefficient $(\frac{cm^2}{s})$
Dp	Particle size diameter, [nm]
d_j	Junction diameter, [m]
$\overrightarrow{d}$	Unique unit vector
He	Argon
k_{g0}	Gas thermal conductivity, [$W/m \cdot K^2$]
k'	Rate constant $(\frac{cm^3}{cm^2.s})$
k	Rate constant $(\frac{1}{s})$
Le	Lewis number
m	Total soot mass per unit volume of gas, [$grams/cm^3$]
M	Oxygen molecular weight
M_T^2	Modified Thiele module

Nu_j	Junction Nusselt number
O_2	Molecular oxygen
OH	Hydroxyl radical
O	Oxygen radical
P_{O2}	O_2 partial pressure, [atm]
P_{OH}	OH* partial pressure, [atm]
R	Radius of soot particle
R_g	Universal gas constant
r_p	Effective pore space
$\vec{r_i}$	Vector pointing from polar symmetry poles
S_{BET}	BET surface $(\frac{m^2}{gr})$
S_{2N}	Nematic symmetry
S_{2P}	Polar symmetry
t	Residence time of soot into the flame, [sec]
t_D	Diffusion time scale (s)
t_r	Reaction time scale (s)
T	Temperature, [K]
Tg	Combustion gas temperature, [K]
T_j	Thermocouple junction temperature, [K]
$\vec{u}_i$	Direction unit vector
V	Unburned gas velocity, [cm/sec]
W	Specific oxidation rate, [g/cm^2·sec]

GREEK SYMBOLS

τ	Tortuosity
γ	Soot porosity
ρ	Soot density
η	Effectiveness factor
Γ_{OH}	Fraction of collisions of OH
$\varnothing_1$	Equivalence ratio in the first burner
$\varnothing_{\mathrm{Overall}}$	Overall equivalence ratio
ϑ	Cold gas velocity, [cm/s]
ϵ_j	Junction/bead emissivity
α_i	Angle between the fringe orientational vector and mean orientational vector
σ	Stefan-Boltzmann constant, [W/m^2·K4]
N_t	Total number concentration, [#/cm^3]

LIST OF ABBREVIATIONS

DCM	Dichlorométhane
DMA	Differential Mobility Analyzer
C/O	Carbon to Oxygen Ratio
DR	Dilution Ratio
FPNP	Fine Particle Number Percentage
FT	Fischer-Tropsch fuel
GC	Gas Chromatography
GRI	Gas Research Institute
HAB	Height Above the Burner
HACA	Hydrogen Abstraction and Acetylene Addition
HR-TEM	High Resolution TEM
MS	Mass Spectrometry
NSC	Nagle and Strickland-Constable
PSDs	Particle Size Distributions
PAHs	Polycyclic Aromatic Hydrocarbons
TEM	Transmission Electron Microscopy
TPD	Thermocouple Particle Densitometry
ST	Sooting Tendency
STP	Standard Temperature (298.15 K) and Pressure (1atm)

SS	Sooting Stability
SMPS	Scanning Mobility Particle Sizer
SMC	Soot Mass Concentration
TGA	Thermogravimetric Analyzer
UCPC	Ultrafine Condensation Particle Counter
UPNP	Ultrafine Particle Number Percentage
XPS	X-ray Photoelectron Spectroscopy

AKNOWLEDGEMENTS

I begin by expressing my most sincere gratitude and appreciation to Dr. Lighty for her encouragement and support throughout my graduate studies. She allowed me the freedom to initiate new ideas, and was always there to lend a listening ear and provide constructive feedback. Her technical and editorial advice was invaluable to the completion of this dissertation.

I also express my heartfelt appreciation to my advisory committee, Dr. Maricq, Dr. Eddings, Dr. Ring, and Dr. Lignell, for their critical comments and guidance on my research.

I would like to express my gratification to Dr. Jaramillo, who helped me with the experiment in the lab, and also for her invaluable advice during the research. I would also like to thank Dana Overaker for his assistance in ordering and buying lab materials, as well as equipment repair and maintenance.

I would like to appreciate my wife for her support, encouragement, patience, and companionship that have turned my journey through graduate school into a pleasure. I am deeply thankful to my parents and my sisters for their faith in me and for encouraging me to be ambitious. Their love and continuous encouragement has always given me the strength to tackle challenges.

This material is based upon work supported by the National Science Foundation under Grant No. 1133480. The author gratefully acknowledges their support.

CHAPTER 1

INTRODUCTION

1.1 Effect of oxygenated fuels on soot emission

Soot emissions from diesel engines continue to be a serious environmental concern which has led to stricter emissions regulations [67]. To meet these increasingly stringent regulations, a number of strategies and techniques have been developed, such as after-treatment processes, engine modifications, and fuel reformulation. Addition of oxygenates has always been considered as an effective way to suppress the soot formation and to ultimately produce a soot which can be more readily oxidized [6,14,26,30,56,61,63]. There have been many studies on the effect of oxygenated fuels on the soot formation [7,14,29,30,47]. Testing a wide variety of oxygenated fuels has shown a substantial reduction in PM exhaust emissions [61]. Miyamoto et al. [36] tested several oxygenates and concluded that the soot emissions correlate with the oxygen content of the fuel.

Oxygenated fuels derived from renewable sources have recently drawn much attention due to worldwide concerns about global warming and petroleum supply shortages in the near future. Alcohols such as ethanol [4,23,44] , methanol [24,54,66], propanol [3,27], and butanol [2,17,35] can be produced from renewable sources. Propanol and butanol are becoming increasingly attractive as additives or alternative fuels compared to ethanol and methanol, because they are less prone to water contamination, are less corrosive, and have a better blending stability and lubricity [2,33,58]. However, n-butanol can potentially be produced from a renewable source in a higher yield [2]. Some studies have investigated the combustion of alcohols such as n-butanol and presented a detailed chemical kinetic mechanism [5,13,25,38,52,53]. One of them has been proposed by Esarte et al. [18] based on theoretical calculations using a gas-phase detailed chemical kinetic model. Their analysis of the reaction pathways undertaken by the main reactants to form gas and soot products helps to understand the fuel decomposition processes which lead to form PAHs. They showed that n-butanol undergoes dehydration, decomposition, and dehydrogenation to form PAH precursors and oxygenated intermediates that finally oxidize to CO. However, the exact mechanisms by which oxygenated fuels impact the reactivity of soot particles are not thoroughly understood. Although much progress has been made in the recent past, there still remain many unanswered questions.

Biodiesel is an alternative energy source and could be a substitute for petroleum-based diesel fuel [10]. Biodiesel is commonly referred to as methyl esters of vegetable oil. Westbrook et al. [67] showed how different oxygenates, ester structures in particular, can have different soot-suppression efficiencies due to differences in the molecular structure of oxygenated species. They concluded that both oxygen atoms in esters remain bound to the same carbon atom and are more likely to form CO_2. When oxygen atoms are farther apart, each of them remains bonded to a different carbon, preventing these carbons from becoming available for soot precursors. Westbrook's results have been supported by other studies [12,57,59,60,67].

Although many studies have been devoted to identify the mechanism of soot formation by using alcohols or esters, there have been few investigations of the influence of these fuels on soot oxidative reactivity. The exact mechanisms by which oxygenated fuels impact the reactivity of soot particles are not thoroughly understood and nanostructures may account for that.

1.2 Soot oxidation and fragmentation

Numerous studies, both experimental and numerical, have been devoted to better understand the combustion processes in order to improve their efficiency and to reduce their impact on human health and the environment. The majority of these studies have been focused on the mechanisms of soot formation such as PAHs formation, particle inception, and particle growth. However, the level of soot emission from combustion systems depends on the competition between soot formation and oxidation process. Soot oxidation plays a key role to determine the particle emissions. High temperature oxidation takes place inherently in flames after the formation of soot [28,31,48]. Many researchers have shown that OH is the principle soot surface oxidant in flame environments, where O_2 concentration is relatively small [19,21,40,50,51]. Two typical kinetic expressions to account for the soot oxidation via O_2 and OH have been proposed by Nagle-Strickland-Constable (NSC) [39] and Neoh et al. [41], respectively. The semi-empirical model by NSC is most-commonly introduced to describe high temperature combustion. Two types of active sites, a more reactive type A and less reactive type B, are proposed. Thermal rearrangement will convert type A to type B. Soot oxidation by OH is described through collision efficiency, suggested by Fenimore et al. [19].

Motivated by this suggestion, Neoh et al. [42,43] used a two-stage burner to study the oxidation of soot under the condition studied (1575-1865°K; 1 atm; ~ 0.05 mole fraction O_2) with the collision efficiency of 0.1 to 0.4 carbon atoms removed per collision.

Oxidation is responsible for the soot burn-out; however, soot particles can be attacked by oxidant species such that the structure can be weakened and the particles can break apart. Oxidation-induced fragmentation of particles can occur if the oxidizing species can remove C atoms from a weak point causing the break-up of larger structures into the smaller ones. In other terms, oxidation-induced fragmentation can be seen as an unintended but inevitable secondary result of oxidation. A fragmentation event occurs after the removal of material condensed from the gas-phase or added by surface reactions, which fills the space between particles. For the first time, this process was reported by Neoh et al. [43] and was named oxidation-induced fragmentation. After Neoh's work, other studies also reported their observation of soot fragmentation [9,16,21,49,68]. Since the oxidation process competes with formation and growth of soot particles, this overlapping makes the study of oxidation-induced fragmentation difficult. The two-stage burner used in Sarofim's group and later by Lighty's group helps to isolate the oxidation process, and thus, evidence embedded phenomena such as oxidation-induced fragmentation. Recently, soot fragmentation has been studied by Echavarria et al. [9,16] in a two-stage burner. They used a scanning mobility particle sizer (SMPS) to obtain particle size distributions (PSDs) to characterize fragmentation in ethylene flame. Their measurements of soot size distribution and number concentration as a function of HAB showed a decrease in particle mean diameter and a significant increase in number concentration (fragmentation) in the region where O_2 concentration decreased. It has been shown that during oxidation of soot particles in high temperature environments, fragmentation of aggregates and even fragmentation of primary particles may occur [9,43]. The lack of data has been a barrier in identifying appropriate mechanisms for incorporation into simulations which predict particle size distributions. The evolution of particle size distribution (PSD) obtained with this experimental setup has constituted a benchmark for the modelers.

1.3 The effect of soot nanostructure on the oxidative reactivity

Nanostructure refers to the physical characteristics and arrangements of carbon plane layers which identify the dimensions and relative orientation and curvature of plane layers. It can provide useful information such as the relative number and accessibility of potential reactive sites [28]. In such an analysis, the surface of soot particles is assumed to resemble an edge of a large PAH molecule, covered with *C-H* bonds [20]. PAHs are stacked together to form nanocrystallites and finally to form soot structure [46]. The larger size of the PAHs in soot results in fewer reactive edge sites due to higher *C/H* ratio [15,34].

Increasing the concentration of reactive cyclic or saturated aliphatics on soot surface can bring lower *C/H* ratios and higher reactivity during soot oxidation process [8,62]. Two types of carbon can be specified in soot particles: 1) the carbon on the edge sites, which is more accessible for oxidizing agents such as O_2 and OH; and 2) the carbon on the basal plane, which has a negligible reactivity, on the order of 100-1000 0.01-0.001 times that of the edge carbon [74, 75]. Carbons on the edge sites contribute to reactions because of the availability of unpaired sp^2 electrons, while carbon atoms in basal planes have only shared π electrons accessible to bond formation [40]. In addition to the layer size and the location of *C-H* bond, the curvature of the layers can also affect their reactivity. Curvatures can be the result of having 5- membered rings in graphene layers [32]. Curvature can affect the soot reactivity by imposing bond strain on the C-C bonds. As a result, these bonds are weakened and more easily subject to oxygen attack [11]. Differences at soot nanostructures, i.e., curvature, orientation of the plane layers, and the interlayer spacing, imply the availability of active sites and subsequently the oxidative reactivity of soot particles [1,22,64]. Studies have shown that there is a relationship between nanostructure and soot reactivity [22,45,46,55,65]. Vander Wal and Tomasek [64] performed HR-TEM on soot nanostructure in order to check for the effect of the initial soot structure on soot oxidative reactivity and changes therein upon oxidation. They concluded that soot oxidative reactivities depend on nanostructures and nanostructures depend on the flame conditions and fuel source.

1.4 Objectives of this work

Soot emissions from combustion systems such as industrial flames, auto engines, etc. have been shown to have adverse effects on human health and the environment. A determinant role for the particle emissions is played by the oxidation processes. The proposed work is an in-depth investigation of soot oxidation and fragmentation by using the two-stage burner. The proposed work has the following objectives:

i) Use a two-stage burner to study the sooting behavior (sooting tendency and oxidative reactivity) of two important oxygenated fuels, n-butanol as an alcohol and methyl decanoate as a surrogate for biodiesel fuels.

ii) Apply a novel image analysis framework extract the soot structural information in order to correlate soot oxidative reactivity with soot nanostructure.

iii) Evaluate the mechanisms hypothesized in the literature for soot oxidation-induced fragmentation by analyzing HRTEM images

iv) Explore the parameters that affect soot oxidation-induced fragmentation by following changes in mobility size, flame temperature, and gas-phase compositions.

1.5 Organization of the dissertation

This dissertation includes a series of publications, namely Chapters 3-6, which are linked as described below.

In Chapter 3, the impacts of increasing *n*-butanol as an oxygenated compound on the formation and oxidative reactivity of soot were studied. A two-stage burner was used to characterize the oxidation of soot for different mixtures and to isolate the soot oxidation from the soot formation process. A scanning mobility particle sizer (SMPS) was used to measure the soot particle size distributions (PSDs) at different heights in the flame during oxidation, and soot oxidation rates were estimated by further analyzing the PSDs. A novel image analysis was used to quantify soot nanostructure and to reveal the effect of structural order on the soot oxidative reactivity.

In Chapter 4, the oxidative reactivity of soot derived from methyl decanoate/n-dodecane (biodiesel/diesel surrogate) was explored. PSDs were also measured and were compared to that of n-butanol/n-dodecane (alcohol/diesel surrogate). Temperature profiles were measured along the centerline of the flame for the fuel mixtures. Gaseous species such as O_2, CO, CO_2, and H_2 were measured by online gas chromatography and used to validate a detailed kinetic model which predicts the OH concentration in the secondary flame. Experimental oxidation rates were calculated by further analysis of PSDs. The conventional models (particularly Neoh and NSC) were computed and compared with the experimental oxidation rates.

In Chapter 5, soot oxidation-induced fragmentation is studied. Two current fragmentation mechanisms, i) primary particle break-up, and ii) aggregate break-up, are examined by the aid of image analysis technique. In order to evaluate the aggregate break-up, high-resolution transmission electron microscopy (HR-TEM) images were processed by an image analysis framework designed for extracting the symmetry parameters (nematic and polar order parameters) to quantify the soot nanostructure. In addition, the feasibility of internal burning in primary particles was tested through an analysis of intraparticle diffusion. In order to estimate the particle tortuosity, the actual distance travelled by O_2 molecules toward the center of a particle was computed using these images. The effective pore width was also estimated by using the random walk simulation. To compare the diffusion time with the reaction time, the effectiveness factor was calculated, with previously determined lognormal distributions of particle tortuosity and pore width as inputs.

In Chapter 6, experiments in a two-stage burner, with ethylene as the fuel, were conducted to further understand the mechanisms associated with the fragmentation of soot particles. Experiments were grouped in the following three categories, based on the main objective of the corresponding experiment: (i) the effect of different inert gases, *Ar*, *He*, N_2 (ii) the effect of an increase in N_2 dilution and O_2 concentration (iii) and the effect of particle mobility size on the fragmentation. Temperature profiles, PSDs, and gas species were measured and reported. Soot oxidation induced fragmentation was identified by observable increase of particles smaller than 10 nm. Also, a role for *OH* oxidation during fragmentation was postulated by probability analysis, since fragmentation was experimentally shown to continue in the region of the flame where *OH* was present.

1.6 References

[1] M. Alfè, B. Apicella, R. Barbella, J.N. Rouzaud, A. Tregrossi, A. Ciajolo, et al., Proceedings of the Combustion Institute. 32 (2009) 697–704.

[2] S. Atsumi, T. Hanai, J.C. Liao, Nature. 451 (2008) 86–89.

[3] S. Atsumi, J.C. Liao, Applied and Environmental Microbiology . 74 (2008) 7802–7808.

[4] P. Binod, R. Sindhu, R.R. Singhania, S. Vikram, L. Devi, S. Nagalakshmi, et al., Bioresource Technology. 101 (2010) 4767–4774.

[5] G. Black, H.J. Curran, S. Pichon, J.M. Simmie, V. Zhukov, Combustion and Flame. 157 (2010) 363–373.

[6] M. Boot, P. Frijters, C. Luijten, B. Somers, R. Baert, A. Donkerbroek, et al., Energy & Fuels. 23 (2008) 1808–1817.

[7] K.I. Burshaid, M.A. Hamdan, Energy Conversion and Management. 65 (2013) 751–754.

[8] J.P. Cain, P.L. Gassman, H. Wang, A. Laskin, Physical Chemistry Chemical Physics. 12 (2010) 5206–5218.

[9] Carlos A. Echavarria, I.C. Jaramillo, A.F. Sarofim, J.S. Lighty, C.A. Echavarria, Combustion and Flame. 159 (2012) 2441–2448.

[10] C. Carraretto, A. Macor, A. Mirandola, A. Stoppato, S. Tonon, Energy (Amsterdam, Netherlands). 29 (2004) 2195–2211.

[11] I.W. Chiang, B.E. Brinson, A.Y. Huang, P.A. Willis, M.J. Bronikowski, J.L.

Margrave, et al., The Journal of Physical Chemistry B. 105 (2001) 8297–8301.

[12] P. Dagaut, S. Gail, M. Sahasrabudhe, Proceedings of the Combustion Institute. 31 (2007) 2955–2961.

[13] P. Dagaut, S.M. Sarathy, M.J. Thomson, Proceedings of the Combustion Institute. 32 (2009) 229–237.

[14] A.J. Donkerbroek, M.D. Boot, C.C.M. Luijten, N.J. Dam, J.J. ter Meulen, Combustion and Flame. 158 (2011) 525–538.

[15] J.B. Donnet, Carbon. 20 (1982) 267–282.

[16] C.A. Echavarria, I.C. Jaramillo, A.F. Sarofim, J.S. Lighty, Proceedings of the Combustion Institute. 33 (2011) 659–666.

[17] J.T. Ellis, N.N. Hengge, R.C. Sims, C.D. Miller, Bioresource Technology. 111 (2012) 491–495.

[18] C. Esarte, M. Abián, Á. Millera, R. Bilbao, M.U. Alzueta, Energy. 43 (2012) 37–46.

[19] C.P. Fenimore, G.W. Jones, Journal of Physical Chemistry A. 71 (1967) 593–597.

[20] M. Frenklach, Phys. Chem. Chem. Phys. 4 (2002) 2028–2037.

[21] A. Garo, J. Lahaye, G. Prado, Symposium (International) on Combustion. 21 (1988) 1023–1031.

[22] H. Ghiassi, P. Toth, J.S. Lighty, Sooting Behaviors of n-Butanol and n-Dodecane Blends, in: ISBN: 978-1-62748-842-6 8th US National Combustion Meeting, 2013.

[23] C.S. Gong, N.J. Cao, J. Du, G.T. Tsao, Advances in Biochemical Engineering/Biotechnology. 65 (1999) 207–241.

[24] R.P. Gupta, D.K. Tuli, R.K. Malhotra, Chemical Industry Digest. 24 (2011) 86–93.

[25] M.R. Harper, K.M. Van Geem, S.P. Pyl, G.B. Marin, W.H. Green, Combustion and Flame. 158 (2011) 16–41.

[26] Z. Huang, H. Lu, D. Jiang, K. Zeng, B. Liu, J. Zhang, et al., Energy & Fuels. 19 (2005) 403–410.

[27] R. Jain, Y. Yan, Microbial Cell Factories. 10 (2011) 97.

[28] I.C. Jaramillo, C.K. Gaddam, R.L. Vander Wal, C.-H. Huang, J.D. Levinthal, J.S. Lighty, Combustion and Flame. (2014) -.

[29] T. Kitamura, T. Ito, J. Senda, H. Fujimoto, JSAE Review. 22 (2001) 139–145.

[30] R.J.H. Klein-Douwel, A.J. Donkerbroek, A.P. van Vliet, M.D. Boot, L.M.T. Somers, R.S.G. Baert, et al., Proceedings of the Combustion Institute. 32 (2009) 2817–2825.

[31] B.F. Kock, B. Tribalet, C. Schulz, P. Roth, Combustion and Flame. 147 (2006) 79–92.

[32] H.W. Kroto, J.R. Heath, S.C. O'Brien, R.F. Curl, R.E. Smalley, Nature (London, United Kingdom). 318 (1985) 162–163.

[33] R. Lemaire, E. Therssen, P. Desgroux, Fuel. 89 (2010) 3952–3959.

[34] F. Marcuccilli, P. Gilot, B. Stanmore, G. Prado, Symposium (International) on Combustion, [Proceedings]. 25 (1994) 619–626.

[35] M. Mascal, Biofuels, Bioproducts & Biorefining. 6 (2012) 483–493.

[36] N. Miyamoto, H. Ogawa, M.N. Nabi, International Journal of Engine Research. 1 (2000) 1468–0874.

[37] V.N. Mochalin, O. Shenderova, D. Ho, Y. Gogotsi, Nature Nanotechnology. 7 (2012) 11–23.

[38] J.T. Moss, A.M. Berkowitz, M.A. Oehlschlaeger, J. Biet, V. Warth, P.-A. Glaude, et al., The Journal of Physical Chemistry A. 112 (2008) 10843–10855.

[39] J. Nagle, R.F. Strickland-Constable, Proc. Conf. Carbon, 5th, Univ. Park, Penna.,. 1 (1961) 154–164.

[40] K.G. Neoh, Soot burnout in flames, Massachusetts Institute of Technology, 1981.

[41] K.G. Neoh, J.B. Howard, A.F. Sarofim, Soot oxidation in flames., in: Part. Carbon: Form. Combust., [Proc. Int. Symp.], Plenum, 1981: pp. 261–282.

[42] K.G. Neoh, J.B. Howard, A.F. Sarofim, Particulate Carbon Formation During Combustion, Plenum Press, New York, 1981.

[43] K.G. Neoh, J.B. Howard, A.F. Sarofim, Effect of Oxidation on the Physical Structure of Soot, in: Twentieth Symposium (International) on Combustion, The Combustion Institute, Pittsburgh, 1985: pp. 951–957.

[44] M. Ni, D.Y.C. Leung, M.K.H. Leung, International Journal of Hydrogen Energy. 32 (2007) 3238–3247.

[45] A.B. Palotas, L.C. Rainey, C.J. Feldermann, A.F. Sarofim, J.B. Vander Sande, Microscopy Research and Technique. 33 (1996) 266–278.

[46] A.B. Palotas, L.C. Rainey, A.F. Sarofim, J.B. Van der Sande, P. Ciambelli, Energy & Fuels. 10 (1996) 254–259.

[47] P. Pepiot-Desjardins, R. Pitsch, H.; Malhotra, S.R. Kirby, A.L. Boehman, Combustion and Flame. 154 (2008) 191–205.

[48] L.M. Pickett, D.L. Siebers, Combustion and Flame. 138 (2004) 114–135.

[49] R. Puri, T.F. Richardson, R.J. Santoro, R.A. Dobbins, Combustion and Flame. 92 (1993) 320–323.

[50] R. Puri, R.J.. Santoro, K.C. Smyth, Combustion and Flame. 97 (1994) 125–144.

[51] P. Roth, O. Brandt, S. Von Gersum, Symposium (International) on Combustion, [Proceedings]. 23 (1990) 1485–1491.

[52] S.M. Sarathy, M.J. Thomson, C. Togbé, P. Dagaut, F. Halter, C. Mounaim-Rousselle, Combustion and Flame. 156 (2009) 852–864.

[53] S.M. Sarathy, S. Vranckx, K. Yasunaga, M. Mehl, P. Oßwald, W.K. Metcalfe, et al., Combustion and Flame. 159 (2012) 2028–2055.

[54] J. Schrader, M. Schilling, D. Holtmann, D. Sell, M. Villela Filho, A. Marx, et al., Trends in Biotechnology. 27 (2009) 107–115.

[55] J. Song, M. Alam, A.L. Boehman, U. Kim, Combustion and Flame. 146 (2006) 589–604.

[56] J. Song, K. Cheenkachorn, J. Wang, J. Perez, A.L. Boehman, P.J. Young, et al., Energy & Fuels. 16 (2002) 294–301.

[57] J. Song, V. Zello, A.L. Boehman, F.J. Waller, Energy & Fuels. 18 (2004) 1282–1290.

[58] E. Sukjit, J.M. Herreros, K.D. Dearn, R. García-Contreras, A. Tsolakis, Energy. 42 (2012) 364–374.

[59] J.P. Szybist, A.L. Boehman, D.C. Haworth, H. Koga, Combustion and Flame. 149 (2007) 112–128.

[60] C.A. Taatjes, N. Hansen, A. McIlroy, J.A. Miller, J.P. Senosiain, S.J. Klippenstein, et al., Science (Washington, DC, United States). 308 (2005) 1887–1889.

[61] D.R. Tree, K.I. Svensson, Progress in Energy and Combustion Science. 33 (2007) 272–309.

[62] A. Violi, Combustion and Flame. 139 (2004) 279–287.

[63] R.L. Vander Wal, C.J. Mueller, Energy & Fuels. 20 (2006) 2364–2369.

[64] R.L. Vander Wal, A.J. Tomasek, Combustion and Flame. 134 (2003) 1–9.

[65] R.L. Vander Wal, A.J. Tomasek, Combust. Flame. 136 (2004) 129–140.

[66] Z. Wang, X. Wang, A method for producing methanol biomass oil from rice husk., 2014.

[67] C.K. Westbrook, W.J. Pitz, H.J. Curran, J. Phys. Chem. A. 110 (2006) 6912–6922.

[68] F. Xu, A.M. El-Leathy, C.H. Kim, G.M. Faeth, Combustion and Flame. 132 (2003) 43–57.

CHAPTER 2

EXPERIMENTAL METHODS AND TECHNIQUES

2.1 Two-stage burner

A two-stage burner designed by Neoh et al. [1], and improved by Lighty and coworkers [2–4], was used to study the soot oxidation. In flames, oxidation is strictly coupled with the formation process, resulting in difficulty in studying soot oxidation. The purpose of the two-stage burner was to isolate soot oxidation from soot formation. Soot was generated in a fuel-rich premixed flame, which served as the first stage. The soot was then burned in a secondary, premixed burner. In the first-stage burner, air and fuel were added to the bottom of a 2" ID stainless steel chamber under a fuel-rich condition. Flame was stabilized over a tube bundle through which the mixture passes in laminar flow (see Figure 2.1). The result of incomplete combustion in the first stage was the formation of soot and some gas species mainly composed of H_2, O_2, CO, CO_2, N_2, and H_2O. The soot-laden combustion gases were mixed with the secondary oxidizer stream in the pre-oxidation chamber.

The secondary burner and pre-oxidation chamber had multiple purposes: efficient mixing of the soot-laden combustion gases with the secondary oxidizer stream to control the stoichiometry and temperature of the secondary flame; generation of a uniform flow

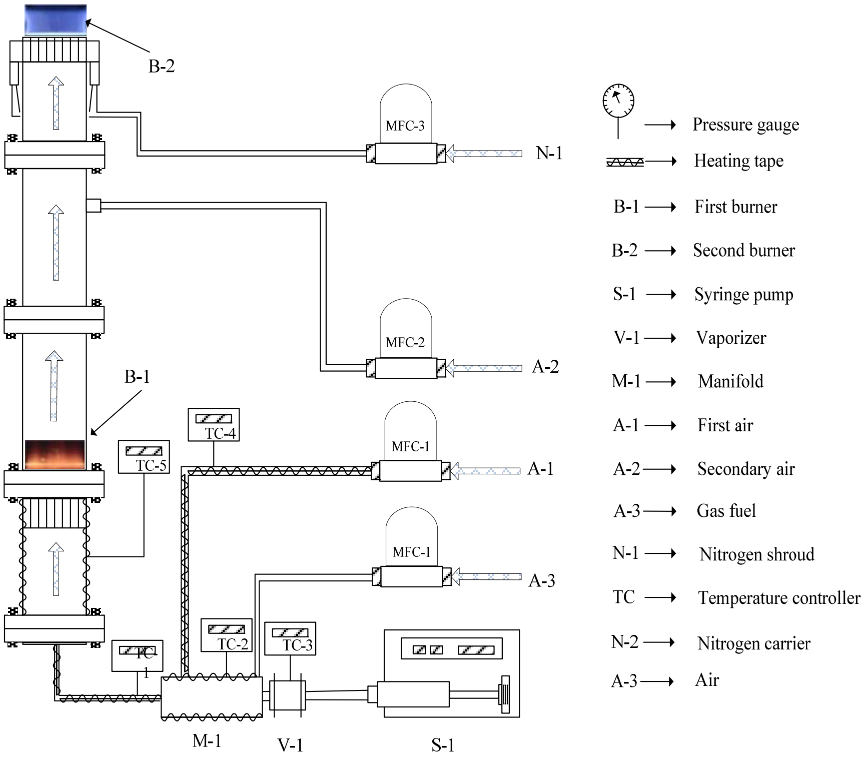

Figure 2.1. Schematic of the two-stage burner

of combustion reactants to the burner; and, oxidation of the soot from the first-stage burner. The flat temperature profiles across the burner reported by Echavaria et al. [5] confirms that the efficient mixing in the pre-oxidation chamber resulted in the flame uniformity across the burner. Similar to the first burner, the secondary flame was stabilized over a tube bundle and shielded from atmospheric interference using a nitrogen shroud. The equivalence ratio was simply determined in the first burner as follows,

$$\Phi_{first\ burner} = \frac{\frac{Fuel}{Air1}}{\frac{Fuel}{Stochiometrc\ Air}} \qquad (2.1)$$

In order to determine the equivalence ratio of the secondary burner, the composition and flowrate of gases fed into the secondary burner need to be known. This means that we need to accurately know the result of the combustion in the first burner. Because of the complexity in determining this information, the overall equivalence ratio is defined as follows,

$$\Phi_{overall} = \frac{\frac{Fuel}{Air1 + Air2}}{\frac{Fuel}{Stochiometrc\ Air}} \qquad (2.2)$$

where Air 1 and Air 2 are the amounts of air injected through the first and secondary ports, respectively. This helps to determine the amount of the secondary oxidizer in terms of the fuel introduced to the first burner.

For liquid fuels (Chapter 3 and 4), a vaporizer was first used to evaporate the liquid stream, then, it was mixed with the preheated air. Experiments ranging from C/O = 0.7 to C/O = 0.56 were run for atmospheric-pressure n-butanol/n-dodecane and methyl decanote/n-dodecane. Table 2.1 gives the experimental conditions for the experiment in Chapter 3 and 4. The regular air was used in the first and second burner. For gas fuels such as ethylene used in Chapter 6, the fuel stream was mixed directly with air at room temperature. The C/O ratio for the first 5 flames was 0.66, while it was 0.60 for the last case. Table 2.2 summarizes it for Chapter 6. The composition of the secondary air for this set of experiment was different. In each chapter, experimental conditions are explained in detail.

Table 2.1. Experimental conditions for flames studied in Chapter 3 and 4.

#	Fuel	$\emptyset_1^a$	$\emptyset_{\mathrm{Overall}}^b$	$\vartheta^c(\frac{cm}{s})$	C/O
C1	30% n-butanol/ 70% n-dodecane	2.2	1.1	3.5	0.7
C2	60% n-butanol/ 40% n-dodecane	2.2	1.1	3.5	0.68
C3	30% methyl decanote/ 70% n-dodecane	1.85	1.05	4.5	0.6
C4	30% methyl decanote/ 70% n-dodecane	1.85	1.05	6	0.6
C5	60% methyl decanote/ 40% n-dodecane	1.76	1	6	0.56

Table 2.2. Experimental conditions for flames studied in Chapter 6. Ethylene was used as fuel.

#	$\emptyset_1^a$	$\emptyset_{\mathrm{Overall}}^b$	$\vartheta^c(\frac{cm}{s})$	Secondary oxidizer composition
Case 1 (base case)	1.98	0.9	3.77	21%O_2–79%N_2
Case 2	1.98	0.9	3.77	21%O_2–79%Ar
Case 3	1.98	0.9	3.77	21%O_2–79%He
Case 4	1.98	0.9	3.77	60%O_2–40%N_2
Case 5	1.98	1.15	3.77	21%O_2–79%N_2
Case 6	1.80	1.10	3.77	21%O_2–79%N_2

[a] Equivalence ratio in the first burner

[b] Overall Equivalence ratio

[c] Cold gas velocity, cm/s (STP)

2.1.1 Fuel feeding system

The fuel feeding system is designed as illustrated in Figure 2.2. The liquid-fuel mixture was injected into the vaporizer (V-1) using a syringe pump (KDS-410). Vaporized fuel was mixed with preheated air in the manifold and then fed into the bottom of the first-stage burner. The temperature of the vaporizer was maintained by using a band heater. The lines and manifold were wrapped with heating elements and their temperature was controlled by a controller. The operating temperature for n-butanol/n-dodecane and methyl decanoate/n-dodecane mixtures was kept at 500 F. For gas fuel (ethylene in this work), Brooks 5850E mass flow controllers was used. No preheating of gas fuel was applied. Complete mixing occurred by passing fuel and air mixtures through the manifold and premixed chamber. The vaporizer was designed for reliable liquid vaporization, specifically for vaporizing liquid hydrocarbons. Direct injection vaporizer system in the designed vaporizer helps to overcome the many limitations of conventional vapor delivery systems. More details of the vaporizer system are given in Appendix A.

.

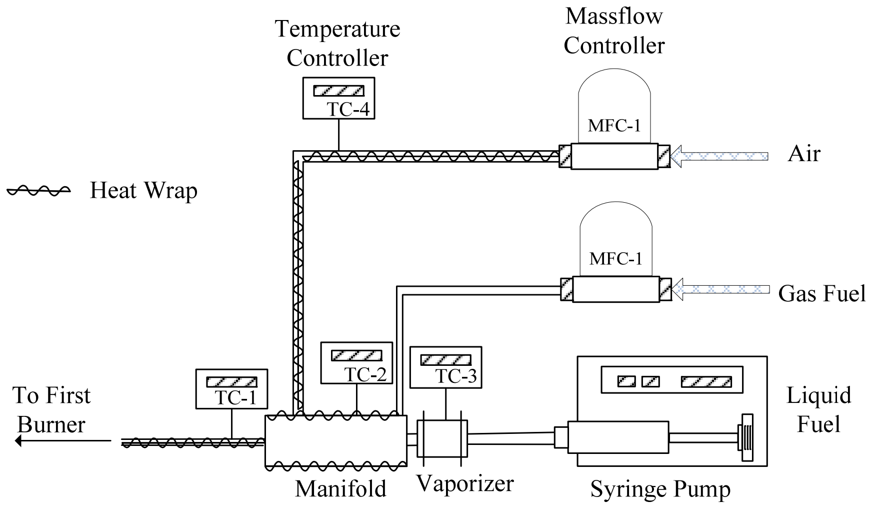

Figure 2.2. Fuel feeding system designed to handle either gas or liquid fuels

2.2 Temperature measurement

Bare wire thermocouples have a very good response time and are less intrusive as compared to the sheathed thermocouples [6]. In this study, the flame temperature was measured along the centerline of the flame by using an uncoated 0.2032-mm Pt/Rh 70%/30% thermocouple (Type B). The thermocouple was inserted into the flame using a fast insertion mechanism. Figure 2.3 shows the structure used to support the thermocouples. It consisted of two high temperature ceramic tubes attached to the heads of two bolts. One of the bolts was tightened, while the other was free to rotate. Since thermal expansion may cause the thermocouple junction sagged downwards, a spring stretched between the ends of the tubes squeezed them together. Temperature measurement by thermocouples is prone to errors due to conduction and radiation losses and therefore has to be corrected for precise measurement [7].

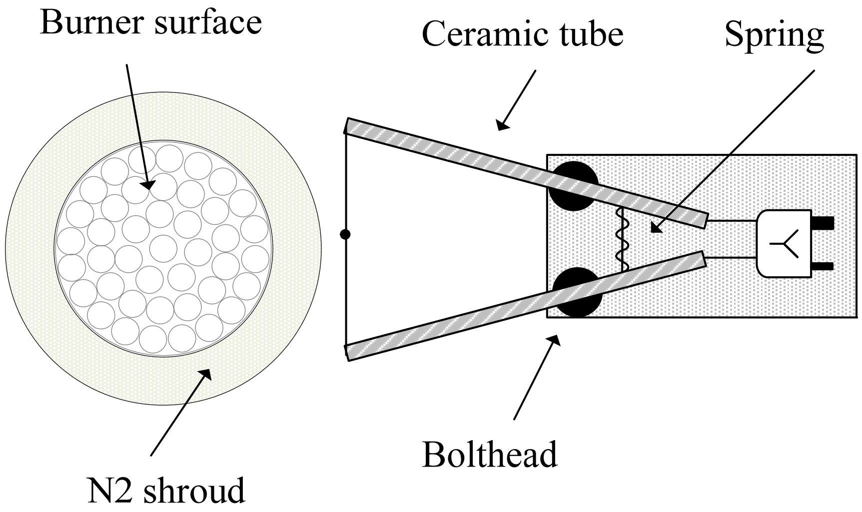

Figure 2.3. Schematic of the thermocouple arrangements

When a thermocouple is inserted into a soot containing flame, particles will deposit on the junction and increase both its emissivity and diameter resulted in greatly increase the error in a temperature measurement. The transient response of the thermocouple was recorded at a sampling rate of 40 samples per second. The radiation correction for the temperature was similar to that of McEnally et al. [8]. Details on the radiation correction across the burner are presented in Appendix B.

2.3 Gas species measurement and modeling

2.3.1 Gas species measurement by GC

The evolution of the combustion gas-phase species was isokinetically sampled by a system involving a water-cooled probe coupled to MAK 10 Sample Gas Conditioners, as illustrated in Figure 2.4.

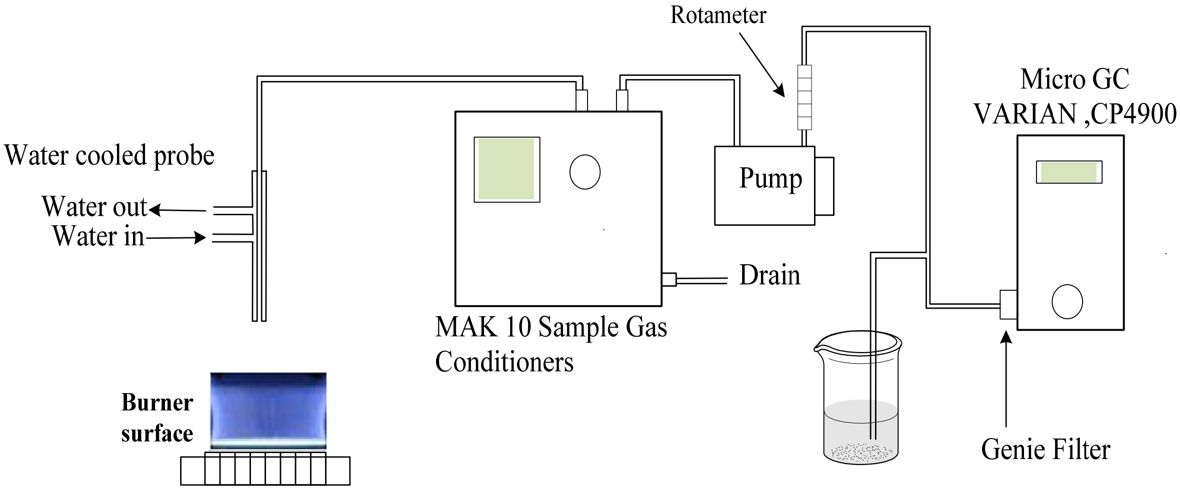

Figure 2.4. Micro GC and sampling probe

The role of MAK 10 was to continuously dehumidify gas sample stream and separate condensable liquids and soot particles. An air pump was used for feeding the GC with a gas sample stream. A rotameter was used in the sampling line to adjust the flow rate of the sampling gas. Since flames contained soot particles in the range of a few nanometers, there was a possibility of escaping ultrafine particles form MAK 10. In order to protect GC columns from these ultrafine particles, the sample stream first passed through the Genie filter (model 101 PS). The micro-GC, VARIAN, CP-4900 was used to analyze the gas sample from the flames. The GC itself is equipped with an internal pump to draw an adequate amount of sample into the columns. Since the external air pump continuously provided gas samples with a flow rate higher than what GC needed, the remainder of the sample was removed via the split vent line. The end of the vent line was placed into a beaker filled with water. This system allows a uniform pressure (atmospheric pressure) in the sampling line.

2.3.2 Gas-phase modeling

Gas-phase modeling was used to obtain the concentration of species which cannot be identified by GC measurement. For this purpose, the temperature profile was used as an input into a CHEMKIN [9] simulation to eliminate the need to model heat losses in the energy equation. Other experimental measurements at the surface of the top burner (mass flow rate, H_2, CO, CO_2, O_2 concentration) were also used as inputs. CHEMKIN modeling coupled a 1D-premixed code to the kinetic model. GRI Mech [10] was used in Chapter 4 and Ranzi's model [11] was used in Chapter 6 because it contains species like He and Ar that are not included in GRI-Mech. Figure 2.5 represents a general overview of the methodology to predict the evolution of gas-phase species in the top burner.

The GC probe sampling technique is innately intrusive. The probe cools the flame and disturbs the flow ahead of the sampling position. Previous studies [12,13] showed the effect of flame cooling by the probe to be within about 2-3 mm ahead of the probe. There are two approaches that can be applied to match the model data with the experimental data. The first one is using the measured temperature profile to obtain the model results. Then, the model results are shifted downstream by a finite distance. The second approach is shifting the temperature profile first and then using it in the model. Both approaches result in the same outcome.

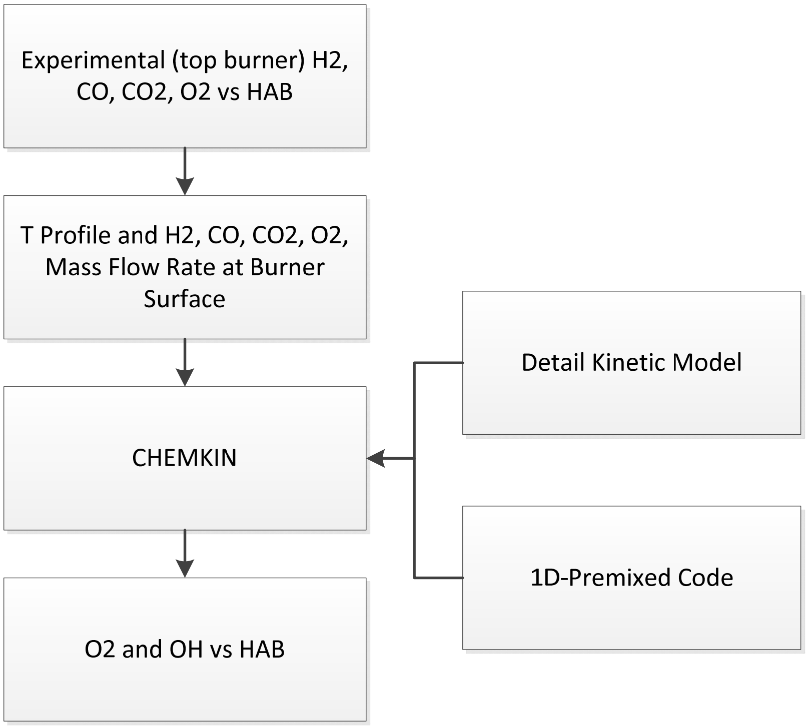

Figure 2.5. Schematic representation of the methodology used to predict gas species. (adapted from [4])

2.4 Particle mobility size measurements

Particle size distributions and soot concentration were measured with a scanning mobility particle sizer (SMPS). An SMPS consists of a 3025 ultrafine condensation particle counter (UCPC) and a TSI 3080 electrostatic classifier equipped with either a 3085 nano-differential mobility analyzer (nano-DMA) or a 3081 long-DMA. After particles are drawn into the probe, they first enter the classifier. The aerosol neutralizer inside the classifier exposes particles to a high concentration of bipolar ions to establish a known bipolar charge distributions. Then, the charged particles are subjected to an electric field created in the DMA. A DMA contains two metal cylinders; the inner cylinder is negatively charged while the outer cylinder is electrically grounded. This creates an electrical fields between two cylinders that allows the positively charges particles to be attracted by the negatively charged collector rod. Particles with a high electrical mobility are collected on the upper portion of the rod, and particles with relatively lower electrical mobility are collected on the lower portion of the rod. Since the electrical mobility of particles in the electric field depends on the so-called mobility diameter, not on the density of the particles [14], the particles are differentiated by size along the length of the collector rod. By changing the voltage, the specific size range exits through the bottom of the DMA. This specific size is drawn into the condensation particle counter (CPC) in order to determine the particle concentration. In a CPC, particle concentration will be determined. Particles pass over a heated pool of alcohol and are saturated with alcohol vapor. The alcohol condenses onto the surface of the particles and they reach a size that is optically visible. At this point, the particles can be counted and can be separated into bins of discrete size. A scan lasts about 2 min. The gas flow can be adjusted to cover a wide range of particle sizes. Figure 2.6 shows the schematic of an electrostatic classifier with a Nano-DMA, which is used in the Chapters 3, 4, and 6.

A general overview of the SMPS and sampling system is presented in Figure 2.7. The sampling probe was placed horizontally above the burner with the orifice faced down toward the flame above the burner. The probe was mounted on a translation stage with the accuracy of probe positioning estimated to be 0.1 mm. In this system, particles were drawn into a small orifice (0.24 mm diameter) and instantaneously diluted using a

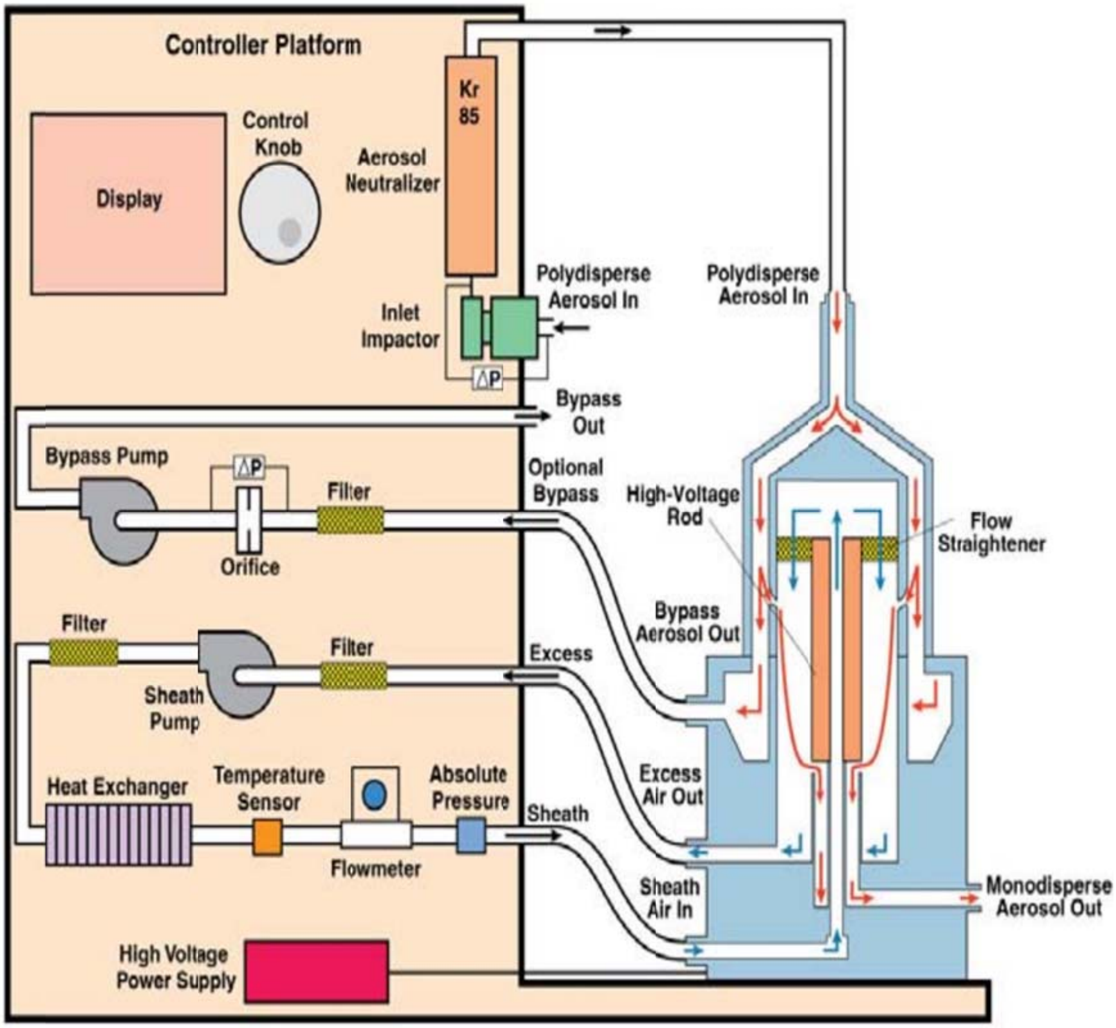

Figure 2.6. Schematic for the electrostatic classifier with Nano DMA [15] (Courtesy of TSI Incorporated).

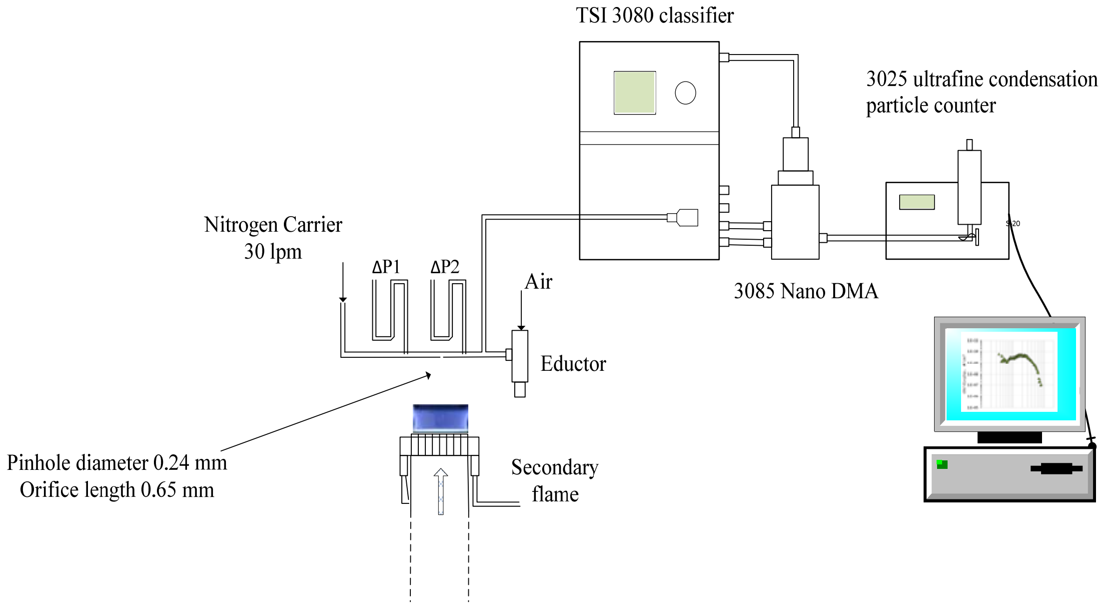

Figure 2.7. SMPS and dilution probe for PSD measurements.

N_2 stream at 30 lpm (STP) to prevent coagulation, diffusion losses, and condensation of higher-molecular weight hydrocarbons. In this study, the dilution system was similar to that of Zhao et al. [13], with some changes in probe size (OD= 11mm) and pinhole diameter (0.24 mm), as illustrated in Figure 2.7. Dilution ratio was determined by a method based on flow meter calibration at 300 K and 1 atm and corrected for viscosity and gas expansion at 1000 K [13]. The dilution ratios used in this study was determined to be in the proper range and it was between 4000-5000. The dilution gas flow was kept constant during the whole data set. Details on the probe optimization such as, critical pinhole diameter, flow conditions, dilution ratio calculations, control of the pressure drop through the pinhole, method reproducibility, and effect of the dilution ratio on PSD were presented in Echavarria [5]. A small portion (1.5 lpm) of the exit stream was sent to the SMPS for particle sizing and number concentration measurements. An eductor was used to control the pressure drop through the pinhole. The pressure difference across the probe orifice was monitored with the aid of two U manometers. The corrections for penetration efficiency into the probe and probe orifice and diffusion losses during transport were based on the procedure presented by Minutolo et al. [16]. This methodology was discussed in details by Echavaria [5].

It is assumed that the particles are spherical. Thus, the size measured for aggregates is presumed to be the diameter of an equivalent sphere having the same drag as the aggregate.

2.5 High-resolution transmission electron microscopy

The soot was sampled by using a fast insertion technique as illustrated in Figure 2.8. The soot sample was deposited on a lacey C/Cu 3.05 mm diameter TEM grid following the procedure of thermophoretic sampling by Dobbins [17]. Soot particles are adsorbed on the surface of a TEM based on the thermophoretic effect between the cold wall of the TEM sampling grid and hot gases of the flame [17]. Multiple insertions were necessary to get a representative soot sample on the grid. The time interval between each insertion was around 10-20 seconds to let the grid cool down. A TEM grid holder attached to a piston and compressed air at 60 psig was used to quickly insert the TEM grid into the flame to minimize the impact of flame temperature on the particles that experienced multiple insertions [5]. In addition, the control system was designed to move the probe with the maximum speed to a precisely defined position in the flame.

The soot samples for Chapter 3 and Chapter 5 were taken from the second burner at initial heights above the burner before soot oxidation happened. The precise spatial positioning of the probe within the flame was achieved by mounting the mechanical

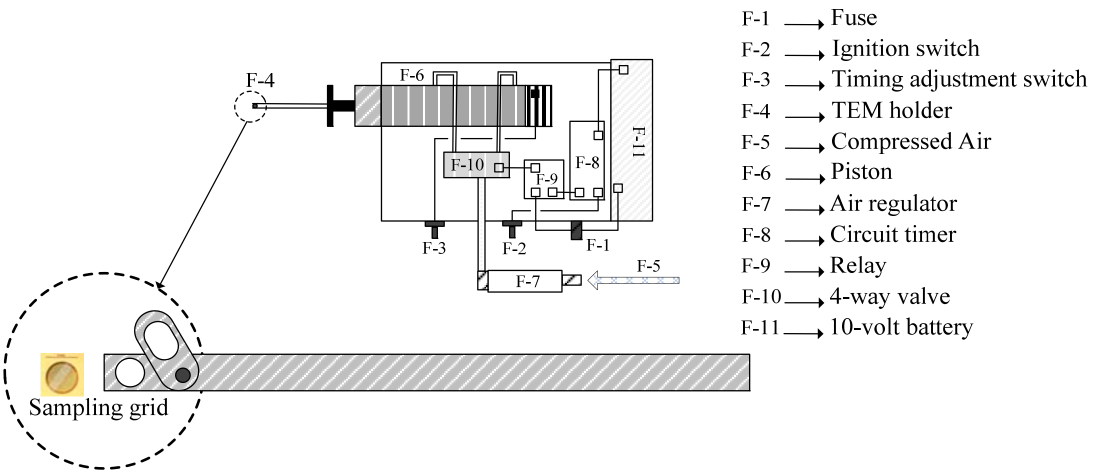

Figure 2.8. Soot particle sampling systems

components on a translation stage. The accuracy of probe positioning was estimated to be better than 0.1 mm. TEM images were taken using a FEI Tecnai F20 Ultratwin TEM/STEM operating at 200 keV.

2.6 X-ray photoelectron spectroscopy

Surface analysis was performed on soot samples obtained from 30% n-butanol/70n-dodecane and 60% n-butanol/40n-dodecane. Because the concentration of soot in the flame (≤ 0.01 µgr/cm3) was very low, collecting enough samples for X-ray Photoelectron Spectroscopy (XPS) analysis was challenging. Therefore, a new method was designed for sampling where a water-cooled sampling probe made of a ceramic tube (1/8 inch OD) was placed horizontally above the burner. The small size of the tube was chosen to minimize the effect of probe perturbation in the flame. When the water-cooled probe was in the flame, water vapor formed in the flame condensed on its surface. Hot particle-laden gas was exposed to cool surface of the tube which was covered with condensed water. The temperature gradient between the hot particle laden gas and the cold surface of the tube resulted in particle deposition on the tube surface due to thermophoresis. A layer of condensed water on the surface of the tube mixed with soot particles was collected by a thin needle-syringe system. The condensed water and soot particle mixture was collected in a bottle. Vacuum evaporation at room temperature was used to separate the water from soot particles. A clean piece of silicon wafer was placed in the bottom of the bottle, so that soot particles could be deposited on its surface. Figure 2.9 shows the visual abstract of the methodology used to collect soot particles. Sampling was performed for two fuel mixtures, 30% n-butanol/70% n-dodecane and 60% n-butanol/40% n-dodecane. In each fuel, particles were collected before oxidation and after oxidation. To collect soot sample before oxidation, the probe was mounted close to the surface of the burner but not touching it, with no flame running on the second burner. For collecting soot sample after oxidation, a flame was on and the probe was fixed at higher elevation (HAB = 8 mm), where soot oxidation was completed. The result of XPS analysis is given in Appendix C.

X-ray Photoelectron Spectroscopy (XPS) was performed by using a Kratos Axis Ultra DLD instrument. A monochromatic Al source was used for excitation. The spectra were recorded using a hemispherical energy analyzer positioned at an angle of 54.7 degrees with respect to the incident radiation and operated in the constant analyzer energy mode (CAE) at pass energy of 40 eV. The binding energy scale was calibrated in the usual way defining the carbon 1s peak with the highest intensity to be at 284.5 eV. The multiple analyses of relevant peaks were achieved by fitting model functions of mixed Gaussian and Lorentzian shape into the measured intensity distribution using a CASA xps program. Background subtraction was performed using the Shirley background model.

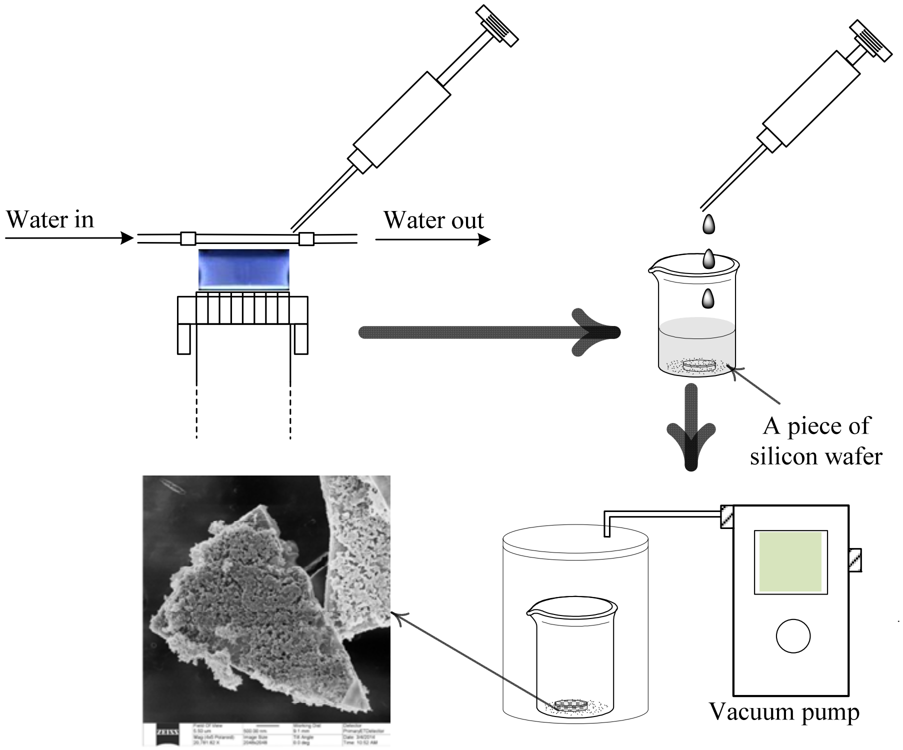

Figure 2.9. Experimental methodology to extract soot particles in a low sooting flame

2.7 References

[1] K.G. Neoh, J.B. Howard, A.F. and Sarofim, Soot Burnout in Flames, Massachusetts Institute of Technology, 1980.

[2] C.J. Merrill, The Oxidation and Fragmentation of Soot in a Two-Stage Burner, University of Utah, 2005.

[3] C.A. Echavarria, I.C. Jaramillo, A.F. Sarofim, J.S. Lighty, Proceedings of the Combustion Institute 33 (2011) 659.

[4] Carlos A. Echavarria, I.C. Jaramillo, A.F. Sarofim, J.S. Lighty, C.A. Echavarria, Combustion and Flame 159 (2012) 2441.

[5] C.A. Echavarria, Evolution of Soot Size Distribution during Soot Formation and Soot Oxidation-Fragmentation in Premixed Flames: Experimental and Modeling Study, University of Utah, 2010.

[6] A.S. Darling, G.L. Selman, R. Rushforth, Platinum Metals Review 15 (1971) 13.

[7] V. Hindasageri, R.P. Vedula, S. V Prabhu, Review of Scientific Instruments 84 (2013).

[8] D.C.S. McEnally, U.O. Koylu, L.D. Pfefferle, D.E. Rosner, Combustion and Flame 109 (1997) 701.

[9] R.J. Kee, J.F. Grcar, M.D. Smooke, J.A. Miller, Fortran Program for Modeling Steady Laminar One-Dimensional Premixed Flames., Sandia Natl. Lab., 1985.

[10] G.P. Smith, D.M. Golden, M. Frenklach, N.W. Moriarty, B. Eiteneer, M. Goldenberg, C.T. Bowman, R.K. Hanson, S. Song, J. William C. Gardiner, V. V. Lissianski, Z. Qin, (2015).

[11] E. Ranzi, A. Frassoldati, R. Grana, A. Cuoci, T. Faravelli, A.P. Kelley, C.K. Law, Progress in Energy and Combustion Science 38 (2012) 468.

[12] A.D. Abid, N. Heinz, E.D. Tolmachoff, D.J. Phares, C.S. Campbell, H. Wang, Combustion and Flame 154 (2008) 775.

[13] B. Zhao, Z. Yang, J. Wang, M. V. Johnston, H. Wang, Aerosol Science and Technology 37 (2003) 611.

[14] W.C. Hinds, Aerosol Technology: Properties, Behavior, and Measurements of Airborne Particles, 2nd Edition., Wiley, 1998.

[15] TSI, Series 3080 Electrostatic Classifiers Operation and Service Manual, 2009.

[16] P. Minutolo, A. D’Anna, M. Commodo, R. Pagliara, G. Toniato, C. Accordino, Environmental Engineering Science 25 (2008) 1357.

[17] R.A. Dobbins, C.M. Megaridis, Langmuir 3 (1987) 254.

CHAPTER 3

SOOTING BEHAVIORS OF *n*-BUTANOL AND *n*-DODECANE BLENDS

3.1 Introduction

Soot emissions from diesel engines have considerably reduced over the last decade due to new fuel formulations, improved engine designs, and more effective emission-control technology. Soot particles come from many sources, but soot emitted from diesel engines is believed to be an important pollutant [1–3]. Soot particles deposit in the lungs and have potentially more adverse health effects [4]. Other damaging effects of ultrafine particles are climate forcing and cloud formation [5]. The damaging effects of soot emission from diesel engines have become a major concern and motivated a wide range of studies on understanding the formation and oxidation of soot particles in diesel engines. The effect of alcohols as oxygenated compounds on the reduction of soot emissions has been widely studied [6–10]. Propanol and butanol are becoming increasingly attractive as additives or alternative fuels compared to other conventional alcohols, because they are less prone to water contamination, are less corrosive, and have better blending stability and lubricity [11–13]. However, *n*-butanol can potentially be produced from a renewable source in a higher yield [11]. The study of the formation and reactivity of soot derived from diesel-oxygenated fuel, in this case a surrogate (*n*-butanol and *n*-dodecane), is important. First, previous studies suggest that the additional of *n*-butanol to diesel fuel reduced soot formation. Yao et al. [14] investigated the influence of *n*-butanol content in diesel fuel on soot emission from a heavy-duty engine. They showed that an increase of *n*-butanol content led to further reduction of soot. A similar result was presented by Zhang et al. [15]. An experimental study was carried out on a modified single cylinder heavy duty diesel engine to investigate the effects of *n*-butanol on diesel engine combustion and emission characteristics. Their results showed a significant decrease in soot emissions.

Second, The use of diesel particulate filters (DPFs) is becoming necessary to control soot particle emitted from exhaust [16–18]. Filter clogging can be avoided by continuously regenerating the DPF. However, conditions for the continuous regeneration depend not only on engine conditions, but also upon oxidative reactivity of particles on the DPF [19]. Accordingly, the study of reactivity of soot derived from diesel affected by *n*-butanol adding is important. In this regard, many studies investigated the oxidation rate of diesel or biodiesel soot, but only a few investigated soot reactivity [20–23] and little work has been done to show the effect of the increase of *n*-butanol in diesel fuel on the reactivity behavior of soot during oxidation process. Vander Wal & Muller [23] showed that soot reactivity was related to its nanostructure. They found that curvy and disordered structures were more reactive than structures formed by planar graphitic layers. For this study, the authors used three different fuels; a blend of the diesel primary reference fuels n-hexadecane (NHD) and 2,2,4,4,6,8,8-heptamethylnonane; neat (i.e., 100%) biodiesel (B100); and neat diethylene glycol diethyl ether (DGE). Song et al. [24] used two different fuels –a Fischer-Tropsch fuel (FT) and a pure biodiesel (B100)— to compare the oxidation behavior and mechanisms for enhanced oxidation. Their results demonstrated that initial oxygen functional groups have a stronger influence on the oxidation rate and soot reactivity rather than its initial nanostructure. Yehliu et al. [16] also focused on the impact of fuel composition on soot reactivity and nanostructure. They examined three different fuels—an ultra-low sulfur diesel fuel (BP15) as a baseline fuel; a Fischer-Tropsch fuel (FT); and a neat biodiesel (B100). Their results were consistent with work by Vander Wal & Muller [23], but in contrast to Song et al. [24] which identified the importance of surface oxygen groups in increased oxidative reactivity.

Our study attempted to further look at the role of both nanostructure and oxygenated fuel on soot surface reactivity. The average carbon content in diesel fuel ranges from 12 to 13; *n*-dodecane was used as a diesel surrogate [25–27]. While there are many studies investigating the reduction of soot after adding an alcohol [14,15,28], this study addressed the impacts of increasing *n*-butanol as an oxygenated compound on the formation, reactivity of soot, and role of soot nanostructure. All experiments were conducted in a two-stage burner. A scanning mobility particle sizer (SMPS) was used to measure the soot particle size distributions (PSDs) in the flame at different heights above the second burner during oxidation. Image analysis was used to quantify soot nanostructure and to reveal differences in the structural order. Our observations based on the measurement of PSDs showed that although increasing *n*-butanol content in diesel fuel reduced tendency of soot formation, it did not enhance soot reactivity.

3.2 Experimental setup and methods

The two-stage burner used in this study operates at atmospheric pressure [29,30]. During the first stage, soot is generated in a fuel-rich premixed flame. In the second stage, a premixed burner isolates the soot oxidation process from the formation process in the first stage [4,30–34]. An oxygenated-diesel surrogate fuel was used in the experiments and consisted of *n*-butanol/*n*-dodecane blends at different molar ratios, 10/90, 30/70, and 60/40. In this study, *n*-dodecane was used as single-component fuel surrogate to represent diesel fuel. Figure 3.1 is a schematic of the burner system.

As seen in Figure 3.1, the liquid-fuel mixture was injected into the vaporizer (V-1) using a syringe pump (KDS-410). Vaporized fuel was mixed with primary air in the manifold and then fed into the bottom of first-stage burner. The temperature in the vaporizer and along the feeding line was adjusted to avoid fuel condensation.

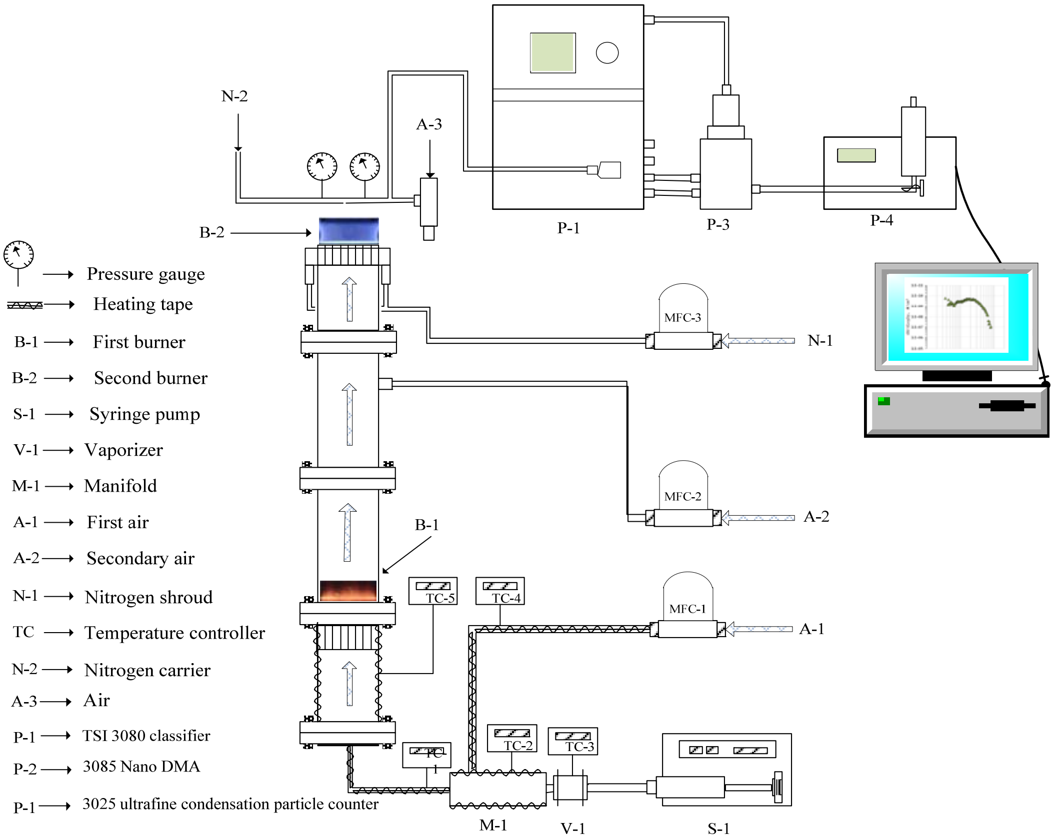

Figure 3.1. Schematic representation of the two-stage burner and feeding system.

The fuel and air mixture were then passed to the bottom of the first stage which is a stainless steel pipe (51 mm ID, Schedule 80, 127-mm long). The velocity of unburned gases, the equivalence ratio at the first burner, and overall equivalence ratio were kept the same for all fuel blends. The velocity of unburned gases in the bottom burner, which was held at standard temperature (298.15 K) and pressure (1atm), was 3.5cm/s. The equivalence ratio at the first stage was (Φ_1 = 2.2). The pre-oxidation chamber of the secondary burner served to efficiently mix soot-laden combustion gases with air. Air was introduced by means of an injection port in order to control the overall equivalence ratio (Φ_{overall} = 1.1). The overall equivalence ratio (Φ_{overall}) is defined by the ratio of fuel to total air (air injected in the bottom and top burners) fed into the burner over the stoichiometric ratio:

$$\Phi_{overall} = \frac{\frac{Fuel\ Blends}{Total\ Air}}{\frac{Fuel\ Blends}{Stochiometrc\ Air}} \tag{3.1}$$

The soot-laden combustion gases, along with secondary air, were passed through a secondary flat-flame premixed burner. The flame was stabilized over a tube bundle (1/16" ID, 1" long) and was shielded using a nitrogen shroud to avoid diffusion of surrounding air. All measurements, including temperature, particle size distributions, and soot surface area, were performed above the secondary burner. A 0.2032-mm uncoated Type-B thermocouple was used to measure temperature profiles along the center line. The radiation correction for the temperature was similar to that of McEnally et al. [35]. SMPS, which consisted of a TSI 3080 classifier and a 3025 ultrafine condensation particle counter, was used with either a 3085 nano-DMA (differential mobility analyzers) or a 3081 long-DMA to measure particle size distributions (PSDs) in the size range from 3 to 340 nm. For the case of 10%*n*-butanol/90%*n*-dodecane, the nano-DMA and long-DMA number counts were matched at 80 nm diameter. The SMPS sampling system was similar to that used by Zhao et al. (2003). The corrections for penetration efficiency into the probe and probe orifice and diffusion losses during transport were applied following the procedure presented by Minutolo et al. [36].

Soot samples were taken for HRTEM analysis following the procedure of thermophoretic sampling by Dobbins [37]. TEM grids were oriented with the face perpendicular to the flow of combustion gases. Multiple insertions were used to get enough soot to present a representative sample on the grid. A TEM grid holder was attached to a piston and compressed air at 60 psig was used to quickly insert the TEM grid into the flame in order to minimize the impact of flame temperature on the particles that experienced multiple insertions. Soot grid samples were taken from the second burner at a HAB equal to 1.5 mm where soot burnout percentage was less than 50% for three cases. HRTEM images were taken using a transmission electron microscope FEI Tecnai F20 Ultratwin TEM/STEM operating at 200 keV.

HRTEM images were processed by a novel image analysis framework specifically designed for analyzing HRTEM micrographs of soot. The details of the framework can be found in [38–40]. Briefly, the framework is based on filtering theory—the micrographs are filtered with special two-dimensional filters in order to extract interlayer spacing and symmetry parameters. Gabor filters [41] tuned to frequencies present in soot HRTEM micrographs were used to extract interlayer spacing distribution—in a previous study [38], the filtering method produced datasets that were two orders of magnitude more robust than datasets produced by conventional fringe analysis algorithms [42]. Nematic and polar order parameters (S_{2N} and S_{2P}, respectively) were extracted by the orientation-filtering technique described by Toth et al. [39]. Polar symmetry implies a curvy structure and nematic symmetry is the limiting case—polar symmetric regions with zero curvature. These parameters were first used to describe soot nanostructure by Shim et al. [43] and are defined as follows:

$$S_{2N} = 2\langle cos^2(\alpha_i) \rangle - 1 = 2\left\langle \left(\vec{d}\,.\,\vec{u}_i\right)^2 \right\rangle - 1 \tag{3.2}$$

$$S_{2P} = 1 - 2\langle cos^2(\alpha_i)\rangle = 1 - 2\langle(\vec{r}_i\,.\vec{u}_i)^2\rangle \tag{3.3}$$

where S_{2N} is the nematic order parameter, S_{2P} is the polar order parameter, α_i is the angle between the fringe orientational vector and mean orientational vector, and < > means mean value. The director $\vec{d}$ is a unique unit vector describing the preferential orientation of the entire field in the nematic symmetry; in the polar case, $\vec{r_i}$ is a vector pointing from polar symmetry poles (amorphous particle cores) to the fringe centroids. For a perfectly ordered structure, S_{2N} is 1 and 0 for a perfectly disordered structure, while S_{2P} is 1 for perfect concentric symmetry, less than 1 for disordered phases and -1 for radial symmetry (see Figure 3.2).

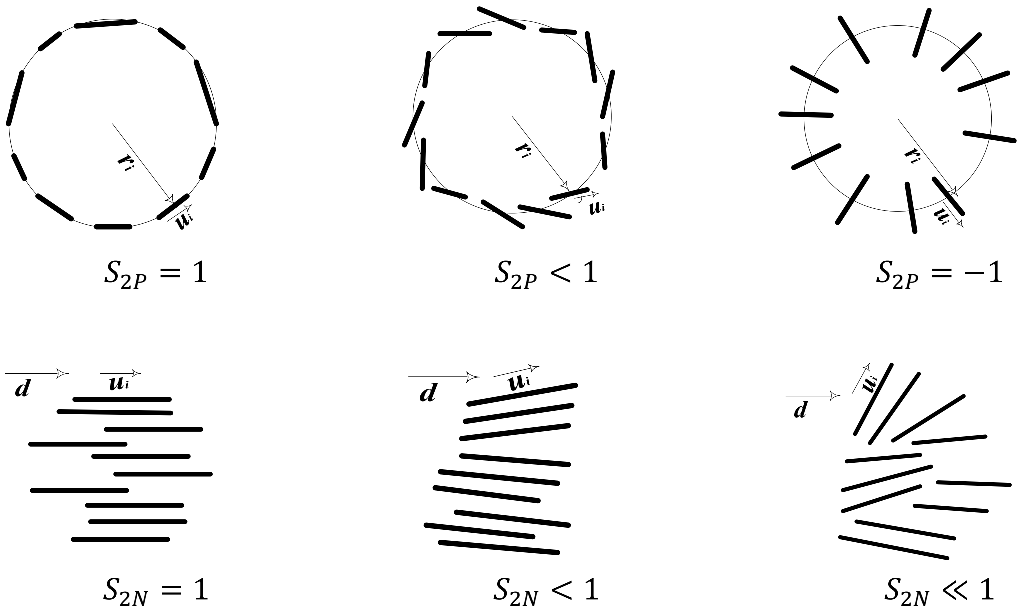

$S_{2P} = 1$ $S_{2P} < 1$ $S_{2P} = -1$

$S_{2N} = 1$ $S_{2N} < 1$ $S_{2N} \ll 1$

Figure 3.2. Examples of orientational order modes in two-dimensional projections. The top shows a typical polar symmetry in three cases; the left one is perfectly concentric symmetry, the middle is random orientation, and the right is radial symmetry. In this case, $\vec{u}_i$ is the direction unit vector and $\vec{r}_i$ is the position vector relative to the pole. The bottom shows typical nematic symmetry; from left to right are perfectly ordered, slightly disordered, and completely disordered phase with random orientations, where the director $\vec{d}$ is the mean orientation and $\vec{u}_i$ is the axis of particle *i*, respectively.

3.3 Results and discussion

3.3.1 Temperature profiles and evolution of the particle size distribution

Figure 3.3 shows the measured and radiation-corrected temperature profiles for different molar percentages of *n*-butanol/*n*-dodecane blends as a function of height above burner (HAB). The x-error bars in the temperature measurement came from thermocouple positioning uncertainty (±0.2 mm). The y-error bars represent temperature measurement uncertainty (±50 K). Temperature increased rapidly close to the burner surface until it reached a peak value due to oxidation of pyrolysis gases from the first burner. Downstream, temperature leveled off and started to drop. The average temperatures increased slightly with decreasing *n*-butanol percentage.

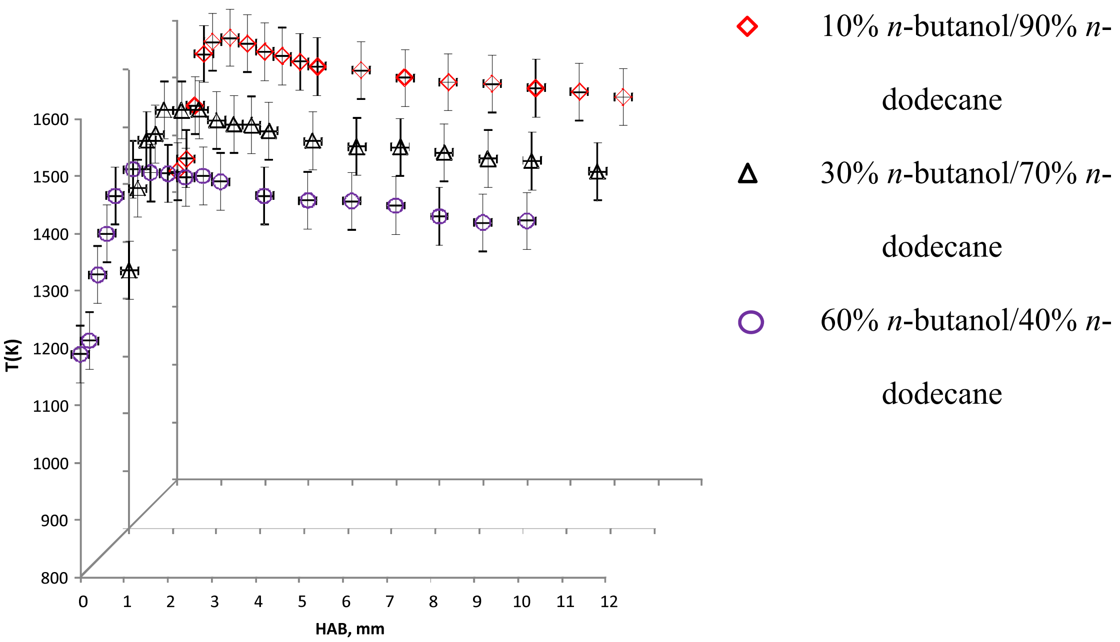

Figure 3.3. Top burner temperature profiles as a function of HAB.

By increasing *n*-butanol in the blend from 10% to 30% and 60%, the average temperature changed from 1502K to 1465K and 1449K, respectively.

The PSDs as a function of HAB are shown in Figure 3.4. The PSDs of the 10% *n*-butanol/90% *n*-dodecane were dominated by the fine mode (mobility diameters >10 nm) with little contribution by the ultrafine mode (mobility diameters <10 nm). When the *n*-butanol percentage increased beyond 10%, the soot number concentration in fine mode reduced and the mean value of the mobility diameter distribution was reduced from approximately 66 nm in 10% to 18 nm at 30% and 11 nm at 60% *n*-butanol close to the second burner. The reduction in the mobility diameter clearly showed the effect of *n*-butanol in suppressing soot formation. This behavior is explained kinetically by a reduction in concentration of soot precursors and aromatic compounds, slowing down soot formation in the first burner [44].

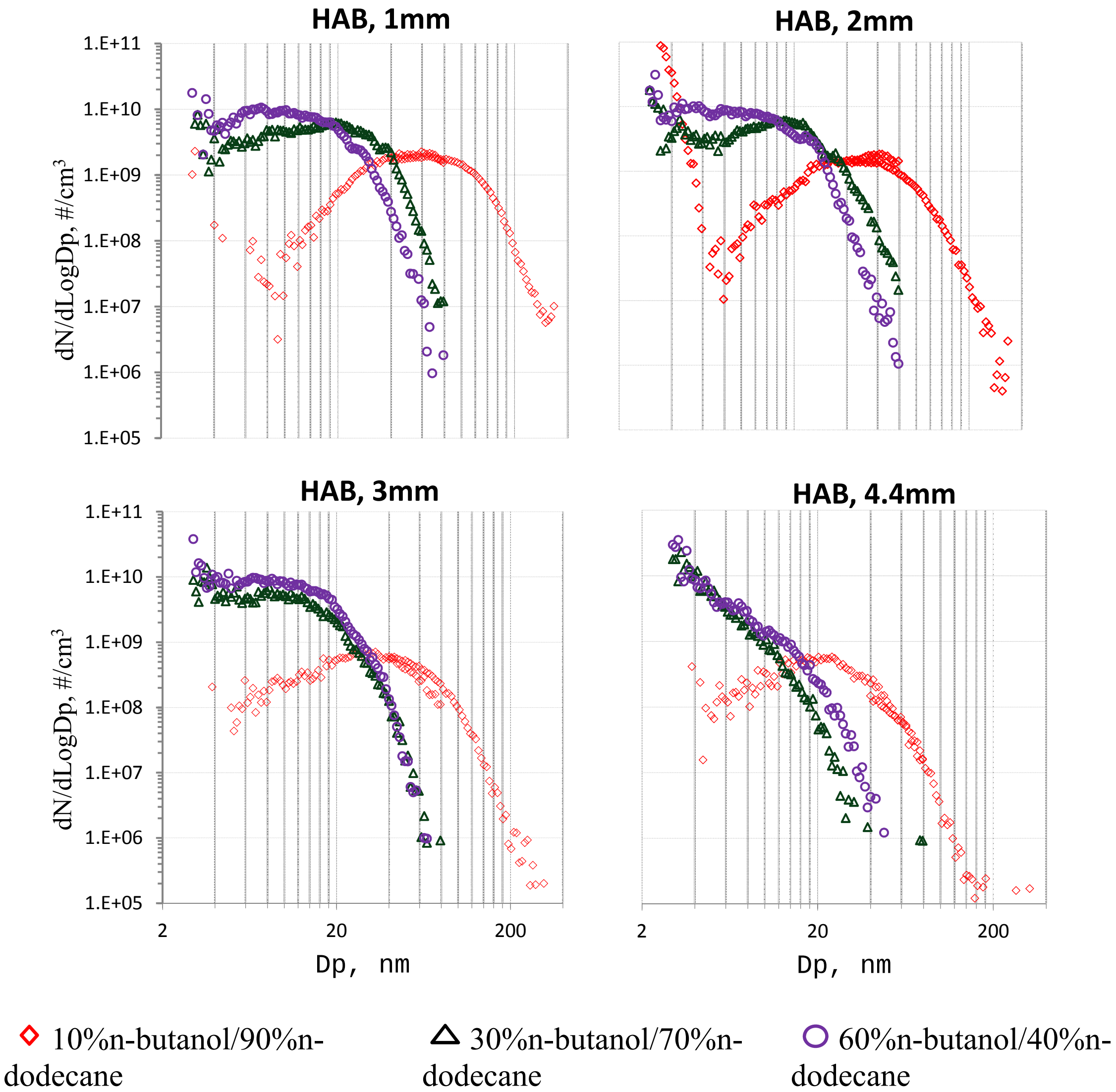

Figure 3.4. An example of the particle size distributions for different *n*-butanol/*n*-dodecane blends at different heights. Fragmentation for 10%*n*-butanol/90%*n*-dodecane is shown at HAB=2 mm.

As the oxidation proceeded in the range of 1 to 4 mm HAB, the particles started to burn out significantly as evidenced by a reduction in number of particles. At an HAB greater than 4mm, the PSDs did not undergo any noticeable change. Echavarria et al. [31] found that for ethylene, particles in the ultrafine mode were almost completely combusted at higher elevations above the burner and particles in the fine mode were dominant. In this study, most of the ultrafine particles remained as the HAB increased. In addition, Figure 3.4 shows that the number of particles for the 60% n-butanol blends, at higher HAB, was larger as compared to those for 30% n-butanol/70% n-dodecane blend, an unexpected result. It can be clearly concluded from this observation that soot from 30% n-butanol/70% n-dodecane blend was more reactive than that of 60% n-butanol/40% n-dodecane and, to a lesser extent, 10% n-butanol/90% n-dodecane. The chemical mechanism involved with this observation has not been identified and nanostructures may account for these changes.

3.3.2 Soot number and mass concentration

To evaluate the influence of n-butanol on ultrafine versus fine modes, the percentage of ultrafine particles was determined. In this case, the number of particles less than 10 nm was integrated separately as was the total number of particles. The percentage of the number of ultrafine particles (*UPNP*) was calculated by:

$$UPNP\ \% = \frac{\text{integral of particles number in size intervals less than 10nm}}{\text{integral of particles number in all sizes}} \times 100 \tag{3.4}$$

The fine particle number percentage (*FPNP*) can be calculated by the difference:

$$FPNP\% = 100 - UPNP\% \tag{3.5}$$

Figure 3.5 depicts the UPNP% associated with given HABs (mm). At low HABs, the UPNP% for 10% n-butanol/90% n-dodecane was a few percent. By increasing n-butanol

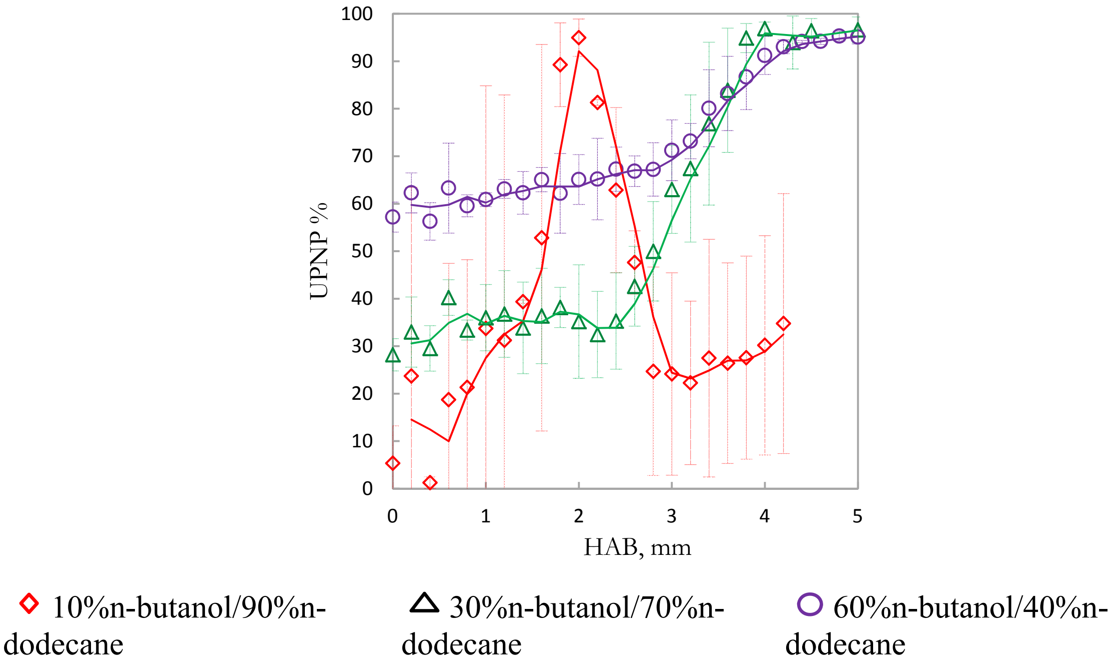

Figure 3.5. The percentage of ultrafine particles in the total number of particles for different blends. Symbols are experimental data; Smooth lines show the trend of each blend.

to 30% and to 60%, the portion of ultrafine particles increased. For all different *n*-butanol blends, the UPNP% increased as oxidation proceeded at higher HABs, indicating that as the particles burned, their mobility diameter decreased. As showed in Figure 3.4, for the 10% *n*-butanol/90% *n*-dodecane blend, the UPNP% increased from 5% to around 95% at HAB of approximately 2mm. As shown in the figure, these particles burned quickly, and the percentage returned to approximately 10% by 3mm HAB. The increase in the UPNP% was attributed to fragmentation; this occurred at higher soot mass burnout (~70%). The fragmentation is likely the result of oxygen diffusion inside the soot agglomerates causing internal burning. This led the particles to breaking apart [29,30]. Neoh and coworkers [29] also found fragmentation for ethylene flame at approximately 70% burnout.

Soot mass concentration (SMC) was calculated directly from the SMPS size and number concentrations assuming spherical particles:

$$SMC_i = \left[\sum_{j=dp_1}^{j=dp_n} N_j \, \rho_j \, V_j \right]_i \tag{3.6}$$

where,

SMC_i Soot mass concentration at the height *i* above the burner, g/cm^3

N_j Number of particles per unit volume which have the size dp_j, #/cm^3

ρ_j Density of particle which have the size dp_j, g/cm^3

V_j Volume of particle which have the size dp_j, assumed to be spherical, cm^3

The change in soot density with respect to mobility diameter was determined according to the approach by D'Anna et al. [45]. In this approach, twenty-six sections are used in a geometric series. Correspondingly, the density changes from 1.2 g/cm^3 for the first section to 1.8 g/cm^3 for the last one. As seen in Figure 3.6(a), the mass of ultrafine particles was highest for the 60% *n*-butanol/40% *n*-dodecane mixture, followed by 30% *n*-butanol/70% *n*-dodecane and then 10% *n*-butanol/90% *n*-dodecane. Figure 3.6(b) shows the mass of the larger particles. In this case, 10% *n*-butanol/90% *n*-dodecane mixture exhibited the most mass of larger particles, followed by a decrease with an increase in *n*-butanol, up to 4 mm HAB. At HAB greater than 4 mm, the order changed with 60% showing more mass as compared to 30%. The last panel of Figure 3.6(c) shows the total mass concentration, which demonstrates the same trends as Figure 3.6(b), as the larger particles dominate the mass.

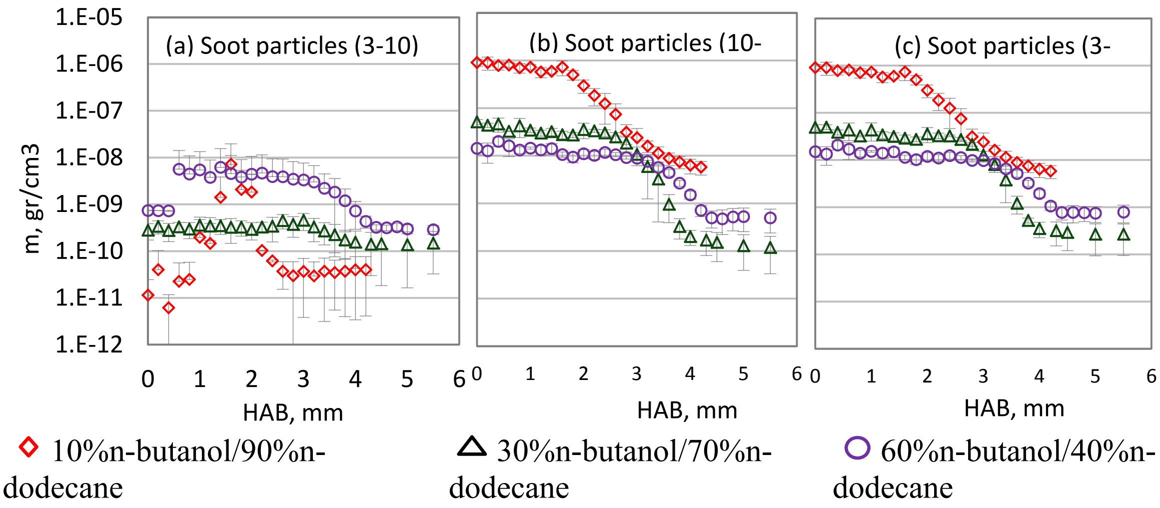

Figure 3.6. Soot mass concentrations for different *n*-butanol/*n*-dodecane blends. (a) Ultrafine particles (3-10nm); (b) fine particles (10-340nm); (c) summation of ultrafine and fine particles (3-340nm). The error bars represent the standard deviation of the measurements.

In summary, the amount of refractory soot for the 10% *n*-butanol/90% *n*-dodecane was around 22 times greater than the 60% *n*-butanol/40% *n*-dodecane. The 60% *n*-butanol/40% *n*-dodecane was around 3 times greater than 30% *n*-butanol/70% *n*-dodecane.

3.3.3 Sooting tendency and sooting stability numbers

The above results led us to investigate the sooting tendency and stability of soot as the amount of *n*-butanol increased. It is well understood that specific experimental parameters strongly affect the results for sooting behavior [46]. Accordingly, sooting tendency (*ST*) for this study was defined as:

$$ST_{k\%} = \frac{SMC_{k\%}|^{max}}{SMC_{10\%}|^{max}} \tag{3.7}$$

In the above expression, the numerator corresponds to the maximum soot mass concentration for a blend with 10% of *n*-butanol, and the denominator corresponds to the maximum soot mass concentration for a blend with *k*% of *n*-butanol. There are number of methods to quantify the sooting tendency of fuels [47–49]. This study's definition of *ST* is more similar to the method proposed by McEnally and Pfefferle [48], which was based on the maximum soot volume fraction measurement. The 10% *n*-butanol/90% *n*-dodecane blend was chosen as the reference because of having the highest amount of soot formation between other cases. The other parameter which was examined was the sooting stability (*SS*). This number is the ratio of the minimum soot mass concentration of a blend with *k%* *n*-butanol content to the minimum soot mass concentration of 30% *n*-butanol/70%*n*-dodecane. The blend of 30% *n*-butanol/70%*n*-dodecane showed the minimum amount of soot after oxidation process between other blends and was chosen as the reference. In fact, the minimum soot mass concentration appeared in the higher elevation where soot did not undergo further oxidation. The *SS* can be determined as follows:

$$SS_{k\%} = \frac{SMC_{k\%}|^{min}}{SMC_{30\%}|^{min}} \tag{3.8}$$

This number is defined to quantify the amount of soot leaving the second burner after oxidation process. The definition of *SS* is similar to the definition of the *ST*; both parameters are the ratio of soot mass concentration of a blend to a reference. Sooting tendency is defined based on the maximum soot mass concentration, implying the tendency of the fuel blends to form soot. Sooting stability is based on the minimum soot mass concentration showing the amount of soot after oxidation process for each case. This comparative parameter indirectly suggests the reactivity of soot against oxidizers. Both *SS* and *ST* parameters are defined consistent with our experimental results to describe and quantify our observations from SMPS measurement.

The results for *ST* and *SS* are depicted in Figure 3.7. By increasing the *n*-butanol percentage in the fuel blend, *ST* decreased, as expected. As the mass fraction of oxygen in the fuel mixture increased, a larger fraction of the total amount of carbon in the fuel was converted to CO and CO_2 and a smaller amount of carbon is present as soot precursors. The combustion products of longer alkanes include a greater proportion of higher alkenes like pentene and butane; therefore, their sooting tendencies increase. Further replacement of *n*-dodecane by n-butanol further reduces their soot precursors.

On the other hand, *SS* decreased with increasing *n*-butanol until 30%. After this, there was an increase at 60% *n*-butanol. Even though the amount of soot was less at 60% *n*-butanol, it appeared to be more stable than 30% *n*-butanol blend. This unexpected observation can be related to the effect of *n*-butanol on soot structures to form stable intermediates during oxidation process. Studies investigating different types of reactive sites present on soot structures [50–54] found carboxyl acid, phenol, lactone, cyclic peroxide, quinone, and carboxyl anhydride [55] at the edge of carbon planes [56]. As a result, they are completely exposed to the main oxidizers like O_2 and OH. Accordingly, these active sites formed on the surface of soot particle affect the reactivity and subsequently the nanostructure and the oxidation rate. From our observation, it can be concluded that increasing *n*-butanol from 30% to 60%, formed the structures which were less active.

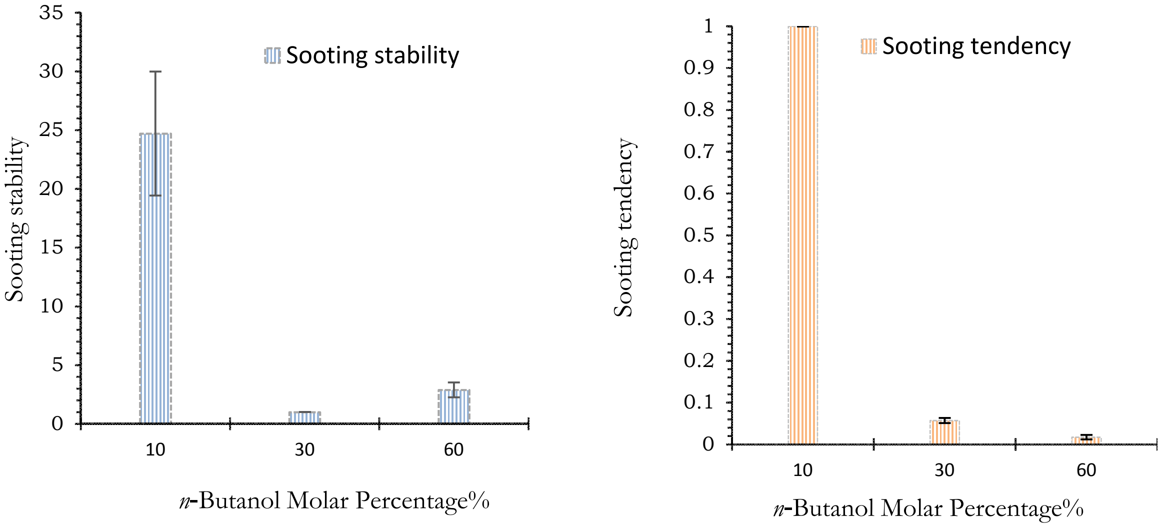

Figure 3.7. Sooting tendency (*ST*) and sooting stability (*SS*) of *n*-butanol/*n*-dodecane blends.

3.3.4 Soot morphology and image analysis

Examples of HRTEM images and symmetry saliency maps are shown in Figure 3.8 for three different *n*-butanol/*n*-dodecane blends at 1 mm HAB. For two cases, 10% *n*-butanol/90% *n*-dodecane and 60% *n*-butanol/40% *n*-dodecane, the agglomerates consist of multilayer fullerenoid structures which are surrounded by longer and parallel layers. Alternately, in the 30% *n*-butanol/70% *n*-dodecane (middle), the surface is dominated by short segments grouped together in short stacks. The saliency map of the HRTEM images in Figure 3.8 on the bottom show the different hues of orange and green colors, corresponding to the strength of polar and nematic symmetry, respectively.

Multiple images were taken from the same grid in order to determine fringe spacing and symmetry analysis. All images from the same sample were processed and then integrated to derive a single graph for the interlayer distance and symmetry strength histograms. Figure 3.9 represents the discrete histograms of interlayer spacing for three

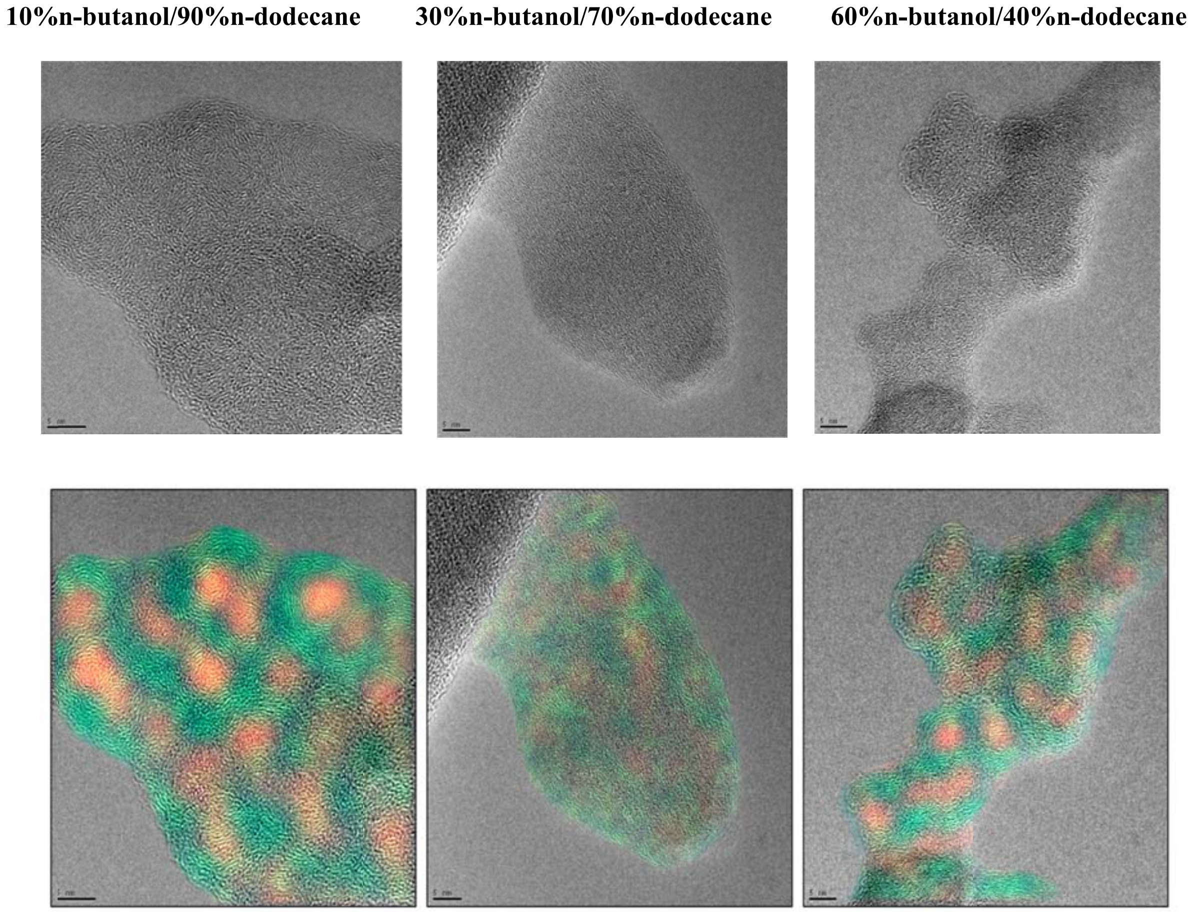

10%n-butanol/90%n-dodecane **30%n-butanol/70%n-dodecane** **60%n-butanol/40%n-dodecane**

Figure 3.8. Examples of HRTEM images of the soots derived from three different *n*-butanol/*n*-dodecane blends. Raw images are on the top. The bottom images are symmetry saliency maps. Hues of green and orange indicate the strength of nematic and polar symmetry, respectively.

different *n*-butanol/*n*-dodecane blends. Clear differences exist between the distributions. The soot derived from 10% *n*-butanol-90% *n*-dodecane had the widest histogram with a mean value of 4.33 *Å*. By increasing the value of *n*-butanol to 30% and 60%, the spread of the distribution became narrower and the mean value decreased to 4.27 and 4.21 *Å*, respectively. The slight shifting of the interlayer spacing distributions towards lower values demonstrates the compaction in the layered structure.

Previous studies showed that increasing the oxidation of soot or residence time of

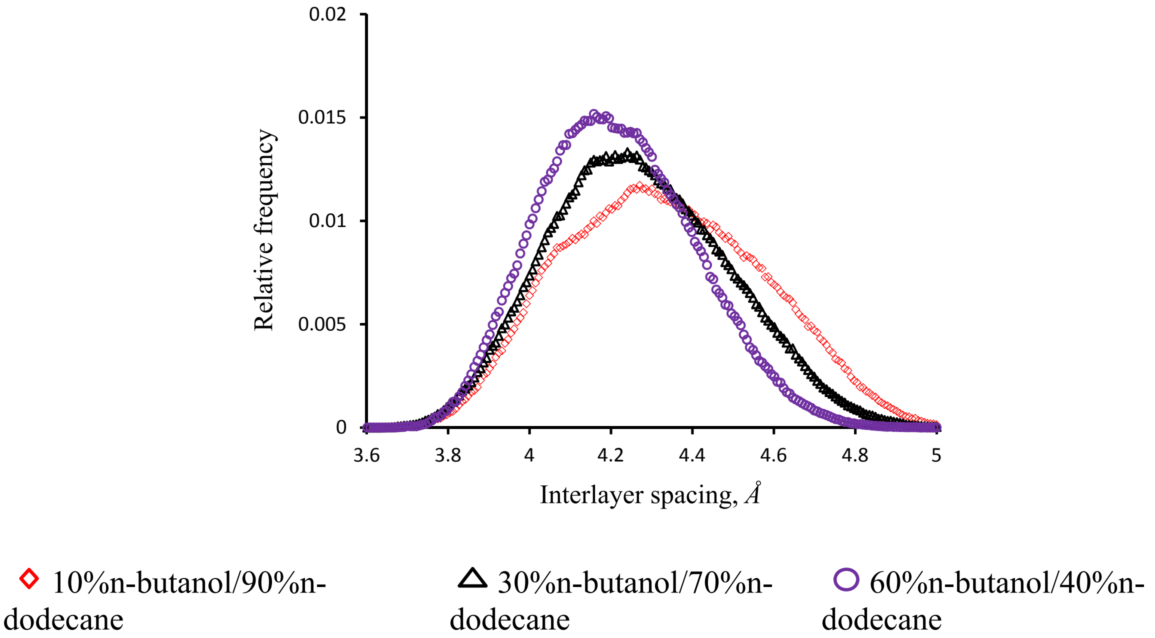

Figure 3.9. The histogram of interlayer spacing for three different *n*-butanol/*n*-dodecane blends.

soot in the high temperature regime decreased the interlayer spacing [57–59]. By decreasing the interlayer spacing, the amorphous structure is expected to become more orderly [57,58] and the restructuring of carbon planes tend to form a graphitic state which is more thermodynamically favored [58]. Accordingly, we would expect that the 60% n-butanol/40% n-dodecane, which had the lowest mean interlayer value, experienced more residence time in the high temperature region and finally attained the highest structural order. However, as detailed below, the 10% n-butanol-90% n-dodecane was more structured than two other blends while it had the greatest interlayer spacing in contradiction with findings. This means that the effect of residence time on soot interlayer spacing has to be considered separately for different fuels as Palotas et al. showed in his work [58]. Lapuerta et al. [60] investigated the effect of the fuel and engine mode on the interlayer spacing of the soot lattice. All soot sampling, temperature, and pressure measurements were done for two biodiesel (an oxygenated fuel) and diesel fuels in an automotive diesel engine running at three different modes. With the same residence time for two fuels, the temperature for diesel was always greater than that of biodiesel, but interlayer spacing was greater for diesel. The presence of oxygenated fuel reduced interlayer spacing, consistent with our result in section 3.3.

The polar or nematic symmetry saliency maps in Figure 3.8 show 10% *n*-butanol concentration had the strongest hues of green and orange colors followed by 60% *n*-butanol, and 30% *n*-butanol concentration. The computed histograms of the nematic and polar symmetry strength as a function of symmetry scale are shown in Figure 3.10.

The combination of both nematic and polar symmetry provide structural information related to the crystalline order in soot. The small symmetry strength value means very short, individual segments with random orientation. Although some small curvy structures—small curvatures in the range of few angstroms to few nanometers that can be taken into account as curvy PAHs—are seen in low nematic and polar symmetry strength, short segments were dominant. At intermediate polar and nematic symmetry strength, higher amount of small curvy structures are available rather than very short segments. These small structures had high curvature. At higher symmetry strength, the low curvature structure has extended and formed larger layer plane. These more-ordered layer planes had lower curvature structures and oriented parallel to each other. The layer plane with lower curvature is more than layer plane with higher curvature by increasing symmetry strength. The "cartoon" of nematic and polar symmetry in Figure 3.10 helps explain this behavior. As seen, 30% *n*-butanol/70% *n*-dodecane had the smallest symmetry strength value in both the nematic and polar histograms. This indicated more

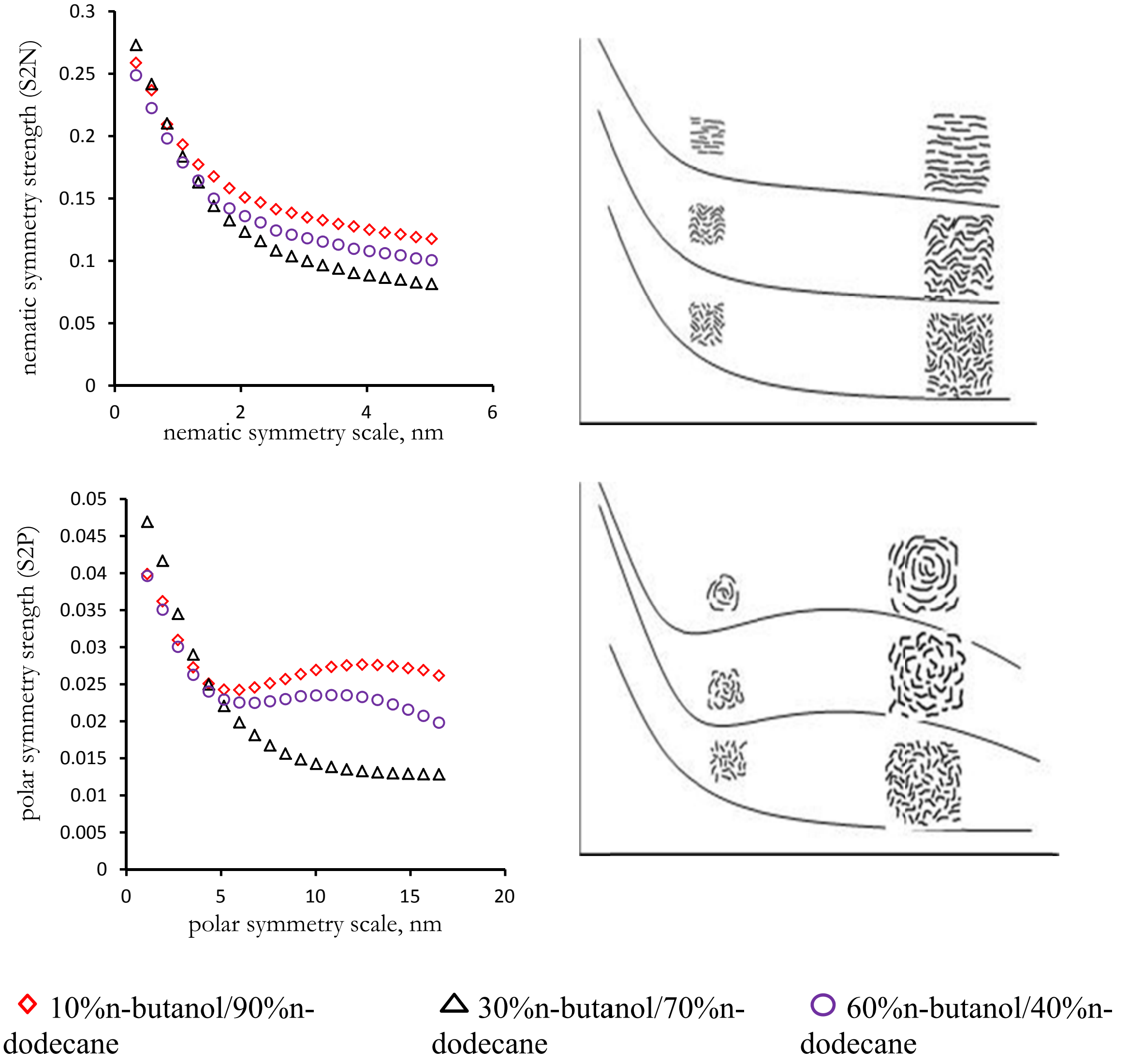

Figure 3.10. Histograms of symmetry strength versus symmetry scale are shown for nematic symmetry (top) and polar symmetry (bottom). The right panel, top and bottom, are “cartoons” to depict the structural differences in the left side images.

irregularity and edge site positions which are more exposed to the oxidizers. The slight increase in the nematic symmetry histogram for 60% and 10% *n*-butanol concentrations corresponded to more-ordered outer layers surrounding concentric cores.

All three cases have high degree of order at short length scales (below about 1 nm). The same behavior can be seen in the polar symmetry histogram. Obviously, both 10% and 60% n-butanol concentrations show an increase in the polar symmetry strength which means there are more multilayer fullerenoid structures than in the 30% n-butanol concentration. Also, the polar symmetry strength value for 10% *n*-butanol was greater than 60%*n*-butanol, indicating that circular structures in 10%*n*-butanol were more ordered and less reactive. The reactivity of soot toward oxidizers with respect to the nanostructure can be explained upon the presence of short stacks and curvy structures [61]. Higher H/C ratios in short stacks imply higher possibility of H abstraction which is associated with high reactivity of soot particles. The presence of small curved structures in soot particles is assumed to enhance oxidation rates [62] regardless of its lower *H/C* ratio in comparison with planar structure. Recently, Raj et al. [61] showed the activation energy for the small curvy structure (curved PAH) was smaller than for the planar structure (planar PAH) which described higher reactivity of small curvatures.

As mentioned, by increasing orderliness in both polar and nematic structures, less layer planes with higher curvature exist. Based on the observation in section 3.3, the 30%*n*-butanol/70%*n*-dodecane blend showed the highest reactivity. The results of soot nanostructure analysis revealed the lowest degree of orderliness for this blend. The lowest symmetry strength (lowest ordering between other cases) indirectly suggested the reactivity of this case is attributed to the higher H/C ratios available in the very short carbon segments. This reactivity was followed by the 60%*n*-butanol/40%*n*-dodecane blend which showed an intermediate ordering. Its nanostructure was mostly comprised of layer plane with high curvature. This high curvy structure is less active than very short carbon segment and more active than planar or low curvy structure. The lowest reactivity was observed for the 10%*n*-butanol/90%*n*-dodecane blend. The highest symmetry strength (highest ordering) in this case implied the presence of layer plane with low curvature which has higher activation barriers for oxidation in comparison with layer plane with high curvature. The results of nanostructure analysis were consistent with our observation based on sooting stability in section 3.3. Accordingly, the degree of orderliness appears to be an indication of reactivity in soot sample.

3.4 Conclusions

The effect of *n*-butanol as an oxygenated compound in diesel surrogates was studied in a two-stage burner. Measuring changes in particle size and concentration showed that, when the *n*-butanol percentage increased, the amount of soot was reduced. On the other hand, the stability of soot exhibited a different behavior as the amount of *n*-butanol increased. Two different parameters were used to quantify our observation with regard to the soot formation and soot reactivity behavior. Sooting tendency (*ST*) was defined to show how the amount of soot formed in the flame was affected by *n*-butanol. Sooting stability (*SS*) was defined for quantifying the reactivity of soot particles during oxidation process. *ST* decreased by increasing the *n*-butanol percentage, as expected. On the other hand, *SS* decreased with increasing *n*-butanol percentage up to 30%. After this, there was an increase at 60% *n*-butanol. Even though the amount of soot was less at 60% *n*-butanol, it appeared to be more stable. Image analysis of the HRTEM images was used to identify the chemical mechanism involved with this observation. The results revealed that increasing *n*-butanol reduced interlayer spacing as well as the tendency of the blend to form soot. The polar and nematic symmetry analysis followed behavior of *n*-butanol/*n*-dodecane blends shown by sooting stability. Both sooting stability and symmetry reduced by increasing *n*-butanol from 10% to 30% and then increased at 60%. Soot derived from

30% *n*-butanol was found to be very reactive and had short carbon segments, implying higher *H/C* ratios. The soot derived from the 60% *n*-butanol blend was less active than the 30% *n*-butanol blend. Its nanostructure consisted of higher amount of layer planes with high curvature. This type of structure was less active than short carbon segments. The most stable soot between all blends was for 10% *n*-butanol blends which had higher amount of low curvy structures. In fact, the lowest reactivity of the 10% *n*-butanol blend derived soot suggested that layer plane with either low or zero curvature was less reactive than layer plane with high curvature.

3.5 References

[1] Braun, N. Shah, F.E. Huggins, K.E. Kelly, A. Sarofim, C. Jacobsen, Carbon 43 (2005) 2588.

[2] M. Knauer, M.E.. Schuster, D. Su, R. Schloegl, R. Niessner, N.P. Ivleva, Journal of Physical Chemistry A 113 (2009) 13871.

[3] X. Wu, F. Lin, H. Xu, D. Weng, Applied Catalysis, B: Environmental 96 (2010) 101.

[4] Carlos A. Echavarria, I.C. Jaramillo, A.F. Sarofim, J.S. Lighty, C.A. Echavarria, Combustion and Flame 159 (2012) 2441.

[5] .E. Penner, D.H. Lister, D.J. Griggs, D.J. Dokken, M. McFarland, Aviation and the Global Atmosphere: A Special Report of the Intergovernmental Panel on Climate Change (IPCC) Working Groups I and II, 1999.

[6] C. Esarte, M. Abián, Á. Millera, R. Bilbao, M.U. Alzueta, Energy 43 (2012) 37.

[7] K.I. Burshaid, M.A. Hamdan, Energy Conversion and Management 65 (2013) 751.

[8] P. Pepiot-Desjardins, R. Pitsch, H.; Malhotra, S.R. Kirby, A.L. Boehman, Combustion and Flame 154 (2008) 191.

[9] T. Kitamura, T. Ito, J. Senda, H. Fujimoto, JSAE Review 22 (2001) 139.

[10] M. Lapuerta, R. Garcia-Contreras, J. Campos-Fernandez, M.P. Dorado, Energy &

Fuels 24 (2010) 4497.

[11] S. Atsumi, T. Hanai, J.C. Liao, Nature 451 (2008) 86.

[12] E. Sukjit, J.M. Herreros, K.D. Dearn, R. García-Contreras, A. Tsolakis, Energy 42 (2012) 364.

[13] R. Lemaire, E. Therssen, P. Desgroux, Fuel 89 (2010) 3952.

[14] M. Yao, H. Wang, Z. Zheng, Y. Yue, Fuel 89 (2011) 2191.

[15] Q. Zhang, M. Yao, Z. Zheng, H. Liu, J. Xu, Energy 47 (2012) 515.

[16] K. Yehliua, R.L. Vander Wal, O. Armas, A.L. Boehman, Combustion and Flame 159 (2012) 3597.

[17] A.L. Boehman, J. Song, M. Alam, Energy & Fuels 19 (2005) 1857.

[18] J.P.A. Neeft, M. Makkee, J.A. Moulijn, Fuel Processing Technology 47 (1996) 1.

[19] K. Yamamoto, K. Yamauchi, Proceedings of the Combustion Institute 34 (2013) 3083.

[20] M. Knauer, M. Carrara, D. Rothe, R. Niessner, N.P. Ivleva, Aerosol Science and Technology 43 (2009) 1.

[21] D.M. Smith, M.S. Akhter, J.A. Jassim, C.A. Sergides, W.F. Welch, A.R. Chughtai, Aerosol Science and Technology 10 (1989) 311.

[22] F. Marcuccilli, P. Gilot, B. Stanmore, G. Prado, Symposium (International) on Combustion, [Proceedings] 25 (1994) 619.

[23] R.L. Vander Wal, C.J. Mueller, Energy & Fuels 20 (2006) 2364.

[24] J. Song, M. Alam, A.L. Boehman, U. Kim, Combustion and Flame 146 (2006) 589.

[25] C.J. Mueller, W.J. Cannella, T.J. Bruno, B. Bunting, H.D. Dettman, J.A. Ranz, M.L. Huber, M. Natarajan, W.J. Pitz, M.A. Ratcliff, K. Wright, Energy Fuels 26 (2012) 3284.

[26] W.J. Pitz, C.J. Mueller, Progress in Energy and Combustion Science 37 (2011) 330.

[27] B.D. Gould, X. Chen, J.W. Schwank, Journal of Catalysis 250 (2007) 209.

[28] O. Dogan, Fuel 90 (2011) 2467.

[29] K.G. Neoh, J.B. Howard, A.F. Sarofim, Particulate Carbon Formation During Combustion, Plenum Press, New York, 1981.

[30] K.G. Neoh, J.B. Howard, A.F. Sarofim, in:, Twentieth Symposium (International) on Combustion, The Combustion Institute, Pittsburgh, 1985, pp. 951–957.

[31] C.A. Echavarria, A.F. Sarofim, J.S. Lighty, A. D'Anna, Combustion and Flame (2011) 98.

[32] C.J. Merrill, The Oxidation and Fragmentation of Soot in a Two-Stage Burner, University of Utah, 2005.

[33] C.A. Echavarria, A.F. Sarofim, J.S. Lighty, A. D'Anna, Proceedings of the Combustion Institute (2009) 705.

[34] C.A. Echavarria, I.C. Jaramillo, A.F. Sarofim, J.S. Lighty, Proceedings of the Combustion Institute 33 (2011) 659.

[35] D.C.S. McEnally, U.O. Koylu, L.D. Pfefferle, D.E. Rosner, Combustion and Flame 109 (1997) 701.

[36] P. Minutolo, A. D'Anna, M. Commodo, R. Pagliara, G. Toniato, C. Accordino, Environmental Engineering Science 25 (2008) 1357.

[37] R.A. Dobbins, C.M. Megaridis, Langmuir 3 (1987) 254.

[38] P. Toth, A.B. Palotas, E.G. Eddings, R.T. Whitaker, J.S. Lighty, Combustion and Flame 160 (2013) 909.

[39] P. Toth, A.B. Palotas, E.G. Eddings, R.T. Whitaker, J.S. Lighty, Combustion and Flame 160 (2013) 909.

[40] P. Toth, Á.B. Palotás, J. Lighty, C.A. Echavarria, Fuel 99 (2012) 1.

[41] D. Gabor, Journal of the Institution of Electrical Engineers III: Radio and Communication Engineering 93 (1946) 429.

[42] A.B. Palotas, L.C. Rainey, C.J. Feldermann, A.F. Sarofim, J.B. Vander Sande, Microscopy Research and Technique 33 (1996) 266.

[43] H.S. Shim, R.H. Hurt, N.Y.C. Yang, Carbon 38 (2000) 29.

[44] C.K. Westbrook, W.J. Pitz, H.J. Curran, J. Phys. Chem. A 110 (2006) 6912.

[45] A. D'Anna, A. Ciajolo, M. Alfe, B. Apicella, A. Tregrossi, Proceedings of the Combustion Institute 32 (2009) 803.

[46] C.S. McEnally, L.D. Pfefferle, Environmental Science and Technology 45(6) (2011) 2498.

[47] Y. Yang, A.L. Boehman, R.J. Santoro, Combustion and Flame 149 (2007) 191.

[48] C.S. McEnally, L.D. Pfefferle, Combustion and Flame 148 (2007) 210.

[49] T. Kitamura, T. Ito, J. Senda, H. Fujimoto, International Journal of Engine Research 3 (2002) 223.

[50] R.L. Vander Wal, V.M. Bryg, M.D. Hays, Journal of Aerosol Science 41 (2010) 108.

[51] M.E. Schuster, M. Haevecker, R. Arrigo, R. Blume, M. Knauer, N.P. Ivleva, D.S. Su, R. Niessner, R. Schloegl, Journal of Physical Chemistry A 115 (2011) 2568.

[52] L.A. Langley, D.E. Villanueva, D.H. Fairbrother, Chemistry of Materials 18 (2006) 169.

[53] G. Barco, A. Maranzana, G. Ghigo, M. Causa, G. Tonachini, Journal of Chemical Physics 125 (2006) 194706/1.

[54] J.P. Cain, P.L. Gassman, H. Wang, A. Laskin, Physical Chemistry Chemical Physics 12 (2010) 5206.

[55] C. Esangbedo, A.L. Boehman, J.M. Perez, Tribology International 47 (2012) 194.

[56] H.P. Boehm, Carbon 40 (2002) 145.

[57] P.R. Buseck, B. Huang, L.P. Keller, Energy & Fuels 1 (1987) 105.

[58] A.B. Palotas, L.C. Rainey, A.F. Sarofim, J.B. Van der Sande, P. Ciambelli, Energy & Fuels 10 (1996) 254.

[59] C.R. Shaddix, A.B. Palotas, C.M. Megaridis, M.Y. Choi, N.Y.C. Yang, International Journal of Heat and Mass Transfer 48 (2005) 3604.

[60] M. Lapuerta, F. Oliva, J.R. Agudelo, A.L. Boehman, Combustion and Flame 159 (2012) 844.

[61] A. Raj, S.Y. Yang, D. Cha, R. Toyouo, S.H. Chung, Combustion and Flame (2013).

[62] R.L. Vander Wal, A.J. Tomasek, Combustion and Flame 134 (2003) 1.

CHAPTER 4

OXIDATIVE BEHAVIOR OF SOOT DERIVED FROM BIODIESEL/DIESEL AND ALCOHOL/DIESEL SURROGATE FLAMES

4.1 Introduction

Biofuels derived from natural and renewable resources offer the potential to completely or partially substitute conventional fuel. Currently, there has been a worldwide effort toward increased usage of biofuels. In Europe, the EU guideline 2009/28/EG (renewable energy directive) requires blending of up to 10% of biofuel with fossil fuel through 2020. There are a variety of biofuels potentially available, but the main biofuels being considered are biodiesel and bioalcohol [1]. Among bioalcohols, ethanol is the most widely produced and used species. However, ethanol is not an ideal fuel because of its lower energy density and its hygroscopicity which cause a number of problems for storage and distribution. Higher alcohols ($C4H9OH$ and $C5H11OH$) do not have the current problems of ethanol [2–4]. However, only butanol has the potential to be produced from renewable sources with higher yields, to make it viable as a fuel substitute [5,6].

Biodiesel from renewable sources consists of mono-alkyl esters of fatty acids, which are typically methyl esters, referred as fatty acid methyl esters (FAME). Biodiesel blended fuels have been proven to enhance diesel particulate filter (DPF) performance

[7–9]. Numerous studies, both experimental and numerical, have shown that the presence of oxygen in fuels reduces soot formation [10–13]. Some of these studies have confirmed that the type of oxygen functional group and the relative position of an oxygen molecule within the structure of the fuel molecule are important factors in the sooting tendency reduction. However, those studies that evaluated the sooting tendency of oxygenated fuels by using laboratory-scale flame burners are limited [14]. Tran et al. [15] analyzed sooting tendencies of soybean biodiesel-diesel blends (0-20% by volume of biodiesel) by laser-based measurements of soot generated from a wick-fed lamp. The results showed that the sooting tendency was reduced by increasing the biodiesel concentration. The most comprehensive study in the literature was made by Pepiot-Desjardins et al. [11], who showed that adding even small quantities of oxygenates to diesel fuels would generate significant reductions of soot emissions. McEnally and Pfefferle [12] measured the sooting tendencies of 186 oxygenated hydrocarbons. They concluded that sooting tendencies depend strongly on the direct chemical effects of oxygenate structures.

Several studies have been performed to investigate the influence of oxygenates on the oxidative reactivity of soot [8,16–18]. Boehman et al. [49] conducted experiments to investigate the oxidative reactivity of soot generated from biodiesel in addition to the regular diesel fuels (low and high sulfur). Their results showed a potential impact of biodiesel blending on the low-temperature oxidation characteristics of soot. Song et al. [8] studied soot reactivity derived from ultra-low sulfur diesel (ULSD), neat biodiesel (B100), Fischer-Tropsch diesel fuel (FT100) and ULSD blended with 20% biodiesel. Their thermogravimetric study (TGA) demonstrated that B100 derived soot was found to be significantly more reactive than FT100 derived soot. Jaramillo et al. [16] applied TGA analysis to obtain the oxidation kinetic rates of soot derived from different fuels, including pure n-dodecane, pure n-butanol, and their mixtures. Their results revealed that the inherent nanostructure of the particulates had an influence on the oxidative reactivity. Soot can be oxidized when it reacts with molecular oxygen (*O_2*), oxygen radical (*O*), and hydroxyl radical (*OH*) [19–23]. For O_2 , the global mechanism is that of NSC [23]. NSC expression was obtained by fitting the experimental data with a kinetic expression over a temperature range from 1273 to 2273 K at O_2 partial pressures of 0.1 – 0.6 bar for pyrolytic graphite. This expression is given as follows:

$$W\left(\frac{gr}{cm^2 s}\right) = 12\left(\left(\frac{k_A P_{O2}}{1 + k_Z P_{O2}}\right)x + (1-x)\, k_B P_{O2}\right) \tag{4.1}$$

where k_A , k_Z and k_B are temperature-dependent kinetic reaction constants given in Table 4.1, P_{O2} is the partial pressure of O_2, and $x = \left(1 + \frac{K_T}{K_B P_{O2}}\right)^{-1}$ is the fraction of the surface covered with *A* type reaction sites.

For *OH*, Neoh et al. [34] considered a two-stage burner where the soot-laden combus-

Table 4.1. Empirical parameters for Nagle and Strickland-Constable Model, $k = A\, exp(-E/RT)$

Rate Constant	E, kcal/mole	A	Units for A
k_A	30	20	$g\, cm^{-2} s^{-1} atm^{-1}$
k_B	15.2	4.46×10^{-3}	$g\, cm^{-2} s^{-1} atm^{-1}$
k_T	97	4.46×10^{-5}	$g\, cm^{-2} s^{-1}$
k_Z	21.3	21.3	$g\, cm^{-2} s^{-1} atm^{-1}$

tion gases from the first stage were mixed with air and burned in the second stage. Their analysis of soot oxidation in several $CH_4/O_2/N_2$ flames showed that the main reactant under the conditions studied (1580-1860 K; 1 atm; 10^{-5}-0.05 mole fraction O_2) was OH, with a collision efficiency of 0.1 to 0.4 carbon atoms removed per collision. Neoh's kinetic expression is given by:

$$W\left(\frac{gr}{cm^2 s}\right) = 1.29 \times 10^2\, \Gamma_{OH} \frac{P_{OH}}{\sqrt{T}} \tag{4.2}$$

In this study, the value of 0.13 for collision efficiency was used. The current study focuses on the understanding of oxidative reactivity of soot derived from the addition of biodiesel and alcohol surrogates to diesel surrogates in a flame temperature. A two-stage burner was used to isolate the formation step from the oxidation. The PSDs were measured and oxidation rates were calculated for methyl decanoate/n-dodecane (biodiesel/diesel surrogate) and n-butanol/n-dodecane (alcohol/diesel surrogate) mixtures. Two of the most commonly used soot oxidation models, Neoh‘s expression [21,24] to account for soot oxidation by OH and the NSC's [23] expression to determine O_2 soot oxidation, were calculated and compared to the experimental data.

4.2 Experimental setup and method

The experimental setup is schematically shown in Figure 4.1. The experiments were carried out in a two-stage burner used in previous studies [18,25–27]. The liquid-fuel mixture was injected into the vaporizer (V-1) by using a syringe pump (KDS-410). The vaporized fuel and air stream (A-1) were mixed in the manifold (M-1) and then passed to

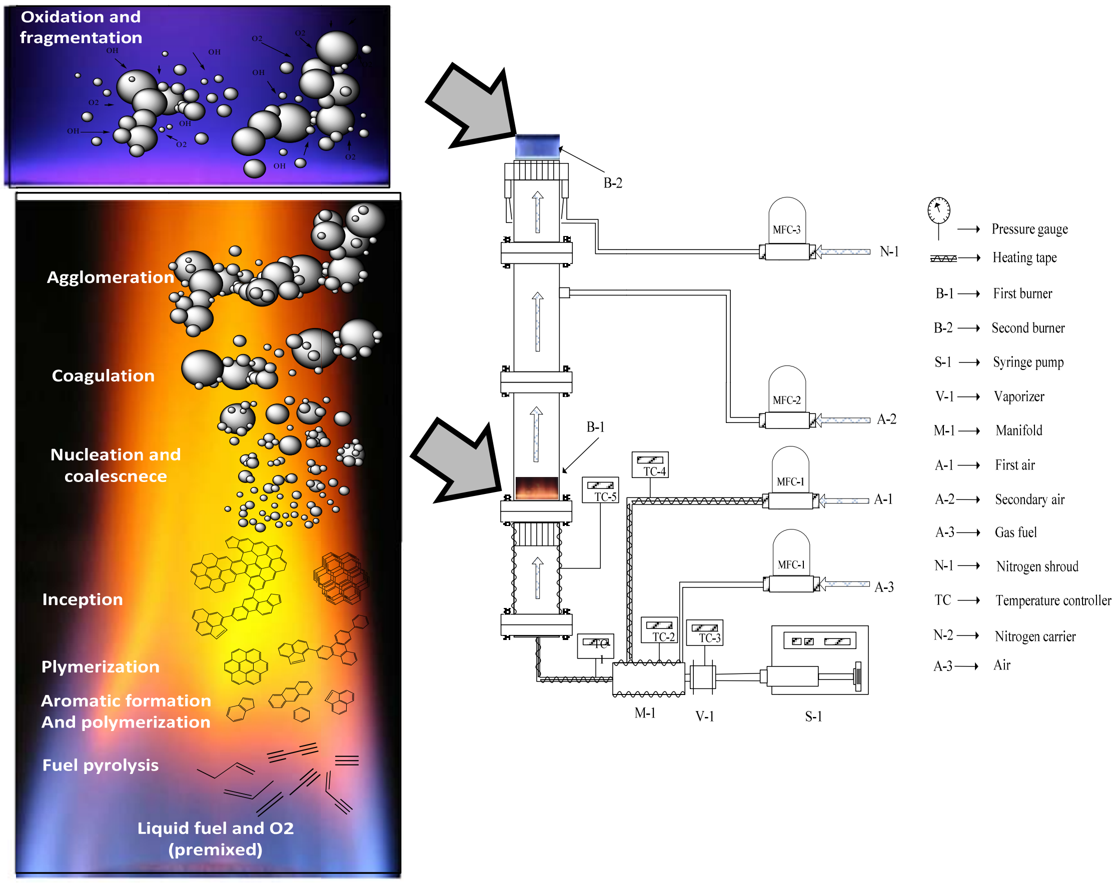

Figure 4.1. Schematic representation of the two-stage burner. History of soot formation and oxidation is illustrated to the left (adapted from Bockhorn [19]).

the premixed section of the first-stage burner (stainless steel pipe, 51 mm ID, Schedule 80, 127-mm long). The first burner was operated fuel-rich to ensure the formation of soot particles. A secondary oxidizer stream (A-2) entered the premixed chamber before the secondary flame. Soot particles formed in the first burner were oxidized in the second premixed flat-flame burner. A nitrogen shroud on the secondary burner was used to shield the flame from excess oxygen diffusion from the surroundings.

Surrogate fuels were used to represent diesel and biodiesel fuels, since diesel fuels typically consist of hundreds of compounds. This makes it easier to determine the effects of fuel composition on combustion properties [28]. Methyl decanoate is a large methyl ester that was used as a surrogate for biodiesel as proposed by Herbinet et al. [29,30] and has also been used by other studies [31–34]. n-Dodecane was selected as a diesel surrogate, as was done in other studies [28,35,36]. The mixture of methyl decanoate/n-dodecane represented the mixture of biodiesel/diesel. Alcohol/n-butanol mixed with n-dodecane, was chosen to represent alcohol/diesel fuels. Table 4.2 shows the experimental conditions for the study.

Temperature, particle size distributions (PSDs), and specific gas-phase compounds were measured for all fuel mixtures. All measurements were performed in the centerline of the flame at different heights above the secondary burner (HABs).

The flame temperature was measured using an uncoated 0.2032-mm Pt/Rh 70%/30% thermocouple (Type B). The radiation correction for the temperature was similar to that of McEnally et al. [37].

PSDs were measured using a scanning mobility particle sizer (SMPS) including a TSI 3080 classifier and a 3025 ultrafine condensation particle counter coupled to a 3085 nano-DMA. The SMPS was optimized to operate in the 3-135 nm range with a sheath

Table 4.2. Experimental conditions.

#	Fuel	$\emptyset_1^a$	$\emptyset_{\text{Overall}}^b$	ϑ^c	C/O
C1	30% n-butanol/ 70% n-dodecane	2.2	1.1	3.5	0.70
C2	60% n-butanol/ 40% n-dodecane	2.2	1.1	3.5	0.68
C3	30% methyl decanote/ 70% n-dodecane	1.85	1.05	4.5	0.60
C4	30% methyl decanote/ 70% n-dodecane	1.85	1.05	6	0.60
C5	60% methyl decanote/ 40% n-dodecane	1.76	1	6	0.56

[a] Equivalence ratio in the first burner
[b] Overall equivalence ratio
[c] Cold gas velocity, cm/s (STP)

flow of 15 L/min and an aerosol sample flow of 1.5 L/min. The SMPS sampling system was similar to that used by Zhao et al. [38]. The validity and reliability of the SMPS sampling procedure and data acquisition have been extensively discussed [38,39]. The sampling probe was placed horizontally above the burner with the orifice faced down toward the flame above the burner. The probe was mounted on a translation stage with the accuracy of probe positioning estimated to be 0.1 mm. The soot-laden gas sample was immediately diluted by nitrogen at the rate of 30 L/min (STP) to quench oxidation reactions, and minimize particle coagulation and thermophoretic deposition. Zhao et al. [38] showed that particle diffusion losses and particle coagulation can be minimized by systematically increasing the dilution ratio to a critical value where the particles size distribution function becomes independent of the dilution ratio. The pressure difference across the probe orifice was adjusted with the aid of two U manometers to obtain a desired dilution ratio. The corrections for penetration efficiency into the probe and probe orifice and diffusion losses during transport were applied following the procedure presented by Minutolo et al. [40].

The evolution of the combustion gas-phase species was isokinetically sampled by a system involving a water-cooled probe which was coupled to a particle filter and a chiller for removing particles and water before entering an online micro gas-chromatography analyzer micro-GC (VARIAN, CP-4900). Similar to the SMPS sampling probe, the GC probe was pointed down toward the incoming flame gas above the burner. It was mounted on a translation stage so that its vertical position could be varied with respect to the burner. The accuracy of the probe positioning was estimated to be around 0.1 mm.

4.3 Results and discussion

4.3.1 Temperature profiles

Radiation-corrected temperature profiles for all fuel blends, as a function of height above the burner (HAB), are given in Figure 4.2a and 4.2b. Figure 4.2a shows temperature profiles for all methyl decanoate/n-dodecane mixtures and Figure 4.2b shows n-butanol/n-dodecane mixtures [18]. The error bars are the result of either uncertainty in the sampling process or due to limitations in the precision of measuring devices.

The 6 cm/s methyl decanoate/n-dodecane flames, C4 and C5, had higher temperature peaks which were shifted toward the surface of the burner, as compared with C3, the 4.5 cm/s flame. Increasing the cold gas velocity stabilized the flames on the secondary burner. This is evidenced by the lower uncertainty of the temperature measurements in C4 and C5 versus C3. A comparison between temperatures of n-butanol/n-dodecane mixtures (C1, C2) and methyl decanoate/n-dodecane mixtures (C4, C5) shows similar peak temperatures that were slightly shifted toward higher HABs for butanol mixtures, C1 and C2. Unlike methyl decanoate/n-dodecane mixtures where the peak temperature

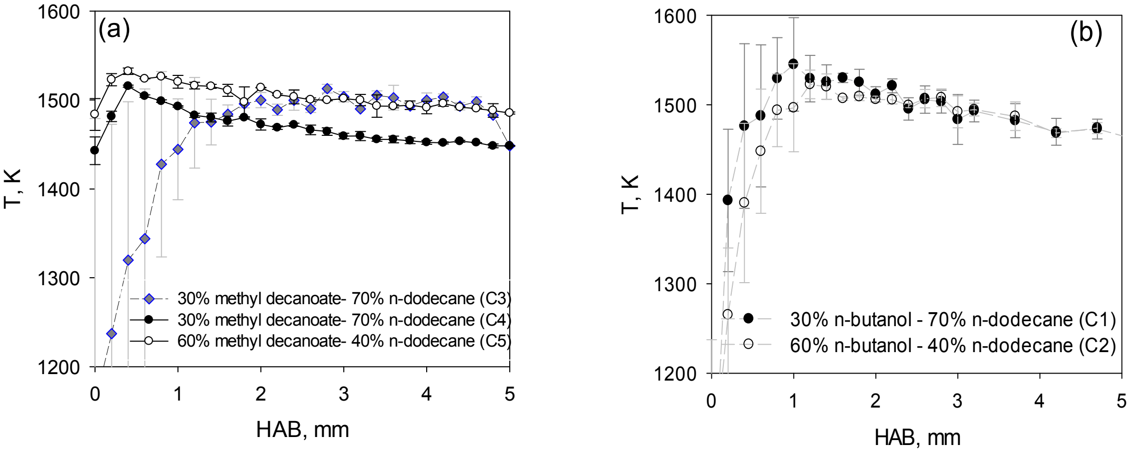

Figure 4.2. Temperature profiles for all five flames

rose by increasing the methyl decanoate percentage, in the n-butanol/n-dodecane mixtures, the peak temperature decreased by increasing n-butanol percentage.

4.3.2 PSDs measurement

The PSDs as a function of HAB are shown in Figure 4.3. The maximum mobility size for both butanol fuel mixtures immediately on the burner was around 80 nm. The PSDs for 30% n-butanol fuel consisted of a higher number of larger particles versus 60% n-butanol mixtures which were mainly dominated by smaller particles. The red line depicted on the PSD plots demonstrates this difference. The PSDs did not significantly change until 2.2 mm for 30% n-butanol mixture and 3.2 mm for 60% n-butanol mixture. After these heights, the considerable change in the PSDs indicated the oxidation region, as evidenced by a reduction in number and size of particles. At higher HAB, around 5 mm, the PSDs did not undergo any noticeable change, indicating that oxidation was hindered. Interestingly, PSDs for 60% n-butanol flame reached a larger distributions than 30% n-butanol flame at higher elevation (after oxidation), although it was initially smaller than 30% n-butanol flame. This behavior indicated a higher oxidative reactivity of soot derived from 30% n-butanol mixture. An extensive discussion was given in the previous chapter regarding the effect of nanostructure on the oxidative reactivity of soot from these two fuels. PSDs measured for three diesel/biodiesel surrogate flames are also given in Figure 4.3. In C3 and C4 flames, the same fuel (30%methyl decanoate/70%n-dodecane) was burned under the same equivalence ratios while the cold gas velocity was different from the previously-discussed mixtures. It was found that increasing the cold

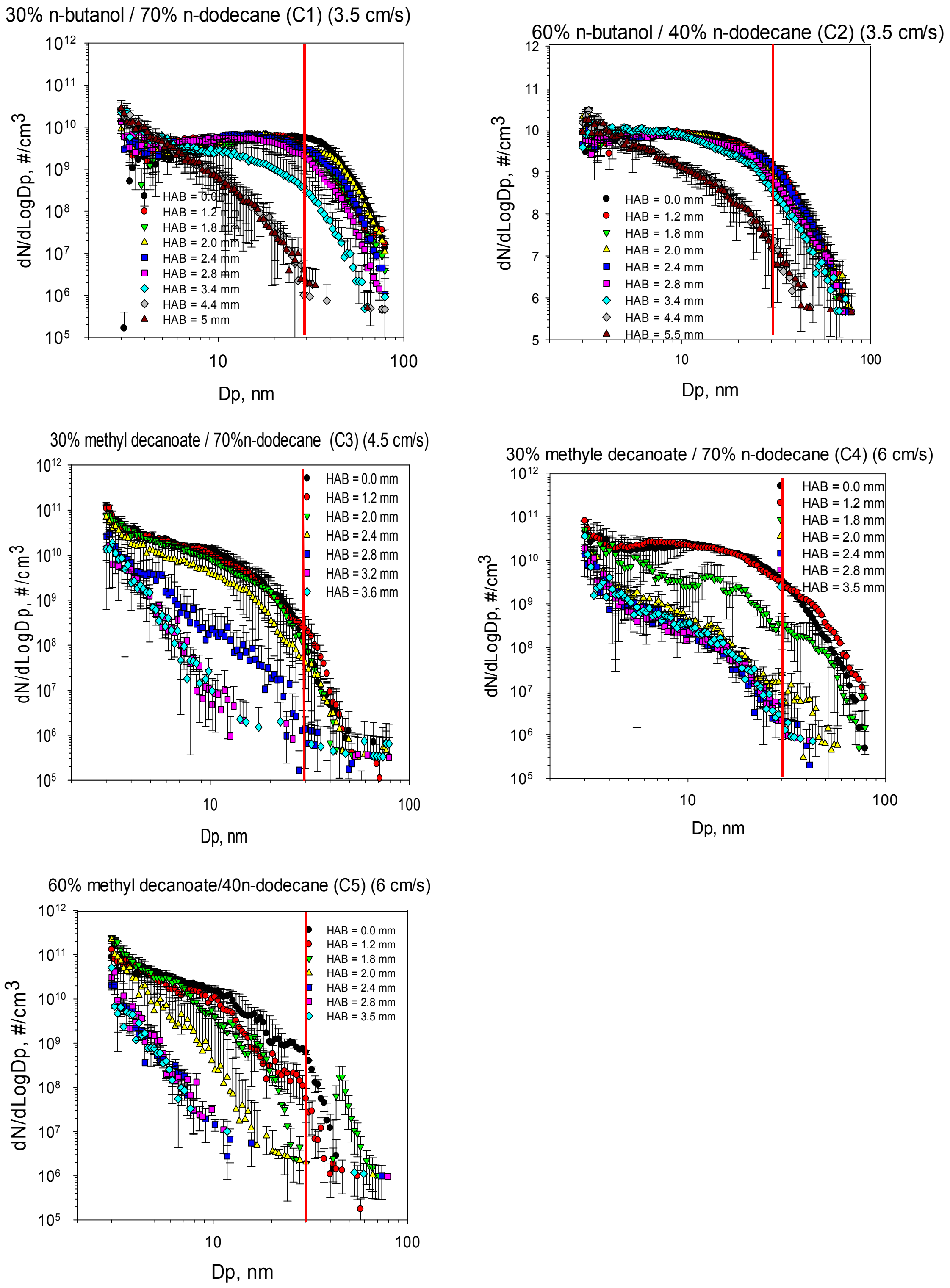

Figure 4.3. PSDs at selected heights above the burner. The red line depicted at 30 nm to better differentiate between PSDs.

gas velocity resulted in slightly larger particles. This behavior was attributed to the effect of cold gas velocity on the formation step in the first-stage flame. Close to the burner surface, maximum mobility size was initially observed for C4 to be ~80 nm and ~60 nm for C3. The red lines on these plots help distinguish between PSDs. PSDs did not undergo considerable change until a certain height was reached, approximately 2.6 mm for C3 and 1.8 mm for C4. The oxidation started at a lower height for C4 because its higher cold gas velocity resulted in a higher peak temperature which occurred closer to the burner surface. For the same velocity, increasing the amount of methyl decanoate in n-dodecane from 30% (C4) to 60% (C5) resulted in smaller PSDs. The maximum value of the initially measured mobility size for 60% methyl decanoate mixture (C5) was ~60 nm versus ~80 nm for 30% methyl decanoate (C4). Similar to C4 flame, the PSDs did not change until it reached the height of 1.8 mm. After 1.8-mm, a significant change in burning indicated the initiation of oxidation. The early oxidation is consistent with its peak temperature occurring in the earlier height. In all cases, methyl decanoate mixtures (C3, C4, and C5) showed a lower tendency to form soot as compared to butanol mixtures.

Figure 4.4 shows the average mobility size obtained by the Sauter mean diameter formula versus residence time to give a better understanding of size change behavior during the oxidation process. The comparison between C4 and C5 (methyl decanoate flames with the similar velocity conditions) indicated that 30% methyl decanoate had a larger average size (~20 nm) than 60% methyl decanoate flame (~10 nm), initially on the burner. This difference in the initial sizes demonstrated the strong influence of methyl decanoate as an oxygenated fuel in suppressing the soot formation. Some studies have shown that the oxygen molecules in the fuel structure remained bonded to carbons,

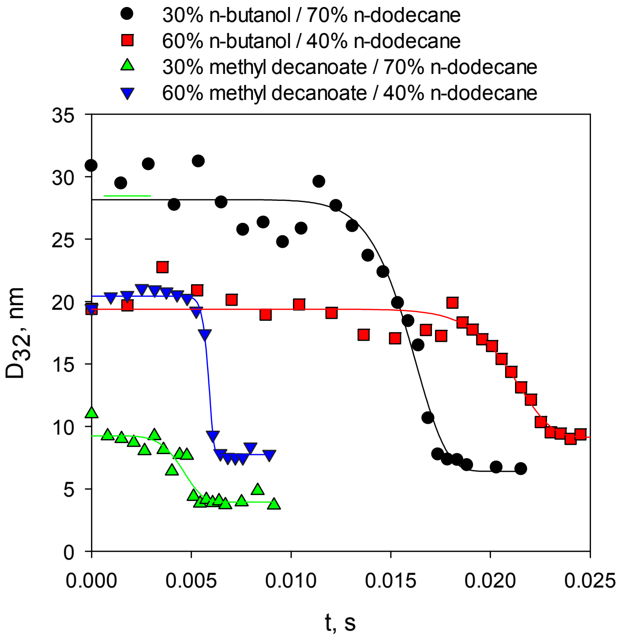

Figure 4.4. Variation in D32 at different HABs for fuel blends.

preventing these carbons from becoming available for soot precursors [41–44]. As shown by other studies [44,45], the early CO_2 production during oxidation of methyl decanoate is due to the direct CO_2 formation from the ester group.

After reaching a certain height, the average size sharply dropped for both fuel mixtures implying the region of the flame that *OH* was formed and oxidation occurred. After the oxidation zone, the final average size for 30% methyl decanoate (C4) was around 9 nm versus 4 nm for 60% methyl decanoate (C5) flame. Burning occurred much faster for methyl decanoate mixtures evidenced by their shorter residence time. This was attributed to the higher cold gas velocity for these mixtures.

On the other hand, the initial average size for 30% n-butanol (C1) mixture was around 30 nm and around 20 nm for 60% n-butanol (C2). This reduction in the initial average size also indicated the effect of n-butanol in suppressing soot formation but to a smaller extent as compared to methyl decanoate flames. A significant size reduction occurred in the oxidation region over a longer period of time.

4.3.3 Gas-phase species measurement and model

One may suspect that a faster burning of soot from methyl decanoate fuels may be the result of a higher concentration of oxidizer species such as O_2 and OH. To investigate this further, GC measurements were performed, coupled with kinetic modeling. Temperature profiles were input into a CHEMKIN [46] simulation to eliminate the need to model heat losses in the energy equation. Other experimental measurements at the surface of the top burner (mass flow rate, H_2, CO, CO_2, O_2 concentration) were also used as inputs. CHEMKIN modeling coupled a 1D-premixed code to GRI kinetic model [47]. The model results were shifted downstream to account for cooling due to the sampling probe [38,48]. Figure 4.5 shows the concentration profiles of OH radical and other gas species. Based on the model results, OH radical started to form and it reached a maximum in the region where O_2 dropped. The concentration of OH then leveled off consistent with the trend of the PSDs obtained in the second burner. The evolution of gas species was similar for both 30% n-butanol (C1) and 60% n-butanol (C2) mixtures. The two methyl decanoate flames at higher velocities (C4, C5) also showed similar gas species profiles. C3, at a lower velocity, had a slightly smaller OH profile than the other two cases since it had a lower temperature.

The comparison between n-butanol flames and methyl decanoate flames demonstrated that the gas species of later flames started leveling off sooner, consistent with the previous observation of average particle size (as illustrated in Figure 4.4). The modeling results show that n-butanol flames led to a slightly higher OH profile. Initially, higher

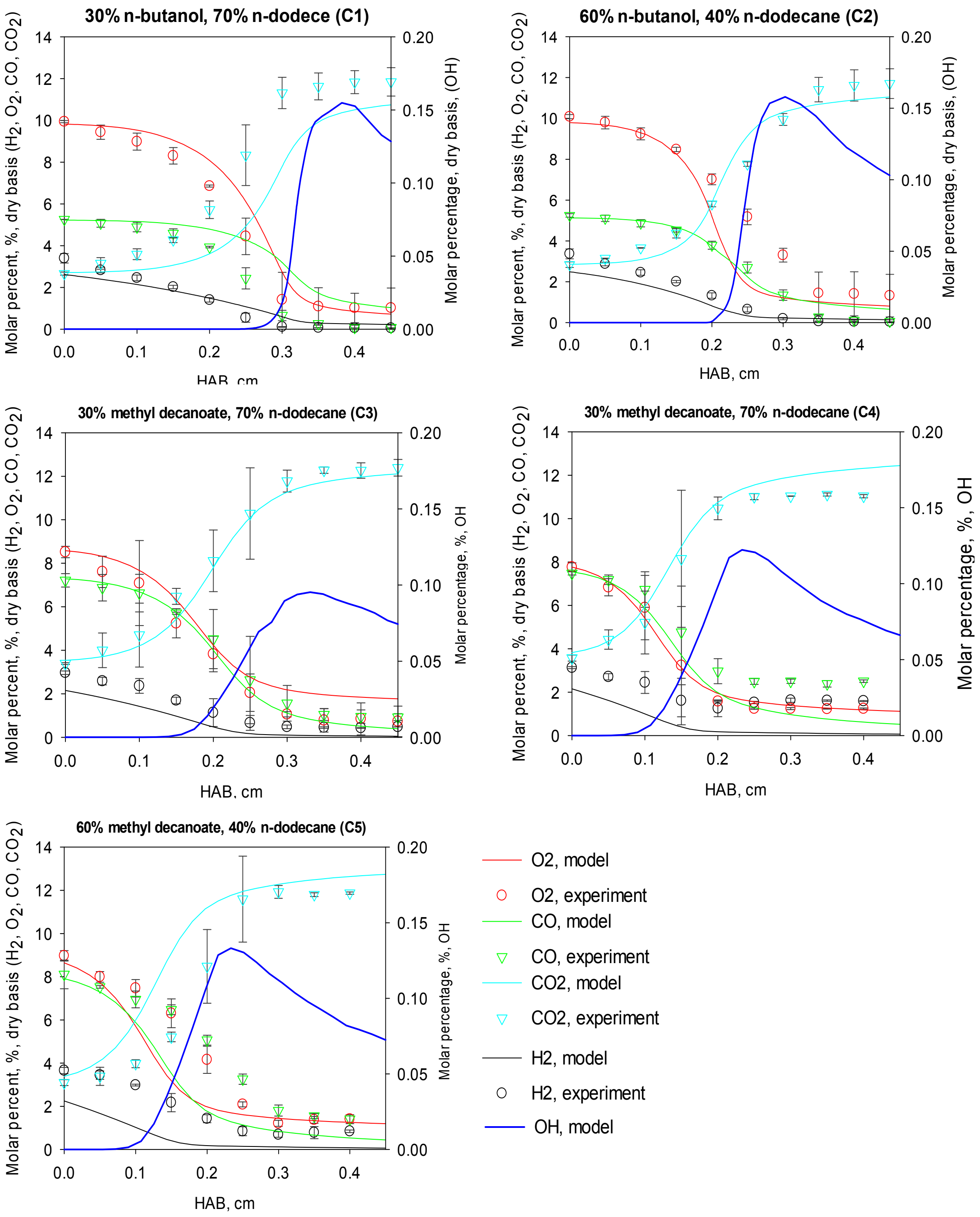

Figure 4.5. Concentration versus HAB for major gas-phase species in the second burner (left axis). The *OH* concentration scale is shown on the right axis. Symbols correspond to experimental results and solid and lines correspond to the model predictions.

concentrations of O_2 and less CO were evident in the n-butanol flames as compared with methyl decanoate flames. This may be the result of burning characteristics of n-butanol and methyl decnoate in the first burner. Basically, CO_2 formation from CO oxidation is significantly suppressed in methyl decanoate flames, because CO_2 is formed directly by decarboxylation of the ester functional group [44].

4.3.4 Soot oxidation rate

As shown in Figure 4.5, n-butanol mixtures showed a higher OH profile. One may ask whether having a higher OH profile would lead to a higher oxidation rate. Soot oxidation rates based on the experimental PSDs were calculated by using:

$$W = \frac{1}{A}\frac{dm}{dt} \quad (\frac{gr}{cm^2.s}) \tag{4.3}$$

where A is the available surface area of soot particles per unit volume of gas (cm^2 /cm^3), m is the total soot mass per unit volume of gas, and t is time. PSDs were integrated to provide measures of the area and mass concentration. Mass concentration was characterized by assuming spherical particles, and accounting for the change in particle density with particle diameter [49]. The results for W calculated by Eq. (1) are presented in Figure 4.6. A number of models and mechanisms have been proposed for the soot oxidation rate [21,23,50–56] and their applicability is questionable under conditions by which they were originally formulated. The most widely used model for soot oxidation with O_2 was proposed by NSC. For OH oxidation, the equation by Neoh is used. Neoh's model predicts the oxidation rate in term of OH concentration, temperature, and collision

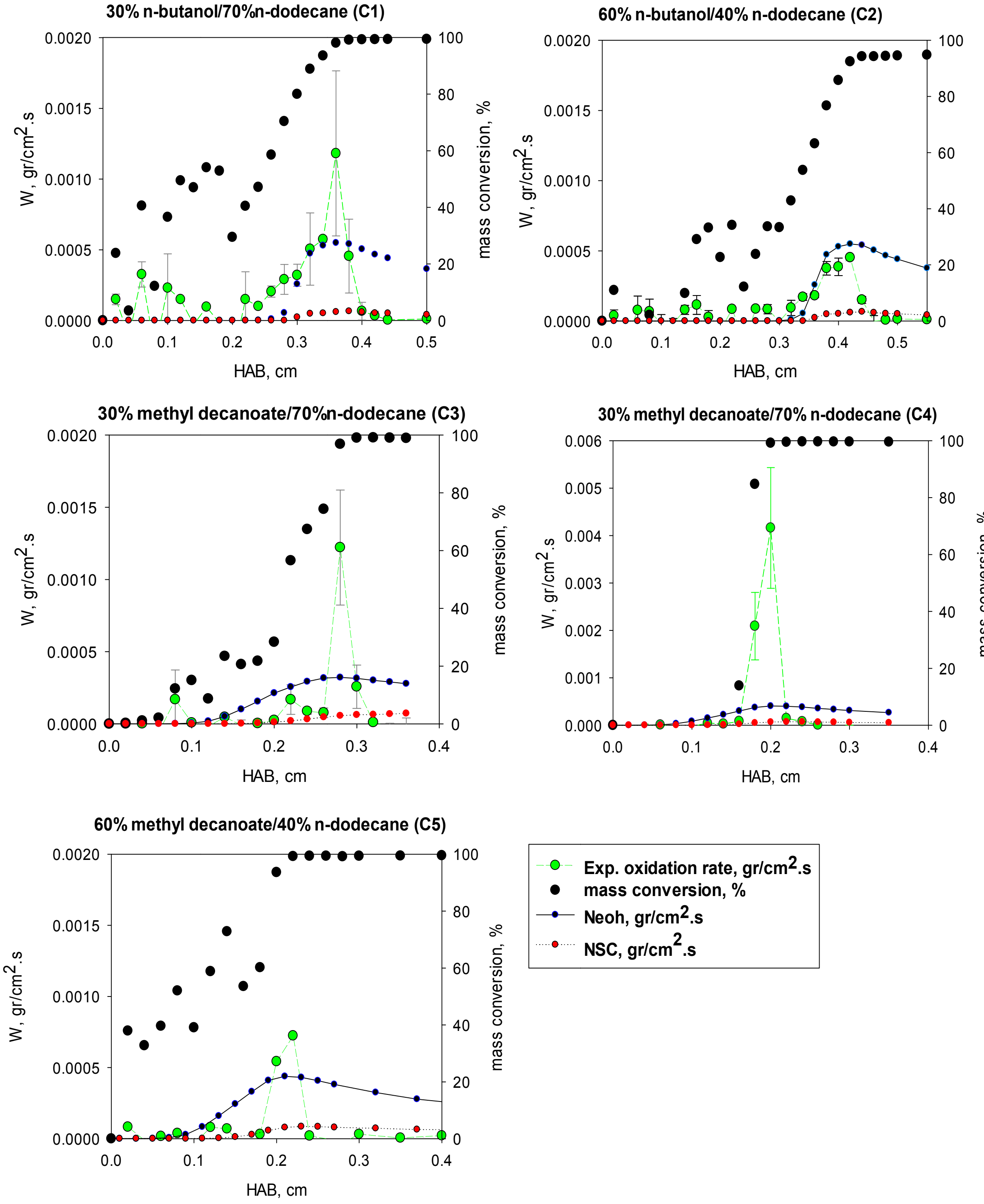

Figure 4.6. Comparison of experimental oxidation rates, Neoh's model, and NSC's model. Soot mass conversion is also given. Any negative values in *W* are set to zero. The left y-axis is oxidation rate and the right one is soot mass conversion. Note y-axis for all plots has a similar scale except from C4.

efficiency. In agreement with earlier work by Fenimore and Jones [51], Neoh showed that the main oxidative reactant was found to be *OH*, with a collision efficiency of 0.1 to 0.4 carbon atoms removed per collision. In our calculations, collision efficiency 0.13 was used, which is the most common value. In addition to the experimental rates, the oxidation rates predicted by Neoh [24] and NSC [57] were also determined for all flames.

The corresponding modeling of the burner system (Figure 4.5) showed that, close to the burner surface, the flame was dominated by H_2 and *CO* and O_2 (oxidizer). Once they started to burn, *OH* radicals were formed. Figure 4.6 is a plot of soot mass conversion versus soot oxidation rate. Soot mass conversion is determined by the ratio of the instantaneously converted amount to the initial amount for all cases based on the following formula,

$$mass\ conversion, \% = (1 - \frac{m_i}{m_0}) \times 100 \tag{4.4}$$

where m_i is the total soot mass per unit volume at any height above the burner and m_0 is the total soot mass per unit volume at HAB = 0 cm. The mass of soot at any height is given in Appendix D.

The comparison between n-butanol fuels showed that the maximum instantaneous experimental oxidation rate for 30% n-butanol flame (C1) was almost three times greater than the maximum oxidation rate for 60% n-butanol (C2) [27]. Some studies have shown the role of surface functionalities in the oxidative reactivity [58,59]. Smith et al. [59] showed that soot reactivity depends on the oxygen and hydrogen functionalities attached to the soot surface.

This increased reactivity was attributed to the reduced energy requirement to remove the oxygen as CO or CO_2 in comparison to regular oxidation of the carbon site. In contrast, Song et al. [60] reported a similarity between the oxygen functional groups of soot derived from n-heptane and ethylene in a laminar diffusion flame burner. The results given in Appendix C revealed that the soot surface functionalities were similar for soot derived from both fuel mixtures, indicating that n-butanol undergoes dehydration, decomposition, and dehydrogenation to form PAH precursors and oxygenated intermediates that finally oxidize to CO and CO_2 and do not contribute in the soot surface [61]. In the previous chapter, it was shown that the variation in the oxidative reactivity of soot from n-butanol flames was affected by the initial soot nanostructure.

The difference in soot oxidation rates was not captured by Neoh's expression, although OH concentration and temperature for both of these flames were similar. The oxidation rate due to O_2 estimated by NSC expression revealed that the contribution of O_2 was apparently small for both flames, consistent with previous studies [57,62–64].

The maximum instantaneous oxidation rate for 30% methyl decanoate flame (C4) was 5 times higher than 60% methyl decanoate flame (C5) despite having a similar temperature and oxidizer species (OH and O_2). This suggests that increasing the amount of methyl decanoate may not be able to enhance soot oxidative reactivity. Graboski et al. [65] reported that volatile organic fraction (VOF) is substantially increased in biodiesel blends. VOF influences micropore development and oxidation by providing an increase in internal surface area due to micropore opening. However, Boehman et al. [9] tested the soot reactivity by eliminating VOF via temperature-programmed oxidation (TPO) in the thermogravimetric analysis. Their results of biodiesel and diesel fuels demonstrated that the higher oxidative reactivity for soot in biodiesel is because of more amorphous and disordered soot nanostructure. Soot nanostructure has been shown to be an important factor in determining the oxidative reactivity [16,18,64,66,67]. It has been shown that the flame conditions and the fuel source impact the nanostructure of soot, and subsequently its oxidative reactivity [16,18,64]. Similar to n-butanol flames, Neoh's expression predicted a similar oxidation rates for C4 and C5 since they had a similar *OH* and temperature profiles. Because C3 had a lower temperature and *OH* concentration, Neoh predicted the oxidation rate for this flame slightly lower than that predicated for C4. These results imply that only considering *OH* concentration and temperature is not enough to predict the soot oxidation. NSC also predicted a small contribution of O_2 in the oxidation region for these three flames. The results suggest that there is currently a significant need to have an oxidation model which can take into account different soot reactivities.

The comparison of oxidation rates between n-butanol flames and methyl decanoate flames showed that with approximately the same molar percentage of oxygenated, methyl decanoate flames had higher instantaneous oxidation rates despite the fact that they had lower *OH* concentrations. The difference in the reactivity is likely due to the difference in combustion characteristics and soot formation process between n-butanol and methyl decanoate.

Based on the soot mass conversion plotted for all flames, typically two regions can be distinguished (see orange ovals in C1 flame). The first region is the pre-flame zone where only oxidizer available is O_2. The second region is in the reaction zone where temperature reaches its peak value and *OH* radical started to form and almost no O_2 is available. The oxidation rates reached their maximum value in the reaction zone when the *OH* concentration reached its peak, which is consistent with other studies showing that *OH* reaction rates are orders of magnitude faster as compared to O_2 [21,26,51]. The results showed that roughly 20-40% of soot mass was oxidized in the pre-flame region. In the reaction zone, due to the high reactivity of *OH*, the soot mass conversion was around 100% when *OH* concentration reached its maximum value. The NSC model was found to be insensitive to the variation of O_2 concentrations in the pre-flame zone where the temperature was low. The fact that NSC underestimated soot oxidation at lower temperatures (pre-flame zone) is consistent with previous studies [57,62–64]. As temperature increased, even though O_2 concentration was minimal, the oxidation rate due to NSC rose, suggesting a larger sensitivity to temperature as compared with O_2 concentration.

4.3.5 Sooting tendency

Sooting tendency (ST) was determined based on the definition given in our previous study for n-butanol mixtures [18]. ST was defined as the ratio of soot mass from a target fuel mixture to the soot mass from a fuel mixture that produced the maximum amount of soot between other cases. In this case, 30% methyl decanoate/ 70% n-dodecane at the higher velocity (C4) produced the maximum amount for this fuel and ST was defined as,

$$ST = \frac{m_i^{max}}{m_{C4}^{max}} \tag{4.5}$$

The results given in Figure 4.7 show that the highest ST was found for C4 flame

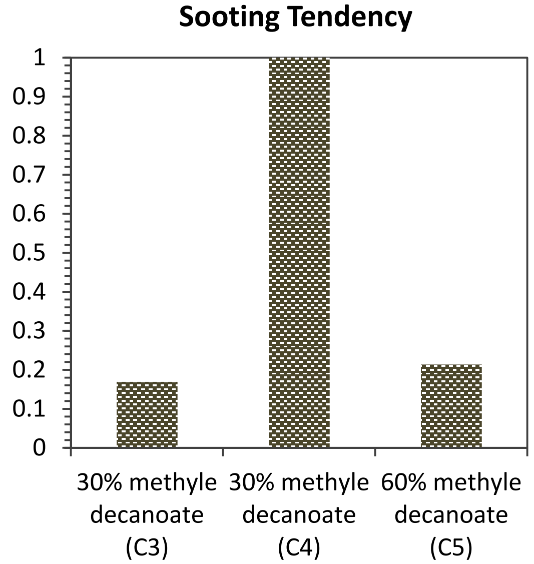

Figure 4.7. Sooting tendency for methyl decanoate/n-dodecane fuel mixtures

(among methyl decanoate mixtures) followed by C3 and C5. The comparison between C3 and C4 flames demonstrated that burning the same fuel under different flame conditions resulted in different ST. Increasing the cold gas velocity increased ST.

Also, the differences between ST for C4 and C5 flames (same flame conditions and different compositions) demonstrated that the fuel composition plays a key role in sooting behavior of the flame; increasing methyl decanoate concentration from 30% (C4) to 60% (C5) reduced the amount of soot, even though the C4 flame had a higher oxidation rate. These data are consistent with n-butanol mixture [16] where increasing n-butanol (10%, 30%, 60%) decreased sooting tendency.

4.4 Conclusion

The sooting behavior of biodiesel/diesel surrogate (methyl decanoate/n-dodecane) and alcohol/diesel surrogate (n-butanol/dodecane) was investigated by using a two-stage burner. PSDs, temperature, and main gas species were measured and reported. Kinetic modeling was used to obtain the *OH* profiles. The experimental oxidation rates were calculated and compared to Neoh and NSC model.

It was shown that increasing the cold gas velocity in methyl decanoate mixtures stabilized the flame. Soot formation was suppressed by increasing the amount of oxygenated fuel, either n-butanol or methyl decanoate. Increasing the methyl decanoate from 30% to 60% resulted in slightly higher peak temperature whereas it was opposite for n-butanol flames. However, the differences were insignificant. The analysis of gas species and kinetic model results showed similar oxidizer concentrations (O_2 and *OH*) for either n-butanol flames or methyl decanoate flames. However, soot oxidation rates were found to be different for each flame. This observation implied that not only soot oxidation rate depends on the *OH* and temperature, but also there is another important parameter which is related to the soot reactivity itself. The soot reactivity seemed to depend on the fuel source and the flame conditions in which soot has been derived. Since Neoh model determined the soot oxidation rates based on the temperature and *OH* concentration, different soot oxidative reactivities were captured by this model. The NSC model was found to be more sensitive to temperature as compared to O_2 concentration.

4.5 References

[1] A.K. Agarwal, Progress in Energy and Combustion Science 33 (2007) 233.

[2] S. Atsumi, T. Hanai, J.C. Liao, Nature 451 (2008) 86.

[3] E. Sukjit, J.M. Herreros, K.D. Dearn, R. García-Contreras, A. Tsolakis, Energy 42 (2012) 364.

[4] R. Lemaire, E. Therssen, P. Desgroux, Fuel 89 (2010) 3952.

[5] Y.L. Lin, H.P. Blaschek, Applied and Environmental Microbiology 45 (1983) 966.

[6] R. V Nair, G.N. Bennett, E.T. Papoutsakis, Journal of Bacteriology 176 (1994) 871.

[7] K. Yamane, Sae Paper 2004-01-1883 SP-1885 (2004) 43.

[8] J. Song, M. Alam, A.L. Boehman, U. Kim, Combustion and Flame 146 (2006) 589.

[9] A.L. Boehman, J. Song, M. Alam, Energy & Fuels 19 (2005) 1857.

[10] E.J. Barrientos, M. Lapuerta, A.L. Boehman, Combustion and Flame 160 (2013) 1484.

[11] P. Pepiot-Desjardins, R. Pitsch, H.; Malhotra, S.R. Kirby, A.L. Boehman, Combustion and Flame 154 (2008) 191.

[12] C.S. McEnally, L.D. Pfefferle, Environmental Science and Technology 45(6) (2011) 2498.

[13] R. Malhotra, A.L. Boehman, S.R. Kirby, H.G. Pitsch, P. Pepiot-Desjardins, in:, Abstracts of Papers, 234th ACS National Meeting, Boston, MA, United States, August 19-23, 2007, American Chemical Society, 2007, p. PETR–041.

[14] E. Barrientos, Impact of Oxygenated Fuels on Sooting Tendency and Soot Oxidative Reactivity with Application to Biofuels, 2013.

[15] M.K. Tran, D. Dunn-Rankin, T.K. Pham, Combustion and Flame 159 (2012) 2181.

[16] I.C. Jaramillo, C.K. Gaddam, R.L. Vander Wal, C.-H. Huang, J.D. Levinthal, J.S. Lighty, Combustion and Flame (2014).

[17] Y. Zhang, A.L. Boehman, Combustion and Flame 160 (2013) 112.

[18] H. Ghiassi, P. Toth, J.S. Lighty, Combustion and Flame 161 (2014) 671.

[19] H. (Ed) Bockhorn, Soot Formation in Combustion Mechanisms and Models, 1994.

[20] K.G. Neoh, J.B. Howard, A.F. Sarofim, Particulate Carbon Formation During Combustion, Plenum Press, New York, 1981.

[21] K.G. Neoh, J.B. Howard, A.F. Sarofim, in:, Twentieth Symposium (International) on Combustion, The Combustion Institute, Pittsburgh, 1985, pp. 951–957.

[22] S.J. Harris, M.M. Maricq, Chemical and Physical Processes in Combustion 33 (2002) 227.

[23] J. Nagle, R.F. Strickland-Constable, Proc. Conf. Carbon, 5th, Univ. Park, Penna., 1 (1961) 154.

[24] K.G. Neoh, Soot Burnout in Flames, Massachusetts Institute of Technology, 1981.

[25] C.A. Echavarria, I.C. Jaramillo, A.F. Sarofim, J.S. Lighty, Proceedings of the Combustion Institute 33 (2011) 659.

[26] Carlos A. Echavarria, I.C. Jaramillo, A.F. Sarofim, J.S. Lighty, C.A. Echavarria, Combustion and Flame 159 (2012) 2441.

[27] H. Ghiassi, P. Toth, J.S. Lighty, in:, ISBN: 978-1-62748-842-6 8th US National Combustion Meeting, 2013.

[28] C.J. Mueller, W.J. Cannella, T.J. Bruno, B. Bunting, H.D. Dettman, J.A. Ranz, M.L. Huber, M. Natarajan, W.J. Pitz, M.A. Ratcliff, K. Wright, Energy Fuels 26 (2012) 3284.

[29] O. Herbinet, W.J. Pitz, C.K. Westbrook, Combustion and Flame 157 (2010) 893.

[30] O. Herbinet, W.J. Pitz, C.K. Westbrook, Combustion and Flame 154 (2008) 507.

[31] K. Seshadri, T. Lu, O. Herbinet, S. Humer, U. Niemann, W.J. Pitz, R. Seiser, C.K. Law, Proceedings of the Combustion Institute 32 (2009) 1067.

[32] P.A. Glaude, O. Herbinet, S. Bax, J. Biet, V. Warth, F. Battin-Leclerc, Combustion and Flame 157 (2010) 2035.

[33] S.M. Sarathy, M.J. Thomson, W.J. Pitz, T. Lu, Proceedings of the Combustion Institute 33 (2011) 399.

[34] Y.L. Wang, Q. Feng, F.N. Egolfopoulos, T.T. Tsotsis, Combustion and Flame 158 (2011) 1507.

[35] W.J. Pitz, C.J. Mueller, Progress in Energy and Combustion Science 37 (2011) 330.

[36] B.D. Gould, X. Chen, J.W. Schwank, Journal of Catalysis 250 (2007) 209.

[37] D.C.S. McEnally, U.O. Koylu, L.D. Pfefferle, D.E. Rosner, Combustion and Flame 109 (1997) 701.

[38] B. Zhao, Z. Yang, J. Wang, M. V. Johnston, H. Wang, Aerosol Science and Technology 37 (2003) 611.

[39] B. Zhao, Z. Yang, M. V Johnston, H. Wang, A.S. Wexler, M. Balthasar, M. Kraft,

Combustion and Flame 133 (2003) 173.

[40] P. Minutolo, A. D’Anna, M. Commodo, R. Pagliara, G. Toniato, C. Accordino, Environmental Engineering Science 25 (2008) 1357.

[41] J. Song, V. Zello, A.L. Boehman, F.J. Waller, Energy & Fuels 18 (2004) 1282.

[42] C.K. Westbrook, W.J. Pitz, H.J. Curran, J. Phys. Chem. A 110 (2006) 6912.

[43] C.A. Taatjes, N. Hansen, A. McIlroy, J.A. Miller, J.P. Senosiain, S.J. Klippenstein, F. Qi, L. Sheng, Y. Zhang, T.A. Cool, J. Wang, P.R. Westmoreland, M.E. Law, T. Kasper, K. Kohse-Hoeinghaus, Science (Washington, DC, United States) 308 (2005) 1887.

[44] J.P. Szybist, A.L. Boehman, D.C. Haworth, H. Koga, Combustion and Flame 149 (2007) 112.

[45] B.A. Buchholz, C.J. Mueller, A. Upatnieks, G.C. Martin, W.J. Pitz, C.K. Westbrook, Society of Automotive Engineers, [Special Publication] SP SP-1890 (2004) 143.

[46] R.J. Kee, J.F. Grcar, M.D. Smooke, J.A. Miller, Fortran Program for Modeling Steady Laminar One-Dimensional Premixed Flames., Sandia Natl. Lab., 1985.

[47] G.P. Smith, D.M. Golden, M. Frenklach, N.W. Moriarty, B. Eiteneer, M. Goldenberg, C.T. Bowman, R.K. Hanson, S. Song, J. William C. Gardiner, V. V. Lissianski, Z. Qin, (2015).

[48] A.D. Abid, N. Heinz, E.D. Tolmachoff, D.J. Phares, C.S. Campbell, H. Wang, Combustion and Flame 154 (2008) 775.

[49] M.M. Maricq, N. Xu, Journal of Aerosol Science 35 (2004) 1251.

[50] P.A. Tesner, T.D. Smegiriova, V.G. Knorre, Combustion and Flame 17 (1971) 253.

[51] C.P. Fenimore, G.W. Jones, Journal of Physical Chemistry A 71 (1967) 593.

[52] K.B. Lee, M.W. Thring, J.M. Beér, Combustion and Flame 6 (1962) 137.

[53] D. Broome, I.M. Khan, Air Pollut. Control Transp. Engines, Symp. (1971) 185.

[54] S.W. Radcliffe, J.P. Appleton, Combustion Science and Technology 3 (1971) 255.

[55] K. Otto, M.H. Sieg, M. Zinbo, L. Bartosiewicz, in:, Diesel Combust. Emiss., [SAE Congr. Expo.], SAE, 1980, pp. 277–289.

[56] P. Gilot, F. Bonnefoy, F. Marcuccilli, G. Prado, Combustion and Flame 95 (1993) 87.

[57] J. Song, C. Song, G. Lv, L. Wang, F. Bin, Combustion Theory and Modelling 16 (2012) 639.

[58] L.R. Radovic, P.L. Walker, R.G. Jenkins, Fuel 62 (1983) 849.

[59] D.M. Smith, A.R.R. Chughtai, M. Smith, Colloids and Surfaces, A: Physicochemical and Engineering Aspects 105 (1995) 47.

[60] H.J. Seong, A.L. Boehman, Combustion and Flame 159 (2012) 1864.

[61] C. Esarte, M. Abián, Á. Millera, R. Bilbao, M.U. Alzueta, Energy 43 (2012) 37.

[62] P. Cadman, R. Cornish, R.J. Denning, AIP Conference Proceedings 208 (1990) 751.

[63] J. Camacho, Y. Tao, H. Wang, Proceedings of the Combustion Institute (n.d.).

[64] R.L. Vander Wal, A.J. Tomasek, Combustion and Flame 134 (2003) 1.

[65] M.S. Graboski, R.L. Mccormick, Progress in Energy and Combustion Science 24 (1998) 125.

[66] R.L. Vander Wal, A.J. Tomasek, Combust. Flame 136 (2004) 129.

[67] I.C. Jaramillo, C.K. Gaddam, R.L. Vander Wal, J.S. Lighty, Combustion and Flame 162 (2015) 1848.

CHAPTER 5

SOOT OXIDATION-INDUCED FRAGMENTATION: PART 1: THE RELATIONSHIP BETWEEN SOOT NANOSTRUCTURE AND OXIDATION-INDUCED FRAGMENTATION

5.1 Introduction

The term "soot nanostructure" has been used broadly to refer to the physical properties such as dimensions and relative orientations of the graphene-like segments in soot particles [1]. High-Resolution Transmission Electron Microscopy (HR-TEM) is a suitable approach to characterize the nanostructure of soot samples [1–6]. It has been shown that initial fuel type and synthesis conditions of temperature and time affect the soot nanostructure [7]. Several studies have been performed to explore the effect of nanostructure on the soot oxidation rate [2,8,9]. A considerable number of them have been devoted to systems where oxygen is the oxidizer [15,25, 30].Vander Wal and Tomasek [8] studied the differences in nanostructure and reactivity for soot samples generated from benzene, ethanol, and acetylene. Their results showed that soot from benzene with amorphous structure and from ethanol with curvy plane layers was more reactive than the sample from acetylene with a graphitic-like structure. In another study, Vander Wal and Muller [16] confirmed that the soot nanostructure comprised of either curvy or disordered structures showed a higher reactivity toward oxidation. Su et al. [14] used HR-TEM and TGA to correlate the nanostructure with oxidation reactivity of different soot samples from exhaust of heavy duty (HD) diesel engines. Yehliu et al. [9] suggested that oxidative reactivity is primarily dominated by the disordered carbonaceous structure. Jaramillo et al. [1] determined the kinetic parameters for soot oxidation by using TGA for several pure component hydrocarbon fuels and surrogates. They also investigated the role of nanostructure in the oxidation of the soot samples. Their result demonstrated that the activation energy is proportional to the fringe length and inversely proportional to the fringe tortuosity.

In a flame study, where OH was the main oxidizer, Ghiassi et al. [10] investigated the role of nanostructure on the soot surface reactivity. The fringe orientation maps were quantified in terms of polar (a representative of curvy structure) and nematic (a representative of flat structure) symmetry, as illustrated in Figure 5.1. The oxidative reactivity was shown to be correlated with the degree of orderliness of layer planes. The most reactive soot had an amorphous nanostructure which was composed of short individual layer planes with no orientation relative to each other. For this type of nanostructure, the higher ratio of carbon in the edge sites versus basal plane sites implied a higher oxidative reactivity. With the same layer plane size, higher relative curvatures were more reactive. Indeed, the curvature weakens the C-C bond and makes it more susceptible to oxidative attack by imposing bond strain and reducing electronic resonance stabilization in the orbital overlap [9, 12].

Soot fragmentation has been hypothesized with two sub-mechanisms [12]: (i) O_2 penetrating the primary soot particles, which in turn causes internal burning and loss of

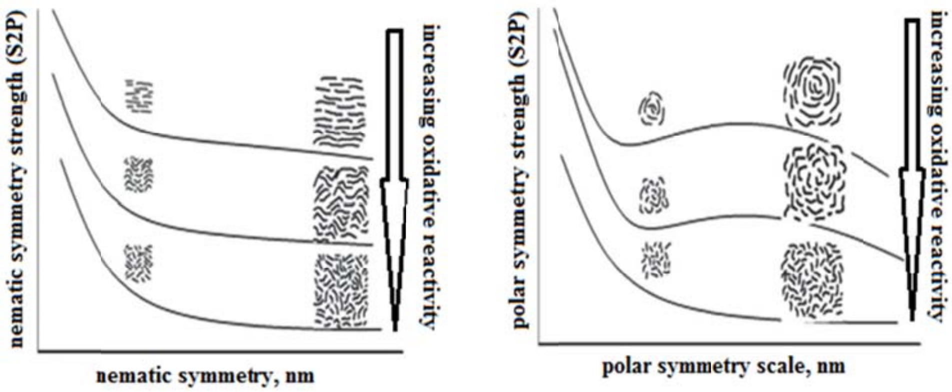

Figure 5.1. Histogram of symmetry strength versus symmetry scale for nematic symmetry (left) and polar symmetry (right) which was in correlation with soot oxidative reactivity (adapted from Figure 3.10, Chapter 3).

connectivity between the carbonaceous phases results in breaking up of primary particles (ii) the breakup of bridges (or necks) between primary particles in the aggregate structure and the removal of small fragments from the edges of the primary particles surface. In this study, these two mechanisms are examined. To explore the reactivity of the bridge sites between two particles, the nanostructure was quantified by image analysis and compared to the nanostructure of bulk materials. In addition, the possibility of internal burning of primary particles was tested by comparing the diffusion time scale to reaction time scale through the effectiveness factor analysis. The parameters needed to calculate the effectiveness factor including the actual oxygen diffusion pathway and pore width were estimated by the image analysis technique.

5.2 Experimental setup

In order to investigate the morphology and nanostructure of the different soot samples, HR-TEM was performed. The soot sample was deposited on a lacey C/Cu TEM grid following the procedure of thermophoretic sampling by Dobbins [13]. TEM grids were rapidly inserted in the flow of combustion gases and soot was deposited due to the thermophoretic gradient. Multiple insertions were used to get a proper representative sample on the grid. A TEM grid holder attached to a piston and compressed air at 60 psig was used to quickly insert the TEM grid into the flame to minimize the impact of flame temperature on the particles that experienced multiple insertions [14]. The temperature of the carrier probe during the sampling was measured by attaching a thermocouple (type B) on the top of the TEM holder. The carrier probe reached a local maximum temperature as high as 450±10 K while at the same HAB, the flame temperature was around 1500 K. This confirmed the minor temperature effect on the soot samples on the grid. In addition, the control system was designed to move the probe with the maximum speed to a precisely defined position in the flame. Figure 5.2 shows the schematic diagram of the probe control system. The soot grid samples were taken from the second burner at initial heights where soot did not undergo any oxidation reactions. The precise spatial positioning of the probe within the flame was achieved by mounting the mechanical components on a translation stage. The accuracy of probe positioning was estimated to be better than 0.1 mm. TEM images were taken using a FEI Tecnai F20 Ultratwin TEM/STEM operating at 200 keV. TEM images were processed by an image analysis framework designed for quantifying the soot nanostructure [15–17]. The framework is based on filtering theory in order to extract the symmetry parameters.

Nematic and polar order parameters (S_{2N} and S_{2P}, respectively) introduced by Shim et al. [18] were extracted by the orientation-filtering technique developed by Toth et al. [16]. Polar symmetry quantifies the dominance of fringes oriented concentrically around a symmetry pole in the overall structure. The nematic symmetry strength parameter

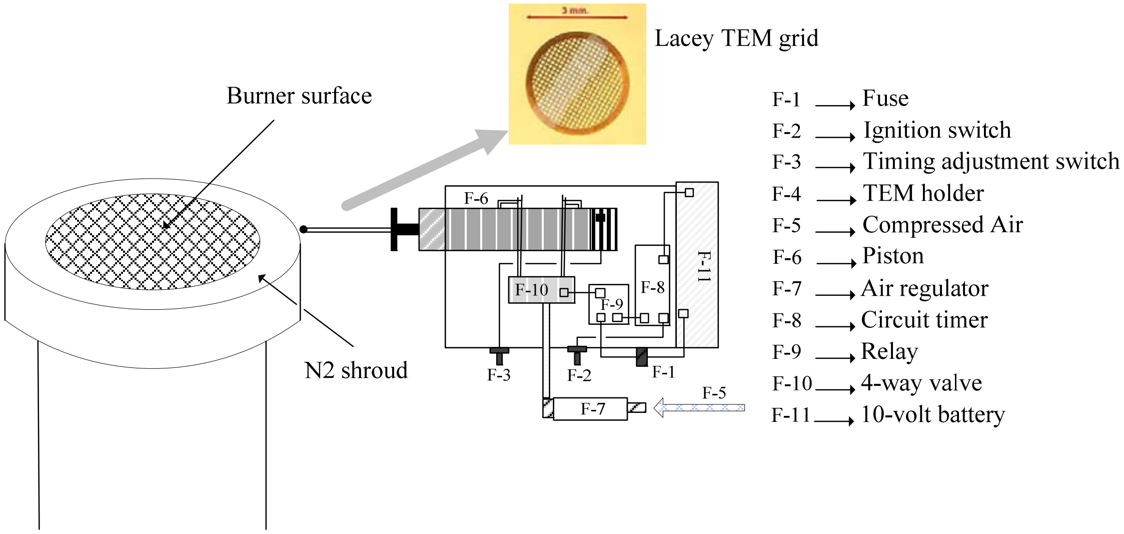

Figure 5.2. Schematic diagram of the probe control system.

quantifies the prevalence of flat graphene layers (graphite-like microcrystals) in the structure. In general, high values of both symmetry parameters imply graphite-like nanostructure. With the method utilized here, it is possible to describe the symmetry of the structure over multiple spatial scales. The bridge sites in the aggregate structure were identified manually, based on which image masks were defined, locating pixels that belonged to bridge sites. The symmetry parameters computed over the masked areas were compared to those computed over the rest (“bulk”) of the imaged structures.

During the assessment of the possibility of internal burning, the knowledge of actual distance travelled by O_2 molecules toward the center of a particle before reacting with an active site is needed. The image analysis procedure similar to that described by Toth et al. [17] was utilized to estimate this. In brief, sub-structures with high nematic symmetry strength were detected by setting a threshold on S_{2N} and constructing binary images that contained true values at the detected patches of high nematic symmetry. The remaining (unmasked) areas represented amorphous material, characterized by low S_{2N} values. It was postulated that O_2 molecules only diffuse through the amorphous phase, as the porous structure imposes much less diffusion resistance as compared to the fairly crystalline sub-structures. Several studies [19–21] suggested that the regions that appear as amorphous in HR-TEM images actually contain pores of different sizes and shapes. Some studies [19,20] proposed ways to determine the size distribution of the suggested pores. In a recent publication, Pré et al. [21] introduced image-analysis based on the measurements of "effective spaces" in pyrolytic carbons. The mean distances travelled by the oxidizer particles were computed by running a Monte-Carlo ensemble of random walk simulations. In random walk, the oxidizer particles were free to travel inside the amorphous phase. The distance travelled inside the amorphous phase was represented by a collection of possible paths along the medial axes of the binary image representing the detected nanopores in the structure (in other words, it was assumed that the molecule travels along the paths of least resistance with no wall collisions) [22]. A set of 100,000 random walk trials were computed for each analyzed image. The simulations were stopped whenever the virtual oxidizer particle "hit" the manually detected inner cores.

There are some limitations in this topological analysis. First, the two-dimensional nature of the analysis implies that the tortuosity values estimated by image processing might be different than values obtained by allowing an additional degree of freedom. However, by assuming that the structures are isotropic, being an implicit measure, the two-dimensional tortuosity ratio approximates its three-dimensional counterpart [23]. Second, no forces or other physical interactions were modeled—tortuosity was treated as a purely topological property. Third, the threshold set for S_{2N} was highly uncertain. Previous studies defined the typical value of 0.7-0.9 as a guideline [24], thus the values used here were varied between 0.8±0.1 and the effect of the variation was included in the final uncertainty of tortuosity. Overall, the resulting tortuosity values are purely topological measures, with no information content whatsoever representing physical or chemical interaction between the oxidizer molecules and the structure—they are, however, fairly robust, although rough estimates of the tortuosity of the studied soot nanostructures. In interpreting the data, the error bars were provided in order to not mislead the reader by suggesting that the reported values are results of rigorous physical measurements.

5.3 Results and discussion

5.3.1 Aggregate break-up

Soot aggregation starts at the nucleation step where freshly formed ultrafine particles (spherules) are nucleated out of the gas-phase [25,26]. These freshly nucleated particles are in point contact immediately after collision. The region between two newly joined particles is a preferred site for surface deposition, resulting in more rapid buildup between them [27,28]. If the rate of nucleation is intense, even the maximum rate of surface deposition is not enough to completely wrap the spherules in a form of single particle [25]. This leads to a partial buildup between two particles resulting in a considerable number of spherules being connected with narrow bridges which form fractal-like structures [26]. In later stages, collisions increase the size of the aggregate and the colliding entities maintain their own structures.

In this study, the nanostructure of the bridge site, as a representative of interparticle deposits, was analyzed versus the bulk material to identify if this region's nanostructure suggests a faster oxidation rate, leading to the fragmentation. Morphological studies were performed on TEM images to reveal differences in ordered and disordered nanostructure; this was shown through the nematic (flat) and polar (curvy) symmetry. Symmetry analysis of 15 particle bridge sites was performed using custom algorithms to extract nanostructure. The analysis required a defined outline where the bridge sites were carefully traced and the traced outline was used (Figure 5.3b). A HR-TEM image is given

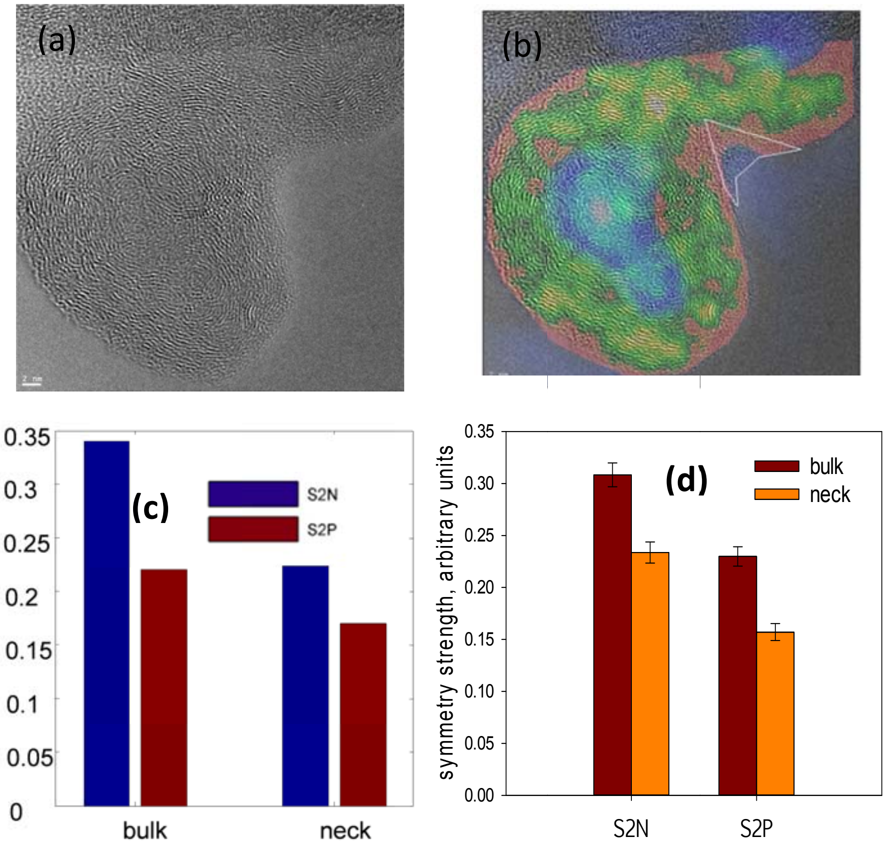

Figure 5.3. HRTEM image of a soot sample derived from the base case (a) with symmetry saliency maps on the right (b). The colors given in (b) represent crystalline regions (green), particle cores (blue), and completely amorphous zones (red). The corresponding symmetry analysis of the given image is presented in the graph (c), indicating that the neck (bridge) is arranged less orderly for both flat (S_{2N}) and curvy (S_{2P}) structure. The bar graph shows the average values for polar (S_{2P}) and nematic (S_{2N}) symmetry is lower for the bridge site than the bulk material. The graph (d) is the average of symmetry analysis of 15 bridge sites.

in Figure 5.3a as a raw image and Figure 5.3b shows the traced neck and corresponding symmetry saliency map. A lower degree of orderliness regarding both nematic (flat) and polar (curvy) symmetry was determined for the given example in Figure 5.3c. The same procedure was repeated for other images and the average is presented in the Figure 5.3d, demonstrating that the bridge site has a less-ordered nanostructure in terms of polar and nematic symmetry as compared to the particle sites.

Our previous studies [10] showed that less-ordered nanostructure, i.e., smaller planes or planes with higher curvature, were more reactive, as illustrated in Figure 5.1. The deposition of small planes or polycyclic aromatic hydrocarbons (PAHs) which contain σ-bonds hinders π-electrons of other similar molecules to reach an interaction distance. This conformation is responsible for lower binding energies which results in disordered nanostructure [29]. A higher number of edge sites versus basal plane carbon atoms in small PAHs results in a higher reactivity. In addition, the relative curvature of planes also impacts the oxidation rate. Curvature is the result of 5-membered rings in the aromatic framework [30]. This curvature imposes bond strain as the orbitals overlap, and decreases the electronic resonance stabilization [36]. The C-C bonds are weakened and individual atoms are more susceptible to oxidative attack [36, 37]. Based on the discussion above and the results in Figure 5.3d, a faster oxidation rate can be expected for the bridge sites. The higher reactivity of the interparticle deposits has been also indirectly reported by literature. The previous study by Echavaria et al. [12] also showed that bridges decreased faster with increasing extent of oxidation. They measured the size of bridges before and after oxidation and they found a significant reduction in size of bridges.

5.3.2 Primary particle break-up

The fragmentation of a single particle due to internal burning by oxygen diffusion has also been suggested as one of the mechanisms for soot fragmentation [12,31]. The possibility of internal burning by OH radicals has been shown to be less than O_2 molecules [31]. OH radicals are more reactive than O_2 molecules and this extreme reactivity makes their reaction time scale much smaller than the diffusion time scale. It is likely that OH radicals would react before getting the chance to diffuse. The mechanism of oxidation by O_2 has been usually assumed by Langmuir-Hinshelwood (LH) or related mechanisms [32,33]. Under LH mechanism, oxidation proceeds via reaction with the migrating oxygen molecules that are first adsorbed on nonreactive sites [32,33]. Adsorption of molecular oxygen onto the basal plane forms a physisorbed precursor state and oxygen molecules then diffuse to defect sites such as vacancies or edge planes [34]. If O_2 diffusion occurs within the pores of particles, then there would be a possibility of internal burning; furthermore, internal burning results in an increase in surface area as combustion proceeds [35]. Studies have shown that noncarbonized soot samples have a strong tendency to burn from the inside out at a lower temperature range 450-800 °C in the presence of O_2 [36,37]. Gilot et al. [38] and Marcucilli et al. [39] showed that the increase in the surface area during oxidation by O_2 was greater at 600 °C than at 800 °C. This observation is consistent with significant oxygen penetration at low temperature due to slower consumption by reaction [35]. However, the possibility of internal burning of the primary soot particles has not been adequately addressed at flame temperatures.

Neoh et al. [40] studied the possibility of internal burning by O_2 molecules and OH radicals by using effectiveness factor analysis. They calculated the effectiveness factors for pores of radius 0.5 and 4 nm, the former radius to represent the pores inside a particle, and the latter to represent the spacing between particles. They showed that O_2 diffuses into the particles to a greater extent than *OH*, primarily due to the higher reaction rate of *OH*. They concluded that it was unlikely to have internal burning by OH, since they did not observe fragmentation for a rich flame, where *OH* is the main oxidant. Whereas Neoh et al. [40] based their calculations by assuming pore radius and particle tortuosity values, our calculations are based on pore radius and particle tortuosity determined by image analysis.

Internal burning, and potential fragmentation due to this burning, will depend upon the rate of diffusion versus reaction at the temperatures of interest. The time scale t_D for O_2 diffusion is

$$t_D = \frac{R^2}{D_e} \tag{5.1}$$

where D_e is the effective intraphase diffusion coefficient, R is the radius of soot particle, The time scale for O_2 reaction (t_r) on the surface or inside a soot particle is,

$$t_r = \frac{1}{k} \tag{5.2}$$

where $k\left(\frac{1}{s}\right)$ is the rate constant.

In order to compare these two characteristic times, the ratio of t_D/t_r is given as follows,

$$M_T^2 = \frac{t_D}{t_r} = R^2 \frac{k}{D_e} \tag{5.3}$$

This number is known as Thiele's module, showing a comparison between the time needed for O_2 diffusion and the time required for O_2 reaction. In other words, it is regarded as a measure for the ratio of the reaction rate to the rate of diffusion.

Determining the Thiele modulus alone does not demonstrate how much the reaction rate is lowered because of the diffusion limit. The effectiveness factor is the parameter defined as follows indicating the relative importance of diffusion and reaction limitations.

$$\eta = \frac{Actual\ overall\ rate\ of\ reaction}{\begin{array}{c}Rate\ of\ reaction\ if\ entire\ surface\ exposed\ to\ the\\ external\ particle\ surface\ condition, C_s\end{array}} \tag{5.4}$$

The use of this dimensionless number is well-established in the literature for describing transport-reaction kinetics in porous catalysts. This concept was first developed mathematically by Thiele [41] and has since been extended by many other researchers. Extensive investigation of analytical solutions and methods for the approximation of the effectiveness factor can be found in Aris [42,43]. The effectiveness factor in terms of M_T is,

$$\eta = \frac{3}{M_T}\left(\frac{1}{\tanh M_T} - \frac{1}{M_T}\right) \tag{5.5}$$

This expression determines the effectiveness factor for spherical particles based on the assumption of first order reaction. For the value of $\eta \cong 1$, the concentration of O_2 is uniform within a particle, whereas for $\eta \cong 0$, the concentration of O_2 drops rapidly (due to a diffusion limit or a fast reaction rate) and there are large concentration gradients of O_2 within a particle. The Thiele modulus takes into account the important factors within a porous particle, namely: (i) diffusion of the reacting components; (ii) micro properties of the particle, the most important being pore size distribution and pore tortuosity; and, (iii) reaction kinetics [44]. These parameters are discussed in the following paragraphs.

Due to the complexity of diffusion of the reactants in a solid matrix, the diffusion is usually determined by an effective diffusion coefficient, D_e. In order to calculate D_e, since soot pore width is on the order of or less than the mean free path, Knudsen diffusion dictates intraphase transport [45,46]. The expression for the effective diffusivity D_e as a function of pore width r_p and tortuosity τ is given as [44, 45]

$$D_e = \frac{4}{3} \frac{S_{BET}\ \rho}{\tau} \left(\frac{R_g T}{2\pi M}\right)^{1/2} r_p^2 \tag{5.6}$$

Neoh et al. [31] used the NSC expression [49] to calculate the rate constant which is needed in the calculation of the Thiele modulus and effectiveness factor. However, use of NSC to estimate the soot oxidation rate is subject to some uncertainty. A number of studies [8,50–52] have compared experimental soot oxidation rates with the NSC expression and reported a higher rates than those given by NSC values. Cadman et al. [50] studied the soot oxidation rates by oxygen-argon mixtures in a shock tube at the temperature range (1500-3500 K). They reported a factor of six higher soot oxidation rates compared with NSC rate. Song et al. [51] measured the oxidation rate of diesel soot by oxidative thermogravimetry and Raman scattering spectrometry. Their result showed the oxidation rates differed by nearly fourfold from that calculated by NSC model. Vander Wal and Tomasek [8] examined soot burnout rates by directly injecting newly formed particles from a pyrolysis flow reaction into the post-flame region of a lean flame. Similar to the aforementioned studies, the burnout rates reported were shown to be more than an order of magnitude faster than NSC. More recently, Camacho et al. [52] determined the kinetics of nascent soot oxidation by molecular oxygen in a flow reactor at temperatures of 950, 1000, 1050 K. The measured rates from particles generated in a premixed flame of ethylene, n-heptane, and toluene were found to be an order of magnitude larger than that predicted by the NSC correlation. Given this, we determined the rate based on the NSC, and multiplied by a factor of 10 in order to calculate k', the rate was approximated as first order, i.e.,

$$k' = W/(12C_{O2}) \tag{5.7}$$

Using two O_2 partial pressures and temperatures, 0.01 and 0.1 atm and 1500 and 1600K, the values of k' were determined, and $k\,(\frac{1}{s})$ was calculated by $k'\left(\frac{cm^3}{cm^2.s}\right) \times S_{BET}(\frac{cm^2}{gr}) \times \rho(\frac{gr}{cm^3})$ with values shown in Table 5.1.

Two important parameters that affect the diffusion time scale are tortuosity and pore width. Tortuosity is an important term defined here for soot particles to account for the deviations in the path length of the pores.

$$\tau = \frac{Actual\ distance\ O_2\ travels\ from\ particle\ periphery\ to\ the\ core}{Shortest\ distance\ from\ particle\ periphery\ to\ the\ core} \quad (5.8)$$

$$= \frac{L}{R}$$

Obviously, τ must be greater or equal to one. A rough estimation on the possible pathway of O_2 toward the center of a particle was determined with the aid of image analysis technique. It was assumed that if an oxygen molecule is able to penetrate the particle, it will do so through the pockets, or pores located on the surface [54].

A penetrated molecule will then continue its pathway through the slit shape cavities between two crystallites [55] until reaching the core of the particle. The image analysis results are shown in Figure 5.4a with two examples of soot crystallites (orange color) and the hypothetical pathway of O_2 (green lines).

The corresponding effective pore width (the measure of space between two crystallites) was performed by using distance transform techniques. Figures 5.4b and 5.4c give the average τ and r_p distributions calculated for 9 images. The result shows that average tortuosity value was 5.33±0.09 and, the average value for extracted effective spaces or pore width was 1.6±0.11 nm. The corresponding value of porosity determined by the given pore width, and other properties in Table 5.1, is 0.41±0.03, in fair agreement with values assumed by [1,56]. This result contradicts literature reports that soot particles are nonporous [57,58] or have only limited porosity [59].

Figure 5.5 shows posterior probabilities of η depicted for different particle sizes for the two temperatures and oxygen partial pressures. Intuitively, there is a possibility of O_2 diffusion occurring within a range of pore sizes (r_p ~0.2-5 nm) with different diffusion pathways (τ~1-20). This effect makes the calculation more complex. Unlike Neoh's

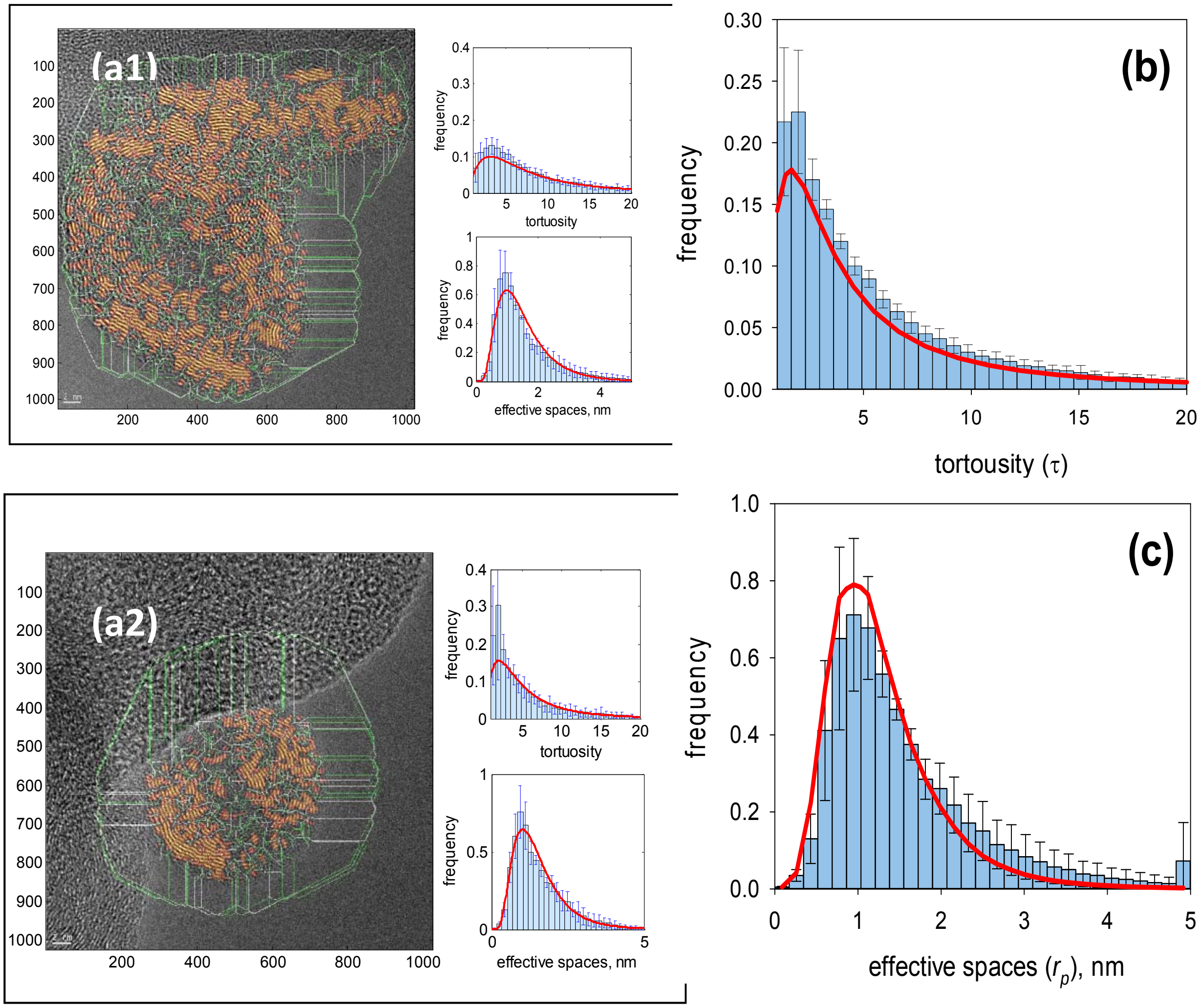

Figure 5.4. Demonstration of crystallite segmentation and the hypothetical pathway of O_2 with the corresponding tortuosity (τ) and effective pore spaces (r_p) estimated based on 2D random walk (a1, a2). The average τ histogram (b) and the average r_p histogram (c) are given for nine images. The red line shows the best fit lognormal probability density functions.

Table 5.1. Parameters used to estimate the effectiveness factors.

Parameter	Value	Source
BET surface, S_{BET}	196 $(\frac{m^2}{gr})$	[12]
Soot density, ρ	1.5 $(\frac{gr}{cm^3})$	[53]

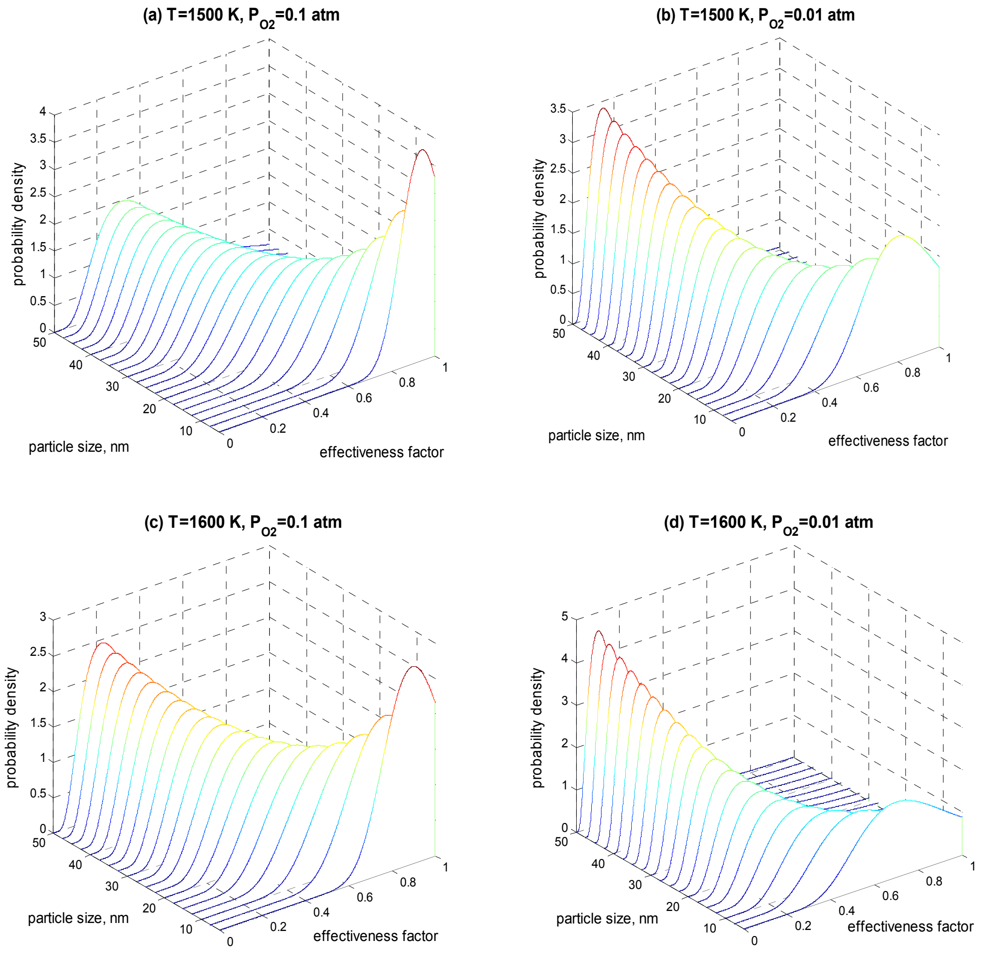

Figure 5.5. Posterior probability of the effectiveness factor for different particle sizes. Note, probability density scales are different.

calculation where a single diffusion pathway (τ=2) and a constant pore width were assumed, this effect was taken into account based on the Monte-Carlo uncertainty propagation, with a priori determined lognormal distributions of τ and r_p as inputs. Figures 5.5a and 5b show η for the temperature 1500 K and oxygen partial pressures 0.1 and 0.01 atm. Figure 5.5c and 5d show the results for similar oxygen partial pressures but at a higher temperature (1600 K). For both temperatures, the probability density distributions moved toward the larger effectiveness values by increasing the oxygen partial pressure. This result illustrated that the higher oxygen concentration suggests greater oxygen availability within the particle. On the other hand, with the same oxygen concentration, reducing the temperature increased the possibility of internal burning, likely due to the decreased reaction rate.

In all figures, increasing the size of particles changed the probability distributions toward smaller values of the effectiveness factor, indicating larger oxygen concentration gradients within these particles. These results suggest that smaller particles have a possibility of internal burning as compared to larger ones.

Using the obtained values stated for average pore width and tortuosity, and kinetic rate for a temperature of 1500 K, Figure 5.6 shows the relative reaction time versus diffusion time as a function of particle size. For all particles, especially those less than 10 nm, O_2 diffusion/reaction time is much larger than OH values. The higher OH reaction rate will dictate that OH will likely react before diffusion in a greater extent than O_2 molecules.

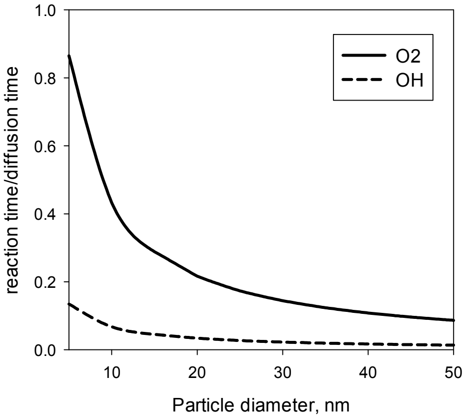

Figure 5.6. Reaction time versus diffusion time for O_2 and OH at T=1500 K. The O_2 reaction rate was calculated by NSC and OH reaction rate was based on the Neoh's expression. The diffusion time was calculated based on the procedure given in the manuscript.

5.4 Conclusion

The work reported here examined two mechanisms of soot fragmentation hypothesized by Neoh et al. [40] and further discussed by [12]. One hypothesis is that fragmentation occurs due to burning bridges between aggregates selectively, breaking the aggregates apart; the second is that oxygen diffuses within the particle and causes internal burning which, in turn, increases porosity such that the particle eventually breaks apart. Since the nanostructure provides information on the oxidative reactivity of soot, the oxidative reactivity of bridge sites was compared to the actual particles through the image analysis technique. TEM images were processed by an image analysis framework designed for extracting the symmetry parameters (nematic and polar order parameters) to quantify the soot nanostructure. The lower values of both symmetry parameters showed a higher reactivity of the bridge sites, resulting in a faster burning rate, suggesting aggregate fragmentation by this mechanism.

In addition, the mechanism of primary particle break-up was tested by assessing the feasibility of internal burning in soot because of O_2 diffusion within the particles. In order to estimate the particle tortuosity, the actual distance travelled by O_2 molecules toward the center of a particle before reacting with an active site was computed by running a Monte-Carlo ensemble of random walk simulations. A log-normal distribution was reported with the average value 5.33±0.09. The effective pore width was estimated by assuming the penetrated molecule continues its pathway through the slit shape cavities between two crystallites until reaching the core of the particle and the average was determined to be 1.6±0.11 nm. To compare the diffusion time with reaction time, the effectiveness factor was calculated for two temperatures and oxygen concentrations, with a priori determined lognormal distributions of particle tortuosity and pore width as inputs. The results showed the internal burning of particles would be possible for small particles up to 10 nm. However, in larger particles, the effectiveness factor decreases, suggesting less O_2 would be available within the particle. The effectiveness factor decreased with increased temperature, also indicating less internal burning.

5.5 References

[1] I.C. Jaramillo, C.K. Gaddam, R.L. Vander Wal, C.-H. Huang, J.D. Levinthal, J.S. Lighty, Combustion and Flame (2014).

[2] K. Yehliua, R.L. Vander Wal, O. Armas, A.L. Boehman, Combustion and Flame 159 (2012) 3597.

[3] C.K. Gaddam, R.L. Vander Wal, Combustion and Flame 160 (2013) 2517.

[4] R.L. Vander Wal, A. Yezerets, N.W. Currier, D.H. Kim, C.M. Wang, Carbon 45 (2007) 70.

[5] Z. Li, C. Song, J. Song, G. Lv, S. Dong, Z. Zhao, Combustion and Flame 158 (2011) 1624.

[6] C.-H. Huang, R.L. Vander Wal, Energy & Fuels 27 (2013) 4946.

[7] R.L. Vander Wal, A.J. Tomasek, Combust. Flame 136 (2004) 129.

[8] R.L. Vander Wal, A.J. Tomasek, Combustion and Flame 134 (2003) 1.

[9] K. Al-Qurashi, A.L. Boehman, Combust. Flame 155 (2008) 675.

[10] H. Ghiassi, P. Toth, J.S. Lighty, Combustion and Flame 161 (2014) 671.

[11] W. Rybak, P. Chambrion, J. Lahaye, Carbon 33 (1995) 259.

[12] Carlos A. Echavarria, I.C. Jaramillo, A.F. Sarofim, J.S. Lighty, C.A. Echavarria, Combustion and Flame 159 (2012) 2441.

[13] R.A. Dobbins, C.M. Megaridis, Langmuir 3 (1987) 254.

[14] C.A. Echavarria, Evolution of Soot Size Distribution during Soot Formation and

Soot Oxidation-Fragmentation in Premixed Flames: Experimental and Modeling Study, University of Utah, 2010.

[15] P. Toth, A.B. Palotas, E.G. Eddings, R.T. Whitaker, J.S. Lighty, Combustion and Flame 160 (2013) 909.

[16] P. Toth, A.B. Palotas, E.G. Eddings, R.T. Whitaker, J.S. Lighty, Combustion and Flame 160 (2013) 909.

[17] P. Toth, Á.B. Palotás, J. Lighty, C.A. Echavarria, Fuel 99 (2012) 1.

[18] H.S. Shim, R.H. Hurt, N.Y.C. Yang, Carbon 38 (2000) 29.

[19] Z.-H. Huang, F. Kang, W.L. Huang, J.-B. Yang, K.-M. Liang, M.-L. Cui, Z. Cheng, Journal of Colloid and Interface Science 249 (2002) 453.

[20] K. Oshida, T. Nakazawa, T. Miyazaki, M. Endo, Synthetic Metals 125 (2001) 223.

[21] P. Pre, G. Huchet, D. Jeulin, J.-N. Rouzaud, M. Sennour, A. Thorel, Carbon 52 (2013) 239.

[22] L. Lam, S.-W. Lee, C.Y. Suen, IEEE Transactions on Pattern Analysis and Machine Intelligence 14 (1992) 879.

[23] S.A. Saltykov, Stereometric Metallography. 3rd Ed., Metallurgiya, 1970.

[24] R.H. Hurt, G.P. Crawford, H.-S. Shim, Proceedings of the Combustion Institute 28 (2000) 2539.

[25] P. Mitchell, M. Frenklach, Symposium (International) on Combustion 27 (1998) 1507.

[26] P. Mitchell, M. Frenklach, Physical Review E: Statistical, Nonlinear, and Soft Matter Physics 67 (2003) 061407/1.

[27] N.M. Morgan, R.I.A. Patterson, M. Kraft, Combustion and Flame 152 (2008) 272.

[28] R.I.A. Patterson, M. Kraft, Combustion and Flame 151 (2007) 160.

[29] A. D’Anna, M. Sirignano, J.H. Kent, in:, Seventh Mediterranean Combustion Symposium, 2011.

[30] H.W. Kroto, J.R. Heath, S.C. O’Brien, R.F. Curl, R.E. Smalley, Nature (London, United Kingdom) 318 (1985) 162.

[31] K.G. Neoh, Soot Burnout in Flames, Massachusetts Institute of Technology, 1980.

[32] R.T. Yang, C. Wong, The Journal of Chemical Physics 75 (1981).

[33] R.T. Yang, C. Wong, Science (Washington, DC, United States) 214 (1981) 437.

[34] R. Schloegl, G. Loose, M. Wesemann, Solid State Ionics 43 (1990) 183.

[35] B.R. Stanmore, J.F. Brilhac, P. Gilot, Carbon 39 (2001) 2247.

[36] F.A. Heckman, D.F. Harling, Rubber Chem. Technol. 37 (1964) 1245.

[37] R.H. Hurt, A.F. Sarofim, J.P. Longwell, Combustion and Flame 95 (1993) 430.

[38] P. Gilot, F. Bonnefoy, F. Marcuccilli, G. Prado, Combustion and Flame 95 (1993) 87.

[39] F. Marcuccilli, P. Gilot, B. Stanmore, G. Prado, Symposium (International) on Combustion, [Proceedings] 25 (1994) 619.

[40] K.G. Neoh, J.B. Howard, A.F. Sarofim, in:, Twentieth Symposium (International) on Combustion, The Combustion Institute, Pittsburgh, 1985, pp. 951–957.

[41] E.W. Thiele, Industrial and Engineering Chemistry 31 (1939) 916.

[42] R. Aris, Mathematical Theory of Diffusion and Reaction in Permeable Catalysts, Vol. 1: The Theory of the Steady State., Oxford Univ. Press, 1975.

[43] R. Aris, The Mathematical Theory of Diffusion and Reaction in Permeable Catalysts, Vol. 2: Questions of Uniqueness, Stability, and Transient Behavior., Oxford Univ. Press, 1975.

[44] R.J. Wijngaarden, A. Kronberg, K.R. Westerterp, Industrial Catalysis: Optimizing Catalysts and Processes., Wiley-VCH, 1998.

[45] S. Salvador, J.-M. Commandré, B.R. Stanmore, Fuel 82 (2003) 715.

[46] J.F. Brilhac, F. Bensouda, P. Gilot, A. Brillard, B. Stanmore, Carbon 38 (2000) 1011.

[47] R.E. Cunningham, R.J.J. Williams, Diffusion in Gases and Porous Media., Plenum Press, 1980.

[48] W. Kast, C.-R. Hohenthanner, International Journal of Heat and Mass Transfer 43 (1999) 807.

[49] J. Nagle, R.F. Strickland-Constable, Proc. Conf. Carbon, 5th, Univ. Park, Penna., 1 (1961) 154.

[50] P. Cadman, R. Cornish, R.J. Denning, AIP Conference Proceedings 208 (1990) 751.

[51] J. Song, C. Song, G. Lv, L. Wang, F. Bin, Combustion Theory and Modelling 16 (2012) 639.

[52] J. Camacho, Y. Tao, H. Wang, Proceedings of the Combustion Institute (n.d.).

[53] M.M. Maricq, N. Xu, Journal of Aerosol Science 35 (2004) 1251.

[54] D. Chen, J. Akroyd, S. Mosbach, M. Kraft, Proceedings of the Combustion Institute (n.d.).

[55] A. Schröder, M. Klüppel, R.H. Schuster, J. Heidberg, KGK. Kautschuk, Gummi, Kunststoffe 54 (n.d.) 260.

[56] J. Song, C.-H. Jeon, A.L. Boehman, Energy & Fuels 24 (2010) 2418.

[57] M.S. Akhter, A.R. Chughtai, D.M. Smith, Applied Spectroscopy 39 (1985) 143.

[58] M.S. Akhter, A.R. Chughtai, D.M. Smith, Applied Spectroscopy 39 (1985) 154.

[59] O. Gustafsson, F. Haghseta, C. Chan, J. MacFarlane, P.M. Gschwend, Environmental Science and Technology 31 (1997) 203.

[60] K.G. Neoh, J.B. Howard, A.F. Sarofim, in:, Part. Carbon: Form. Combust., [Proc. Int. Symp.], Plenum, 1981, pp. 261–282.

CHAPTER 6

SOOT OXIDATION-INDUCED FRAGMENTATION: PART 2: EXPERIMENTAL INVESTIGATION OF THE MECHANISM OF FRAGMENTATION

6.1 Introduction

Soot is formed in a flame under complex steps including the molecular precursor formation, particle inception, coagulation, and growth [1–3]. As result of collisions between particles, aggregates consisting of a large number of primary particles can be formed [4,5]. Following this, aggregates are destroyed through two parallel processes: oxidation and fragmentation [6]. Fragmentation is the process of breaking up particle aggregates into smaller ones, reflected by the observable increase of ultrafine particles. The fragmentation of soot in the flame was first experimentally observed by Neoh et al. [7,8], where soot oxidation and fragmentation was studied in a two-stage burner. Soot was produced in a first-stage premixed burner and then oxidized in a second stage. They saw evidence of fragmentation at higher fractional carbon burnout, around 0.7-0.8 for a methane-air premixed system. Two hypotheses were presented: that fragmentation was a result of oxygen diffusion in bridges between particles which then burn and break apart; or, that oxygen diffuses into a primary particle, causing internal burning, increasing particle porosity, and eventually breaking it apart. Garo et al. [9] also saw evidence of soot fragmentation, occurring at approximately 0.75 fractional burnout for a methane-air diffusion flame. Puri and coworkers' [10] observations in a laminar ethylene diffusion flame showed that when soot particles are transported further downstream, where coagulation was not dominant, the degree of particle aggregation started to decrease. They concluded that this observation was related to the soot oxidation-induced fragmentation. Xu et al. [11] reported that soot aggregate fragmentation occurred in the oxidation region in their experimental study of a laminar C_2H_4/air diffusion flames at atmospheric pressure. Recently, soot fragmentation was also studied by Echavarria et al. [12] with an experimental configuration similar to Neoh et al. [8]. A scanning mobility particle sizer (SMPS) was used to obtain particle size distributions (PSDs) and to characterize fragmentation in an ethylene flame.

Numerical models have also shown the importance of fragmentation to correctly predict particle burnout and particle size in flames. Zhang et al. [13] showed that, without considering fragmentation, there is a discrepancy between model prediction and experimental measurement of particle mobility diameter during oxidation. He assumed that the fragmentation was the result of breaking the weak bonds connecting primary particles in an aggregate structure. Harris and Maricq [14] used an arbitrarily chosen fragmentation rate to predict the steady-state soot particle size distribution. They showed that the addition of soot aggregate fragmentation to the Schmoluchowski aerosol coagulation model significantly improved their model predictions; without fragmentation, the model over-predicted the number of particles at larger particle diameters. Mueller et al. [6] developed a model within the hybrid method of moments (HMOM) to predict particle size distribution by taking into account the fragmentation of aggregates. They considered a mechanism of the fragmentation based on the idea of internal burning. More recently, Sirignano et al. [15,16] used a discrete sectional model to give a further proof of the importance of fragmentation in determining the final amount and the morphology of the particles in a counter flow diffusion flame as well as a premixed flames.

The lack of data on soot fragmentation has been a barrier in identifying the appropriate mechanisms. A better understanding of the soot fragmentation processes can improve the existing models for predicting size distribution and mean properties of particles as they undergo oxidation. The goal of this study is to systematically perform a set of experiments to identify the mechanism of fragmentation. The experiments can be classified as follows,

1- The effect of flame temperature on fragmentation by using various diluent gases (N_2, *Ar, He*) (Section 3.1)

2- The effect of flame temperature on fragmentation by altering the nitrogen-to-oxygen ratio (Section 3.2)

3- The effect of fuel-lean and fuel-rich condition on fragmentation (Section 3.2)

4- The effect of variation in the mobility particle size on fragmentation (Section 3.3)

6.2 Experimental setup

The experimental setup is schematically shown in Figure 6.1. The experiments were carried out in a two-stage burner similar to that used in previous studies [12,17,18]. An ethylene stream (A-3) and air stream (A-1) were mixed in the manifold (M-1) and then passed to the premixed section of the first-stage burner (stainless steel pipe, 51 mm ID, Schedule 80, 127-mm long). A fuel/air mixture was burned under a fuel-rich condition (see Table 6.1) in a laminar premixed flame at atmospheric pressure in the first-stage,

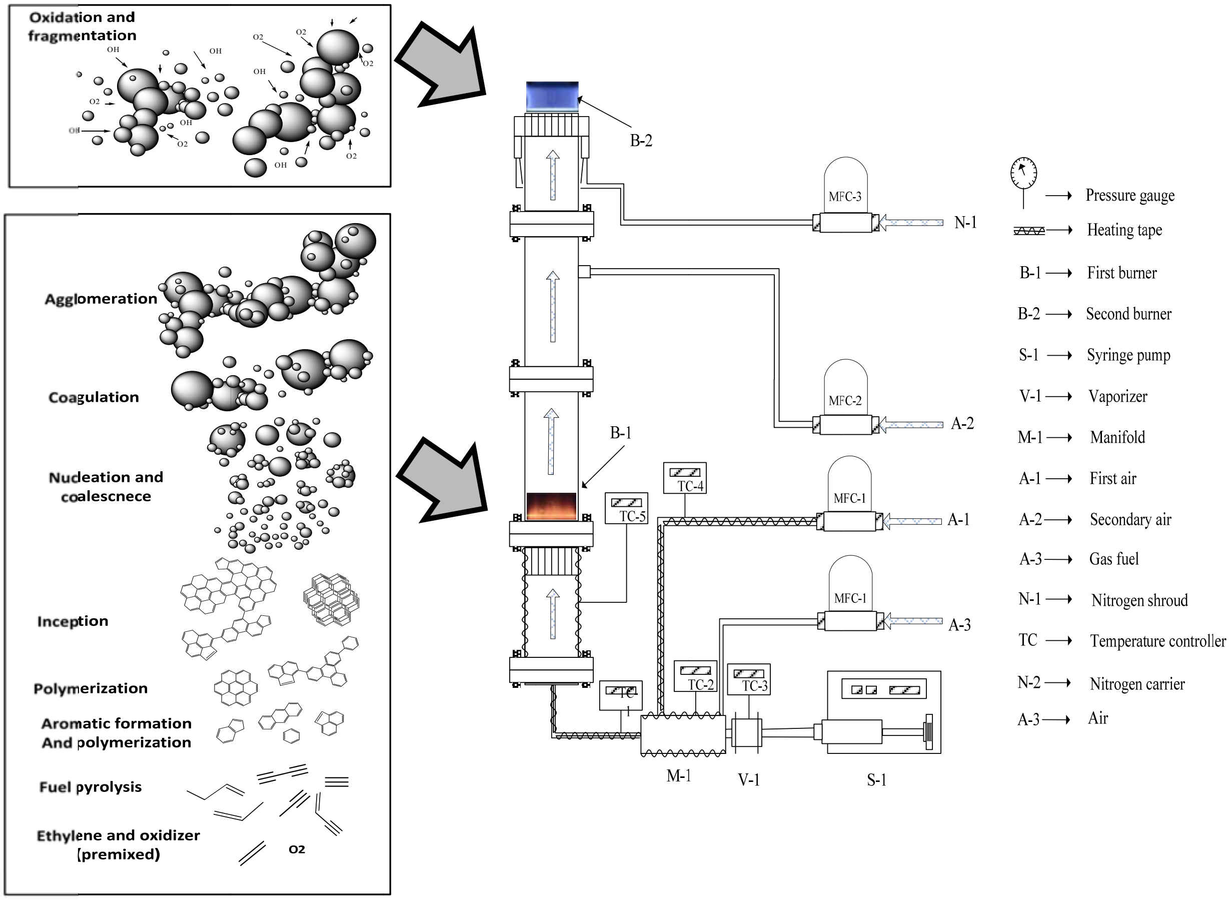

Figure 6.1. Schematic representation of the two-stage burner. History of soot formation and oxidation is illustrated to the left (adapted from Bockhorn [23]).

Table 6.1. Experimental conditions.

#	$\emptyset_1^a$	$\emptyset_{\text{Overall}}^b$	ϑ^c	Secondary oxidizer composition
Case 1 (base case)	1.98	0.9	3.77	$21\%O_2$–$79\%N_2$
Case 2	1.98	0.9	3.77	$21\%O_2$–$79\%Ar$
Case 3	1.98	0.9	3.77	$21\%O_2$–$79\%He$
Case 4	1.98	0.9	3.77	$60\%O_2$–$40\%N_2$
Case 5	1.98	1.15	3.77	$21\%O_2$–$79\%N_2$
Case 6	1.80	1.10	3.77	$21\%O_2$–$79\%N_2$

[a] Equivalence ratio in the first burner

[b] Overall equivalence ratio

[c] Cold gas velocity, cm/s (STP)

resulting in soot formation in the form of primary particles and aggregates, along with a gas mainly composed of H_2, CO, CO_2, N_2, and H_2O. The secondary oxidizer stream (A-2) was introduced into the mixture. Products were oxidized under slightly lean or rich condition, in the second premixed flat-flame burner. The two-stage burner separates the formation process (first burner) from oxidation (second burner). The flame was stabilized through a tube bundle (1/16"ID, 1" long) and a nitrogen shroud was used to isolate the flame from surrounding air. Whereas the cold-gas velocity was constant, the equivalence ratio in the first burner was adjusted by changing the ratio of fuel stream (A-3) to air stream (A-1) and the overall equivalence ratio was defined by the ratio of fuel to total oxidizer (oxygen in the bottom and top burners) fed into the burner over the stoichiometric ratio:

$$\emptyset_{\text{overall}} = \frac{\left(\frac{\text{Fuel(A}-3)}{\text{Oxygen(A}-1)+\text{Oxygen(A}-2)}\right)_{\text{Actual}}}{\left(\frac{\text{Fuel}}{\text{oxygen}}\right)_{\text{Stochiometric}}} \tag{6.1}$$

To investigate soot fragmentation, we carried out a wide range of experiments (reported in Table 6.1). These experiments were designed to investigate the effect of equivalence ratio in the first burner ($\emptyset_1$), the overall equivalence ratio ($\emptyset_{\text{overall}}$), and the composition of secondary oxidizing stream on the fragmentation. Changing $\emptyset_1$was achieved by adjusting the ratio of fuel stream (A-3) to the oxidizer stream (A-1); this directly affected the soot formation in the first burner and consequently the particle mobility size that appeared in the secondary burner.

The comparison between the Cases 5 and 6 demonstrated the result of changing the equivalence ratio in the first burner when the other parameters were kept the same. Changing $\emptyset_{\mathrm{overall}}$ impacted the flame temperature due to adding more or less oxygen (rich or lean flame). Cases 1 and 5 were performed to show the effect of $\emptyset_{\mathrm{overall}}$ on the fragmentation when the other parameters were the same. The composition of the secondary oxidizer stream was varied in two ways (i) mixing the same amount of O_2 with different inert gases such as N_2, Ar, and He (ii) using different concentrations of O_2/N_2 mixture. The different inert gases (Case 1, 2, and 3) were tested to study the diffusion and heat capacity effects on the fragmentation. In addition, different concentrations of O_2/N_2 (Cases 1 and 4) allowed for investigating the effect of nitrogen dilution which also changed the flame temperature.

Temperature and particle size distributions (PSDs) were found for all cases and specific gas-phase compounds were measured for the Cases 1, 2, and 3. All measurements were performed in the centerline of the flame at different heights above the secondary burner (HABs). The flame temperature was measured using an uncoated 0.2032-mm Pt/Rh 70%/30% thermocouple (Type B). The radiation correction for the temperature was similar to that of McEnally et al. [19].

PSDs were found with online sampling using a scanning mobility particle sizer (SMPS) including a TSI 3080 classifier and a 3025 ultrafine condensation particle counter coupled to a 3085 nano-DMA. The SMPS was optimized to operate in the 3-135 nm range with a sheath flow of 15 L/min and an aerosol sample flow of 1.5 L/min. The SMPS sampling method was similar to that used by Zhao et al. [20]. The validity and reliability of the SMPS sampling procedure and data acquisition have been extensively discussed [20,21]. The sampling probe was placed horizontally and the orifice (0.24 mm) was faced down toward the incoming flame gas above the burner. The probe was mounted on a translation stage with the accuracy of probe positioning estimated to be 0.1 mm. The soot-laden gas sample was immediately diluted by nitrogen at the rate of 30 L/min (STP) to quench oxidation reactions, and minimize particle coagulation and thermophoretic deposition. Zhao et al. [20] showed that particle diffusion losses and particle coagulation can be minimized by systematically increasing the dilution ratio to a critical value where the particles size distribution function becomes independent of the dilution ratio. The pressure difference across the probe orifice was adjusted with the aid of two U manometers to obtain a desired dilution ratio. The corrections for penetration efficiency into the probe and probe orifice and diffusion losses during transport were applied following the procedure presented by Minutolo et al. [22].

The evolution of the combustion gas-phase species was isokinetically sampled by a system involving a water-cooled probe which was coupled to a particle filter and a chiller for removing particles and water before entering an online micro gas-chromatography analyzer micro-GC (VARIAN, CP-4900). Similar to the SMPS sampling probe, the GC probe was pointed down toward the incoming flame gas above the burner. It was mounted on a translation stage, then its vertical position could be varied with respect to the burner. The accuracy of probe positioning was estimated to be around 0.1 mm.

6.3 Results and discussion

6.3.1 The effect of different inert gases on fragmentation

To understand the role of inert gases in the soot oxidation, the effect of adding N_2, *Ar*, and *He* (Cases 1, 2, and 3) was investigated. These experiments included a highly diffusive species (*He*) and two near equidiffusive species (*Ar*, N_2). All combustion parameters were kept the same ($\emptyset_1$, $\emptyset^{a}_{overal}$, and ϑ) for three cases, while the primary oxidant (O_2) was mixed with *Ar*, N_2, and *He* in the secondary gas stream. Figure 6.2 shows the temperature profiles for three flames where the maximum temperature was approximately 1480, 1560, and 1600 K for Cases 3 (*He*), 1 (N_2), and 2 (*Ar*), respectively.

The error bars are the result of either uncertainty in the sampling process or uncertainty due to limitations in the precision of measuring devices. The smaller heat capacity of *Ar* compared to N_2 resulted in a slightly higher temperature for Case 2 in contrast with the base case (Case 1), supported by the literature [23]. For *He* addition, the temperature response was more complex. Although argon and helium have the same heat capacity, their temperatures are different. Based on the calculation of Le number (larger Le for *He*), this variation in temperatures can be due to the difference in the diffusivity of these two species [24,25]: the thermal diffusivity of helium is higher than that of argon, because the molecular weight (and, therefore, the density) of helium is much smaller.

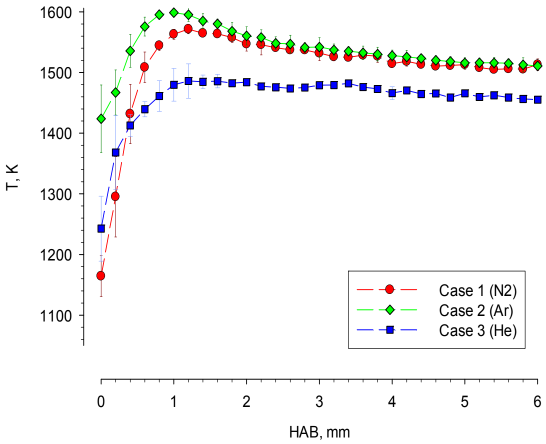

Figure 6.2. The measured and radiation-corrected temperature profiles for Cases 1 (N_2, base case), 2 (*Ar*) and 3 (*He*) as a function of HAB.

To obtain a better understanding of fragmentation, the number density is plotted against particle mobility diameter for some selected heights. PSDs for some selected HABs are presented in Figure 6.3 for N_2 (base case) as an example. The uncertainties given at each point may be classified in the same two categories as mentioned above. Because of the same equivalence ratio in the first burner, the PSDs were similar for all three cases immediately on the burner surface.

The fragmentation was identified by the observable increase in ultrafine particle numbers (below 10 nm). For N_2, the PSDs remained unimodal until the height 2.4 mm, then a bimodal size distribution behavior started to evolve indicating fragmentation. The fragmentation lasted up to 3.8 mm, after which it disappeared.

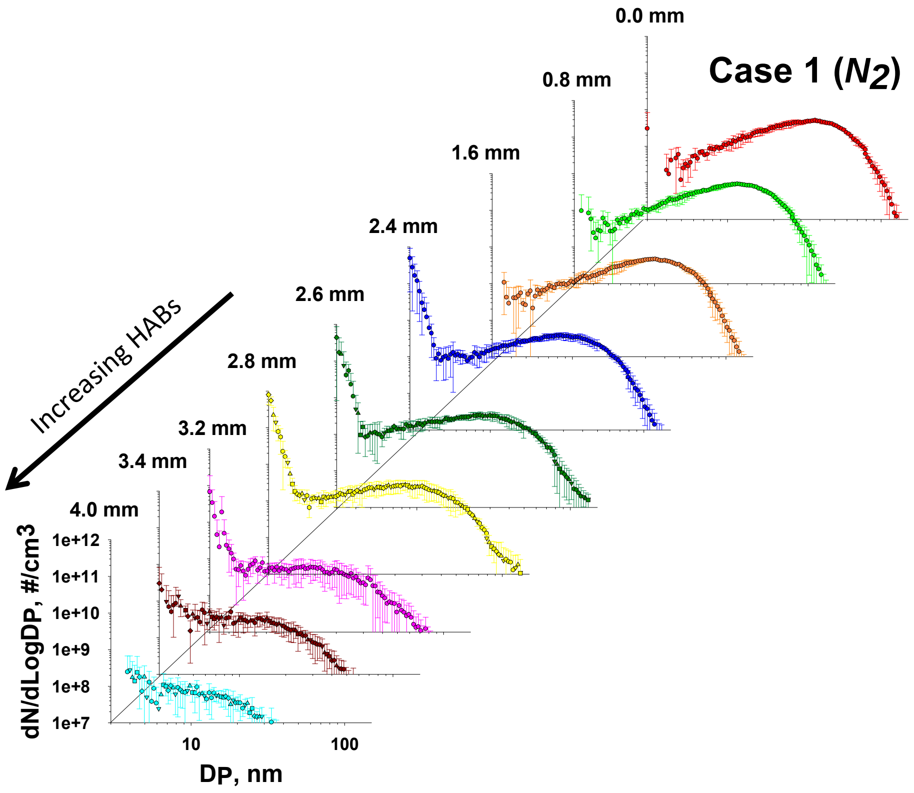

Figure 6.3. An example of PSDs at selected HABs for N_2 (base case)

Figure 6.4 helps to better understand the fragmentation for each flame by plotting the particle number density integrated for ultrafine particles (3-10 nm) versus HABs. The PSD measurements were performed every 0.2 mm above the burner. Similar to N_2, the fragmentation started for *Ar* at the same height but at a lower extent and it disappeared faster, around 3.2 mm. On the contrary, the fragmentation for *He* appeared at lower heights, around 1.2 mm, and reached its maximum at 4.2 mm. The amount of fragmentation was also higher as evidenced by the higher integrated number densities. Figure 6.4 shows that the lowest extent of fragmentation was for *Ar* followed by N_2 and *He*. Figure 6.4 and Figure 6.2 illustrate that the highest extent of fragmentation occurred with *He*, which also showed the lowest peak temperature. In contrast, *Ar* had the maximum peak temperature and the lowest extent of fragmentation. These results show the apparent effect of peak temperature on the extent of fragmentation.

The first potential explanation involves the effect of different peak temperatures on the concentration of oxidizing species (O_2, OH). In order to investigate this effect, GC

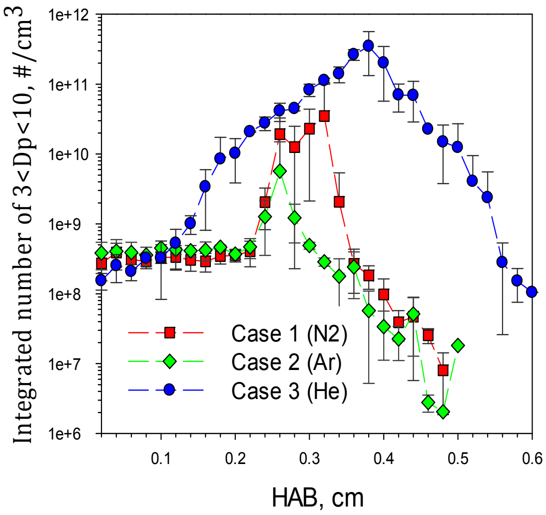

Figure 6.4. Integrated particle number density integrated for ultrafine particles (3-10 nm)

measurements were performed, coupled with kinetic modeling. Experimental mole fractions of H_2, CO, CO_2, O_2, were measured using an online *GC* analyzer. Temperature profiles were input into a CHEMKIN [26] simulation to eliminate the need to model heat losses in the energy equation. Other experimental measurements at the surface of top burner (mass flow rate, H_2, CO, CO_2, O_2 concentration) were also used as inputs. CHEMKIN modeling couples a 1D-premixed code to a detailed kinetic model developed by Ranzi et al. [27]. The model results were shifted downstream to account for cooling due to the sampling probe [20,23]. Experimental and model prediction concentration profiles of the major gas-phase species and *OH* radical are shown in Figure 6.5 for N_2, *Ar*, and *He*. The evolution of the gas species was similar for three cases; the maximum *OH* concentration was reached at a HAB around 3 mm for N_2 and *Ar*, while a delay was observed for *He*. Good agreement was obtained between the model results and the experimental data for the major gas species.

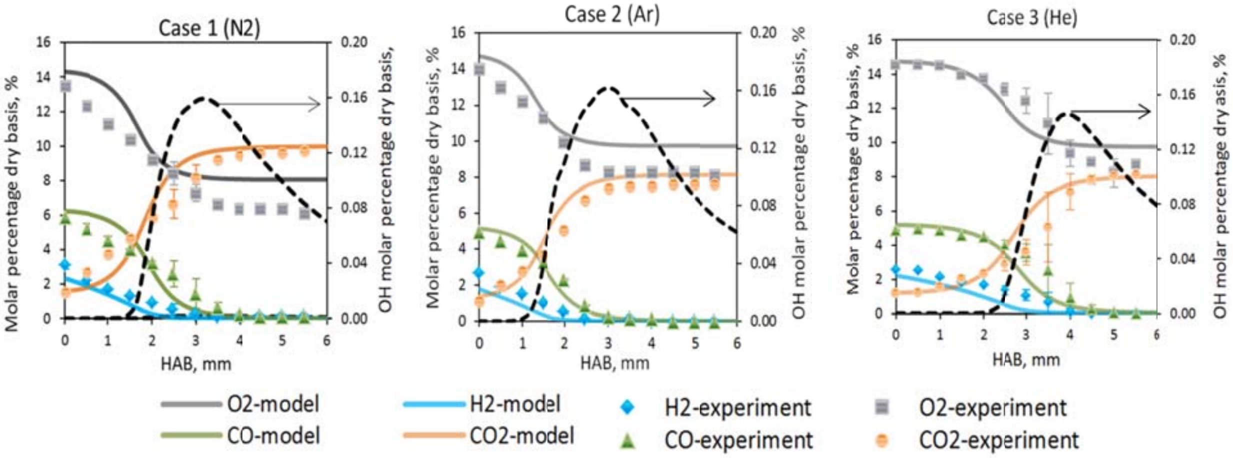

Figure 6.5. Concentration versus HAB for major gas-phase species with N_2, *Ar*, *He* addition in the second burner (left axis). The *OH* concentration scale is shown on the right. Symbols correspond to experimental results and solid and dashed lines correspond to the model predictions.

The model results show no differences in the concentration of the oxidizing species, specifically the *OH* radical and O_2 concentration, so it is unlikely that this is the cause of the differences in fragmentation. Possible explanation can be proposed by investigating the effect of temperature change on the soot burnout. Integrated mass of the entire particle mobility diameter range, 3-135 nm, is plotted versus HAB in Figure 6.6 as an indication for soot burnout. The fastest burnout appeared for *Ar* which had the maximum peak temperature. N_2 had a peak temperature slightly lower than *Ar* and the mass change was also slightly delayed. *He* showed much slower burnout, consistent with its peak temperature. The extent of fragmentation was found to be correlated with temperature.

In the flame temperature, soot can be oxidized when it reacts with O_2 and *OH* [11, 28]. The oxidation rate by O_2 is usually orders of magnitude slower than *OH* rate [18,29]. The lower O_2 rate will likely give O_2 molecules the ability to diffuse within the pores of soot nanostructure, before reacting with an active site. This will probably result in internal burning, increasing the porosity, and finally enhancing the breakup process.

Although the contribution of O_2 to the overall burnout process may be low, it may be

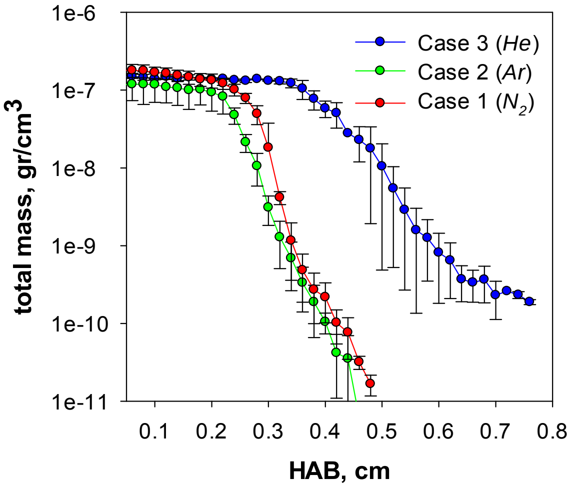

Figure 6.6. Integrated mass density for particles with mobility diameter between 3 and 135 nm.

sufficient to affect the structure of the soot aggregate, as stated by Neoh et al. [29]. Once *OH* is formed, its higher reactivity will dictate that it will probably react on the surface of the particle, and *OH* diffusion into pores will be in a much smaller extent than O_2 molecules. The combined effects of internal burning and external surface regression may cause soot aggregates to break at bridges after a certain extent of burnout [29]. Part 1 showed that the nanostructure of the bridges were such that they had the potential to be more reactive, and selective burnout may occur. Experimental data given here suggest that the temperature has a major effect on fragmentation through changing the overall oxidation. As illustrated in Figure 6.6, at higher flame temperatures (*Ar* flame), soot burnout occurred quickly, probably burning aggregates before they could fragment. The opposite behavior is expected for lower temperatures, such as the case in *He* flame. At decreased temperature, soot burnout was delayed and subsequently, small particles produced after fragmentation persisted in the flame for a longer time.

6.3.2 The effect of increase in N_2 dilution and O_2 concentration

In Cases 1 and 4, the variation of the maximum flame temperature in the secondary flame was manipulated by changing the mean specific heat of the flame gas mixtures, achieved by altering the nitrogen-to-oxygen ratio in the secondary gas oxidizer. The flame condition was the same for both Cases in the first burner implying the same amount of soot formed in the first stage. The main difference was in the composition of the secondary air which was 60% O_2/40% N_2 for Case 4 versus the base case 21% O_2/79% N_2. Because of the similarity in the overall equivalence ratio, the same amount of oxygen was introduced in both cases from the oxidizer stream. But due to different secondary air compositions, the nitrogen molar flow rate was lower in 60% O_2/40% N_2 (0.0015 mole/s) than air (0.0037 mole/s). Given this change in the N_2 flow rate, the oxygen molar fraction (X_{O2}) initially on the secondary burner was higher in Case 4 (26%) as compared to the base case (15%). The temperature measurements illustrated in Figure 6.7 show a slightly increased temperature for Case 4, higher O_2, as compared to air. The integrated particle number density for ultrafine particles, Figure 6.8, illustrates that fragmentation did not occur for Case 4 as compared to the base case.

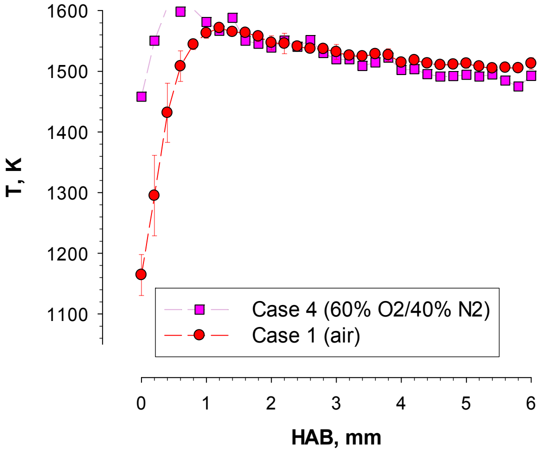

Figure 6.7. The radiation-corrected temperature profiles for Case 1, and Case 4, as a function of HABs with the maximum peak temperature 1560 K and 1600 K.

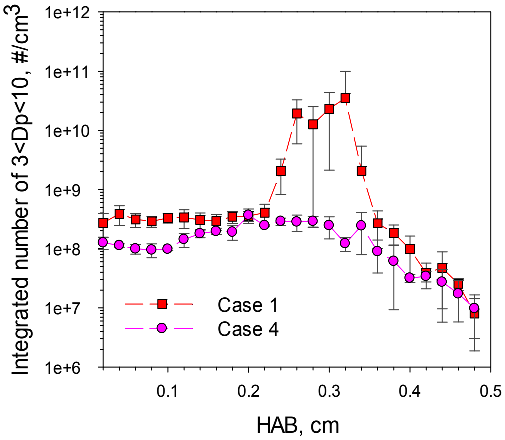

Figure 6.8. The particle number density integrated for ultrafine particles (3-10 nm) for base case with air (Case 1) and higher oxygen case (Case 4).

This observation is consistent with the effect of temperature discussed in the previous section, as lower peak temperature resulted in a higher extent of fragmentation.

To further investigate temperature, a fuel-rich condition (Case 5) versus the base-case fuel-lean condition (base case) was compared. The equivalence ratio in the first burner was the same, but the overall equivalence ratio was different, 1.15 for Case 5 and 0.9 for the base case. This difference was accomplished by changing the flow rate of the secondary air. The temperature profile measurement illustrated in Figure 6.9 shows the higher peak temperature for the leaner case, which can be attributed to an increased oxygen concentration in the flame.

The integrated particle number density for ultrafine particles is shown for both cases in Figure 6.10a. The fragmentation started at early stage, around 1.2 mm for Case 5 while it was at 2.2 mm for the base case. The fragmentation lasted until higher heights for Case 5, but it disappeared for the base case at the height around 3.2 mm. Again, Case 5 showed a higher fragmentation than the base case. The initial oxygen concentration in the base case ($X_{O2} \cong 0.14$) was higher than that of Case 5 ($X_{O2} \cong 0.08$). The higher extent

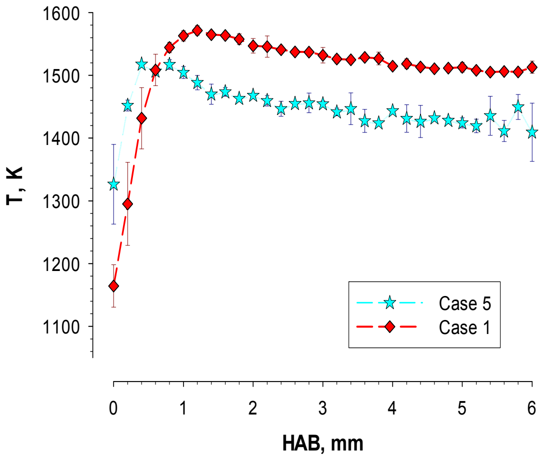

Figure 6.9. The radiation-corrected temperature profiles for fuel-lean (Case 1) and fuel-rich (Case 5) versus HABs with the maximum peak temperature 1520 K and 1560 K.

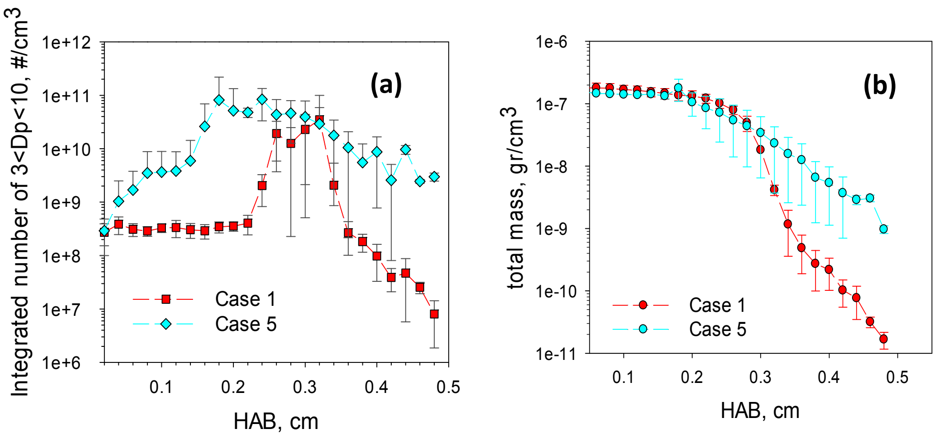

Figure 6.10. The particle number density integrated for ultrafine particles (3-10 nm) (a) and the total mass density integrated for particles (3-135 nm) (b)

of fragmentation in Case 5 showed that temperature, not oxygen concentration, was more important in fragmentation. As illustrated in Figure 6.10b, faster burning was evident for the base case consistent with its higher peak temperature, similar to the previous results. This observation shows the impact of overall burnout on the fragmentation over the oxygen concentration; in fact the oxidation-induced fragmentation can be seen as a particular event of the overall oxidation.

6.3.3 The effect of mobility particle diameter on fragmentation

The effect of particle mobility diameter on fragmentation was also investigated through Cases 5 and 6, two overall rich cases. Case 6 had a slightly leaner flame in the first burner as compared to Case 5. The overall equivalence ratio in Case 6 was adjusted such that the oxygen concentration in the second burner was comparable to the concentration in Case 5. The temperature profiles for two cases are shown in Figure 6.11. As seen in the figure, Case 6 (leaner flame) had a lower temperature with the maximum 1420 K as compared to Case 5 (richer flame) with the maximum 1520 K.

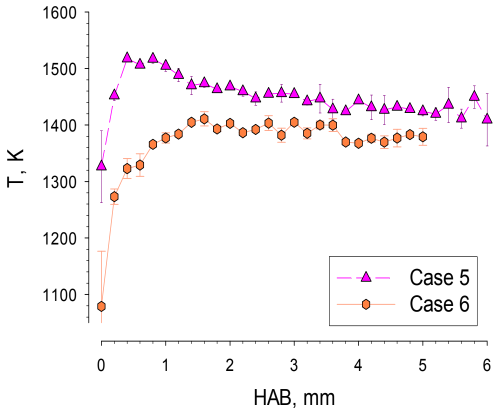

Figure 6.11. Temperature profile for Cases 5 (first burner fuel-rich) and Case 6 (first burner leaner).

Based on the observation from previous sections, one may expect the fragmentation to be higher for Case 6 because of its lower peak temperature. However, Figure 6.12a shows just slight increase in ultrafine particles for Case 6 (lower peak temperature) at higher HABs, indicating a low extent of fragmentation, while there was substantial increase in ultrafine particles for Case 5 (higher peak temperature). The possible explanation can be determined by considering the PSDs of both cases at the burner face (Figure 6.12b). The PSDs at HAB=0 mm showed the maximum mobility particle for Case 5 (richer flame) to be 135 nm versus 80 nm for Case 6 (leaner flame). The difference in the maximum mobility size indirectly indicates the presence of larger aggregates in Case 5, since the primary particles can be assumed in the range of 20-80 nm in diameter [30–32]. The presence of aggregates was possible in both cases, but aggregates were obviously smaller in Case 6 in terms of size and number density. Given the lower temperature, the previous results suggest a higher extent of fragmentation for Case 6; however, lack of fragmentation for Case 6 shows the importance of aggregates in the onset of fragmentation. It is possible that the smaller particles were burned out prior to fragmentation, and not caught by the measurements.

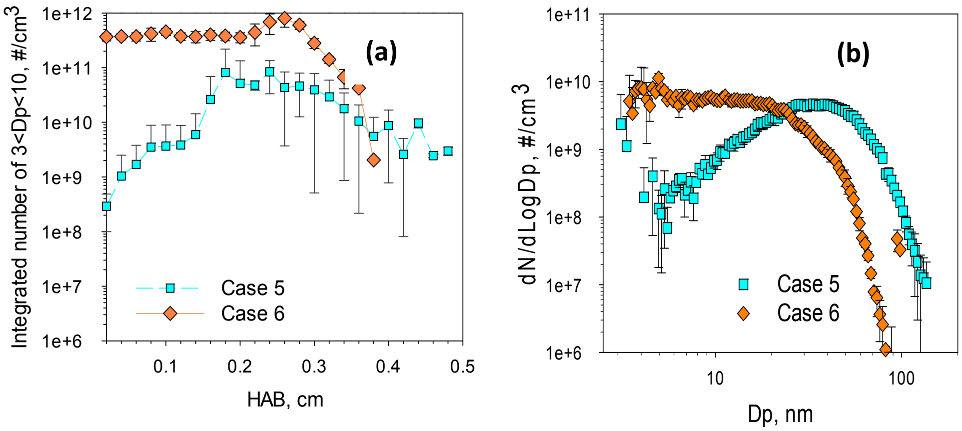

Figure 6.12. The particle number density integrated for ultrafine particles (3-10 nm) (a). PSDs immediately on the secondary burner for Case 5 and 6 (b).

Since O_2 has been considered as an important factor in fragmentation, one may suspect that the fragmentation in Case 5 may be the result of higher O_2 concentration. The concentration profiles given in Figure 6.13 show a comparable O_2 profile for Case 6 and Case 5 for the region of interest. The results showed that the onset of fragmentation depends on the presence of aggregates in the flame which is related to the formation step. During the soot formation, aggregation starts as soon as ultrafine particles nucleate out of the gas-phase [33]. The intense particle nucleation at richer flame results in a vast supply of newly nucleated particles [34]. The size of these nucleates are approximately in the

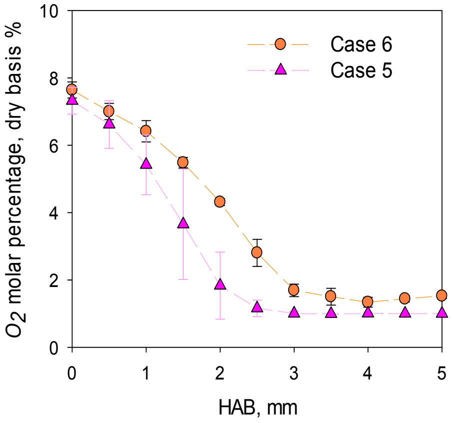

Figure 6.13. O_2 concentration versus HAB for Case 5 and 6.

size range of 3-10 nm evidenced by the small-size mode in the bimodal distribution [23,35]. These ultrafine particles can coagulate with each other or with other larger particles. Immediately after coagulation, particles are approximately in point contact, creating a small zone between two particles which is a preferred site for growth [36]. The growth between two particles results in forming a narrow bridge. If the growth rate becomes high enough, this may cause a significant surface deposition in the bridge area that ultimately buries the particle stuck to the form of individual particle [34]. If the rate of nucleation is faster than surface deposition, then a considerable number of small particles remain on the body of particle [34] in a point contact or with a narrow bridge. More recently, Schenk et al. [37], by using helium-ion microscopy (HIM), confirmed that primary particles synthesized in the ethylene flame are not perfectly spherical. This implicitly implies the presence of freshly nucleated particles in the structure of particles which are more susceptible to be detached during the oxidation because the bridges between particles have a higher oxidative reactivity (as shown in Part 1). This leads to the release of ultrafine particles as well as the removal of small fragments from the edges of the primary particles surface.

6.3.4 Soot burnout

The corresponding modeling of the burner system (Figure 6.5) showed that, close to the burner surface, the flame was dominated by fuel (H_2 and CO) and oxidizer (O_2). Once the fuel started to burn and O_2 was consumed, OH radicals were formed. Therefore, two regions can be specified in the flame: (i) the region with high O_2 concentration (ii) the region where O_2 is dropped and OH is formed. It has been shown that OH is the main oxidizer in the flame and responsible for burning soot particles [29,38–40]. The data can be used to show whether fragmentation occurs only before *OH* formation or whether it continues in *OH*. Soot mass conversion is defined as the fraction of soot mass which has been oxidized (soot burnout). Soot mass conversion is determined by the ratio of the instantaneously converted amount to the initial amount based on the following formula,

$$mass\ conversion, \% = (1 - \frac{m_i}{m_0}) \times 100 \tag{6.2}$$

where m_i is the total soot mass per unit volume at any height above the burner and m_0 is the total soot mass per unit volume at HAB = 0 cm. Figure 6.14, a plot of soot mass conversion, total ultrafine particles, and soot mass versus HAB, helps ascertain when fragmentation occurs. The rapid increase in conversion (the green dots) occurred in the flame front where *OH* was formed (i.e. Figure 6.4). As discussed previously, Cases 6 and 4 did not show any fragmentation. Fragmentation occurred for *He* (Case 3), fuel-rich (Case 5), the base case (Case 1), and argon (Case 2), with the extent, based on number of small particle mobility diameters, in the order given. The fragmentation started for the base case, air, and argon at the mass conversion around 20% and it continued, reaching a peak around 60-80% conversion. This result is consistent with that by Neoh et al. [7] who also showed that fragmentation happened at higher soot burnout, around 70%. For the cases with a higher extent of fragmentation, Cases 3 and 5, fragmentation was observed to start at a lower mass conversion, between 5 and 10% and the maximum was reached at conversion around 40%. Since *OH* is the principle oxidizer, the presence of fragmentation at such a high mass conversion showed that the fragmentation continued in

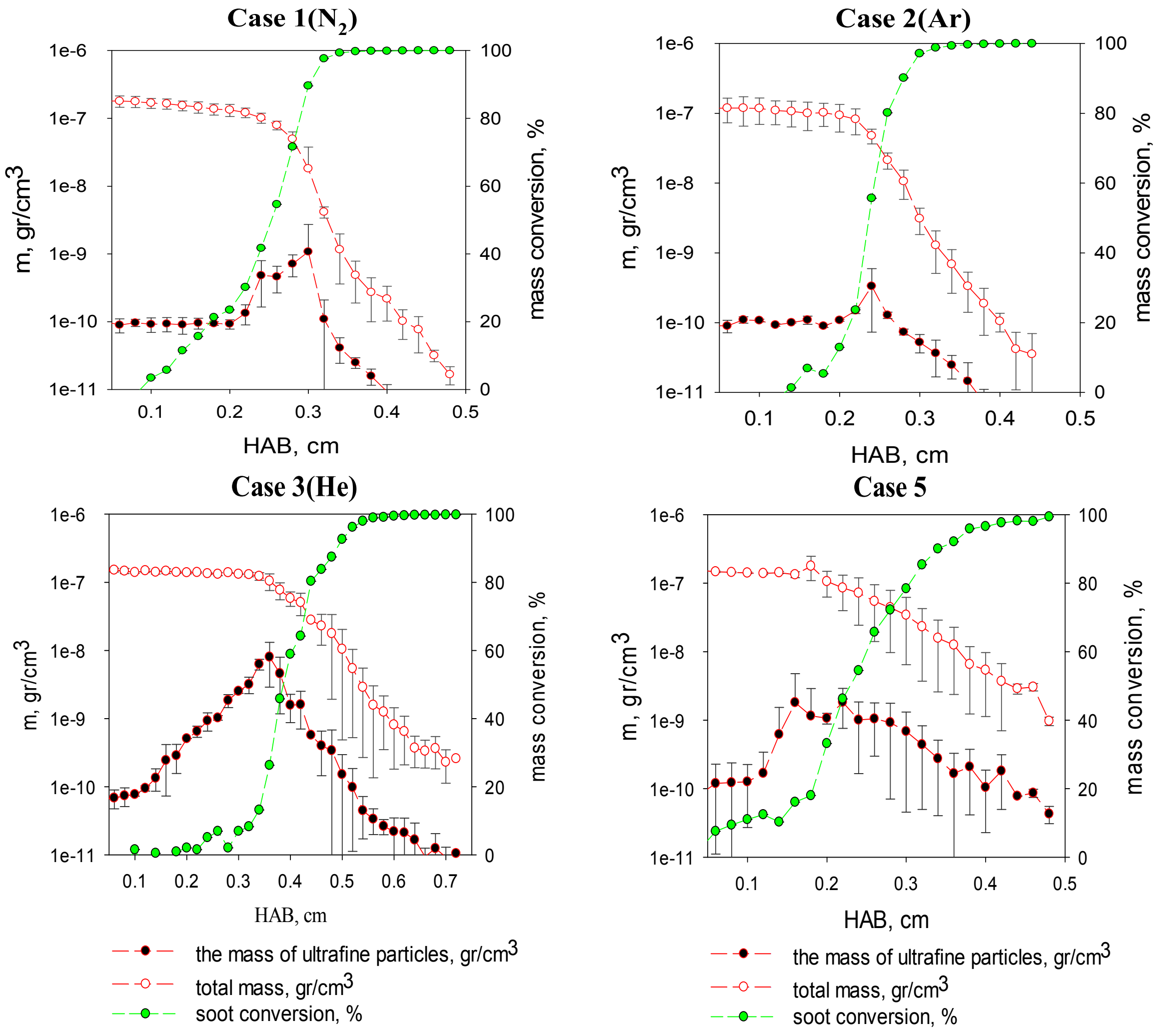

Figure 6.14. Mass conversion, total soot mass, and mass of ultrafine particles for Cases 1(N_2), 2(Ar), 3(He), and 5(fuel-rich). (Note: the cases are shown here in which the fragmentation was observed.)

OH region. As a result, reducing temperature slowed down the oxidation rate by the *OH* and gave enough time for oxygen to penetrate into the bridges, which were found to be more reactive, and helped the structure break apart. Echavarria et al. [18] hypothesized that the fragmentation at low burnout was the result of breaking up the bridges (or necks) between primary particles which our findings demonstrate; however, that fragmentation appears to continue from low burnout to higher burnout.

6.3.5 The role of *OH* radicals in the fragmentation

OH concentration can also impact the fragmentation rate due to its role in the soot oxidation. *OH* has been shown to be the most dominant oxidizer in flames [8,32,38,40,41], due to its faster rate. The mechanism of oxidation by *OH* is based on surface reactions defined by a collision frequency [7]. A temperature reduction in the second burner (oxidation zone) could reduce the number of successful collisions which remove carbon mass. The population of active sites is also another parameter that could affect the successful collisions through the following analysis [42].

Assuming *OH* radicals are released at a distance of $R+a$ from the surface of a sphere of radius *R*, the probability (P_a) that *OH* hits the surface of the soot at least once before leaving is,

$$P_a = \frac{R}{R+a} \tag{6.2}$$

The probability that this *OH* will execute *n* touches on the surface, wander away at *r* = $R + a$, and diffuse to infinity, is $P_a^n(1-P_a)$. The probability of not hitting an active site in a single random encounter is $\beta = 1 - (Na^2)/4R^2$. Furthermore, the probability that a radical survives all subsequent contacts until it escapes to infinity is:

$$P_{esc} = \sum_{n=0}^{\infty} \beta^n P_a^n\,(1-P_a) = \frac{(1-P_a)}{(1-\beta P_a)} \tag{6.3}$$

By substituting $P_a$and β, Eq (3) can be reduced to:

$$P_{esc} = \frac{4R}{(4R + Na)} \tag{6.4}$$

Equation 4 shows that the probability of OH escaping is inversely proportional to N (number of active sites). The bridges demonstrate a less-ordered structure (from Part 1) which has been shown to lead to higher oxidative reactivity [43,44]. This implies that there are likely more reactive sites (radical sites [45,46]) in the bridges. The presence of differences in reactive sites and reactivity has been discussed by others as well [45]. Accordingly, the higher OH oxidation rate in the bridges would lead to loss of connectivity in the aggregate structure. This in turn would lead to fragmentation of aggregates as well as the removal of small fragments from the edges of the primary particles surface.

6.4 Conclusion

A set of experiments was designed in a two-stage burner to further understand fragmentation during oxidation using ethylene fuel. To compare the results, all experiments were classified in three categories of study: (i) the effect of different inert gases, *Ar*, *He*, N_2; (ii) the effect of increase in N_2 dilution and O_2 concentration; (iii) and, the effect of mobility particle size on the fragmentation. Based on the experiments, two main results were obtained: First, the onset of the fragmentation depended on the presence of large aggregates in the flame. Second, in the presence of aggregates, the extent of the fragmentation was inversely proportional to the peak temperature.

Case 6 had a smaller size distribution with the maximum mobility size around 80 nm, and it was mainly dominated by particles less than 20 nm in diameter. No fragmentation was observed for this case although the flame temperature was low and more favorable for fragmentation. On the other hand, in larger size distributions, e.g., Case 5, with the maximum mobility diameter around 135 nm, fragmentation occurred. This difference in the maximum mobility size indirectly indicated the presence of larger aggregates for Case 5 as compared to Case 6. This observation showed the importance of aggregates in the onset of fragmentation.

For cases with larger mobility size distributions, the amount of fragmentation was found to be inversely proportional to the peak temperature. At higher flame temperatures, soot burnout occurred quickly, probably burning aggregates before they could fragment. In contrast, the lower temperatures resulted in slower soot burnout which helped the fragmentation process in two ways: first, likely giving O_2 molecules enough time to diffuse and internally burn, second, allowing the fragmented particles to last longer in the flame before being oxidized. Furthermore, the impact of temperature on the overall soot burnout was found to be more effective than O_2 oxygen concentration. In fact, the oxidation-induced fragmentation can be seen as a particular event of the overall oxidation.

Fragmentation occurred, not only before OH formation, as evidenced in the lower temperature studies, but also in regions where OH radicals were formed. By probability analysis, a role for OH radicals was postulated by suggesting a selective burning in bridges that resulted in the loss of connectivity in the aggregate structure. The combined effects of internal burning and external surface regression may cause soot aggregates to break at bridges after a certain extent of burnout. It was shown that fragmentation can be started at very early burnout (~10%), and it can reach its peak at higher burnout (~70%).

6.5 References

[1] D.B. Kittelson, W.F. Watts, J.P. Johnson, Journal of Aerosol Science 37 (2006) 913.

[2] M. Frenklach, D.W. Clary, T. Yuan, J. Gardiner, W. C., S.E. Stein, Combustion Science and Technology 50 (1986) 79.

[3] M. Frenklach, Phys. Chem. Chem. Phys. 4 (2002) 2028.

[4] J.C. Zahnow, J. Maerz, U. Feudel, Physica D 20 (2011) 882.

[5] S. Rothenbacher, A. Messerer, G. Kasper, Particle and Fibre Toxicology 5 (2008) 1.

[6] M.E. Mueller, G. Blanquart, H. Pitsch, Proceedings of the Combustion Institute 33 (2011) 667.

[7] K.G. Neoh, J.B. Howard, A.F. Sarofim, in:, Twentieth Symposium (International) on Combustion, The Combustion Institute, Pittsburgh, 1985, pp. 951–957.

[8] K.G. Neoh, J.B. Howard, A.F. Sarofim, Particulate Carbon Formation During Combustion, Plenum Press, New York, 1981.

[9] A. Garo, J. Lahaye, G. Prado, Symposium (International) on Combustion 21 (1988) 1023.

[10] R. Puri, T.F. Richardson, R.J. Santoro, R.A. Dobbins, Combustion and Flame 92 (1993) 320.

[11] F. Xu, A.M. El-Leathy, C.H. Kim, G.M. Faeth, Combustion and Flame 132 (2003) 43.

[12] C.A. Echavarria, I.C. Jaramillo, A.F. Sarofim, J.S. Lighty, Proceedings of the Combustion Institute 33 (2011) 659.

[13] Q. Zhang, M.J. Thomson, F. Guo, H.; Liu, G.J. Smallwood, Combustion Science and Technology 182 (2010) 491.

[14] S.J. Harris, M.M. Maricq, Chemical and Physical Processes in Combustion 33 (2002) 227.

[15] M. Sirignano, J. Kent, A. D'Anna, Energy & Fuels 27 (2013) 2303.

[16] M. Sirignano, J. Kent, A. D'Anna, Proceedings of the Combustion Institute 35 (2015) 1779.

[17] H. Ghiassi, P. Toth, J.S. Lighty, Combustion and Flame 161 (2014) 671.

[18] Carlos A. Echavarria, I.C. Jaramillo, A.F. Sarofim, J.S. Lighty, C.A. Echavarria, Combustion and Flame 159 (2012) 2441.

[19] D.C.S. McEnally, U.O. Koylu, L.D. Pfefferle, D.E. Rosner, Combustion and Flame 109 (1997) 701.

[20] B. Zhao, Z. Yang, J. Wang, M. V. Johnston, H. Wang, Aerosol Science and Technology 37 (2003) 611.

[21] B. Zhao, Z. Yang, M. V Johnston, H. Wang, A.S. Wexler, M. Balthasar, M. Kraft, Combustion and Flame 133 (2003) 173.

[22] P. Minutolo, A. D'Anna, M. Commodo, R. Pagliara, G. Toniato, C. Accordino, Environmental Engineering Science 25 (2008) 1357.

[23] H. (Ed) Bockhorn, Soot Formation in Combustion Mechanisms and Models, 1994.

[24] A.D. Abid, N. Heinz, E.D. Tolmachoff, D.J. Phares, C.S. Campbell, H. Wang, Combustion and Flame 154 (2008) 775.

[25] D.X. Du, R.L. Axelbaum, C.K. Law, Combustion and Flame 102 (1995) 11.

[26] R.-H. Chen, M. Chaos, A. Kothawala, Proceedings of the Combustion Institute 31 (2007) 1231.

[27] R.J. Kee, J.F. Grcar, M.D. Smooke, J.A. Miller, Fortran Program for Modeling Steady Laminar One-Dimensional Premixed Flames., Sandia Natl. Lab., 1985.

[28] E. Ranzi, A. Frassoldati, R. Grana, A. Cuoci, T. Faravelli, A.P. Kelley, C.K. Law, Progress in Energy and Combustion Science 38 (2012) 468.

[29] B.R. Stanmore, J.F. Brilhac, P. Gilot, Carbon 39 (2001) 2247.

[30] F. Liu, B.J. Stagg, D.R. Snelling, G.J. Smallwood, International Journal of Heat and Mass Transfer 49 (2006) 777.

[31] B.S. Haynes, H.G. Wagner, Progress in Energy and Combustion Science 7 (1981) 229.

[32] P. Mitchell, M. Frenklach, Symposium (International) on Combustion 27 (1998) 1507.

[33] P. Mitchell, M. Frenklach, Physical Review E: Statistical, Nonlinear, and Soft Matter Physics 67 (2003) 061407/1.

[34] C.A. Echavarria, A.F. Sarofim, J.S. Lighty, A. D'Anna, Combustion and Flame (2011) 98.

[35] N.M. Morgan, R.I.A. Patterson, M. Kraft, Combustion and Flame 152 (2008) 272.

[36] M. Schenk, S. Lieb, H. Vieker, A. Beyer, A. Gölzhäuser, H. Wang, K. Kohse-Höinghaus, Proceedings of the Combustion Institute (2014).

[37] M.F.R. Mulcahy, B.C. Young, Carbon 13 (1975) 115.

[38] K.G. Neoh, J.B. Howard, A.F. and Sarofim, Soot Burnout in Flames, Massachusetts Institute of Technology, 1980.

[39] B.S. Haynes, H.G. Wagner, Zeitschrift Fuer Physikalische Chemie (Muenchen, Germany) 133 (1982) 201.

[40] C.P. Fenimore, G.W. Jones, Journal of Physical Chemistry A 71 (1967) 593.

[41] P. Roth, O. Brandt, S. Von Gersum, Symposium (International) on Combustion, [Proceedings] 23 (1990) 1485.

[42] H.C. Berg, E.M. Purcell, Biophysical Journal 20 (1977) 193.

[43] H. Ghiassi, J.S. Lighty, Combustion and Flame (2015).

[44] R.L. Vander Wal, A.J. Tomasek, Combust. Flame 136 (2004) 129.

[45] J.B. Howard, Symposium (International) on Combustion 23 (1991) 1107.

[46] D.E. Edwards, D.Y. Zubarev, W.A. Lester, M. Frenklach, The Journal of Physical Chemistry A (2014).

CHAPTER 7

CONCLUSIONS AND RECOMMENDATIONS FOR FUTURE WORK

Soot oxidation was studied by evaluating PSDs in the two-stage burner by using a SMPS. This experimental technique, along with measurements of flame temperature, gas-phase composition, and soot nanostructure and morphology, allowed for a better understanding of the processes of soot oxidation and soot oxidation-induced fragmentation.

In the case of alcohol and ester fuels, by increasing the fuel oxygen mole fraction, a reduced sooting tendency was observed; however, it resulted in a lower rate of soot oxidation that slowed soot burnout before exhaust, which could lead to higher net PM emissions. The study found that the soot oxidation rate was dependent on the initial soot nanostructure. Oxygen functionalities were not contributors to the changes in rates seen for changes in concentrations in n-butanol in n-dodecane. However, a more complete study is warranted for a comparison of the different fuels. The highest soot oxidative reactivity was found for the soot nanostructure with the minimum degree of orderliness. On the other hand, the lowest oxidative reactivity was observed for the soot with the nanostructure composed of large layer planes with either low or zero curvatures. A higher soot oxidation rate was observed for methyl decanoate/n-dodecane than n-butanol/n-dodecane fuel mixtures. As expected, conventional models (NSC, Neoh) did not fully capture differences in soot oxidation rates. The effect of soot nanostructure on the oxidative reactivity for these oxygenated fuels is consistent with other fuels, although further work is required to incorporate these effects into soot oxidation models.

Soot fragmentation has also been found important in soot oxidation. By the aid of image analysis, two main mechanisms of soot fragmentation were evaluated: i) oxygen diffusion in bridges between particles which then burn and break them apart, or ii) oxygen diffusion into a primary particle, causing internal burning, increasing particle porosity, and eventually breaking it apart. The results of image analysis demonstrated that bridge sites were formed by less-ordered nanostructure, suggesting a faster burning rate and aggregate fragmentation by this mechanism. A further analysis of the soot nanostructure yielded the particle tortuosity and the effective pore width, which was used in the effectiveness factor calculation to evaluate the feasibility of primary particle breakup by O_2 internal burning. The average tortuosity was 5.33±0.09 and pore width was 1.6±0.11 nm. The results showed the internal burning of particles would be possible for small particles up to 10 nm. It was shown that increasing the temperature and particle size, and decreasing O_2 partial pressure resulted in lower possibility of internal burning by O_2. In addition, experimental results showed that the rate of fragmentation was inversely proportional to the peak temperature. In addition, it was found that by decreasing the maximum mobility size from 130 nm to 80 nm, fragmentation vanished, implying that the onset of fragmentation depended on the presence of aggregates.

Soot oxidation-induce fragmentation massively produces ultrafine particles smaller than 10 nm. The characteristics of these ultrafine particles could be associated to a "nano-soot" rather than larger aromatics similar to PAHs, which are typically found during the formation process. This difference may result in different reactivities of these nano-ultrafine particles toward the human health and/or toward after-treatment systems which identifies areas of further study.

APPENDIX A

VAPORIZER

The vaporizer was designed for reliable liquid vaporization, specifically for vaporizing liquid hydrocarbons. Direct liquid injection vaporizer system overcomes the many limitations of conventional vapor delivery systems. Bubblers or vapor draw systems are difficult to start and stop, require very close control of temperature and pressure, and are inefficient at generating well controlled vapor mass flow. Furthermore, it is very challenging to determine precisely how much vapor mass is actually being delivered from a conventional vapor delivery system. In the direct injection vaporizer, the closed system helps to deliver all vaporized fuel to the burner. Figure A.1 shows a schematic of the vaporizer.

After being pumped by a syringe pump, the liquid fuel enters the chamber which is filled with stainless steel shot. Heat transfer occurs efficiently by liquid stream passing over heated balls. The stainless steel screen is used to hold the balls in the chamber. When the heated liquid undergoes a reduction in pressure by passing through an empty chamber, the flash vaporization occurs. Then, the vapored fuel goes into the manifold in order to be carried out with a stream of hot gas. The temperature in the vaporizer and along the feeding line is adjusted to avoid fuel condensation (500 F). The temperature of

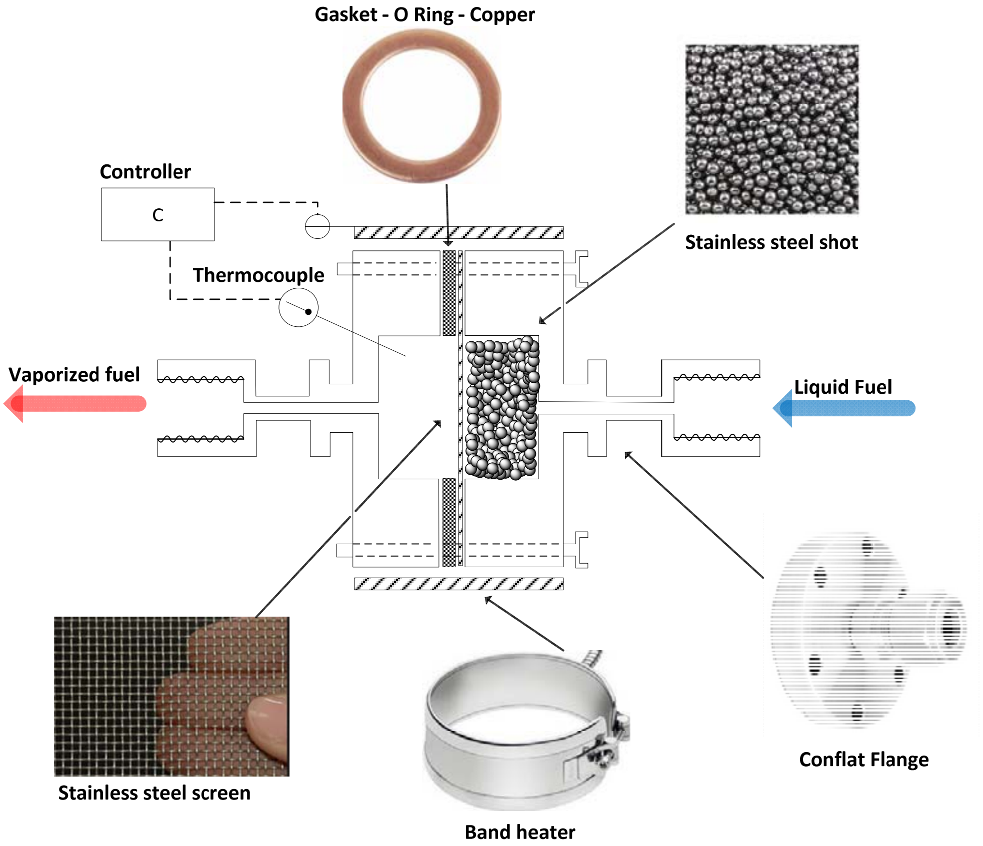

Figure A.1. The cross section of the vaporizer.

the vaporizer is maintained by using a band heater. The temperature inside the vaporizer is monitored with a thermocouple type K and its signal is transferred to a controller in order to control the temperature of the band heater.

In order to evaluate the performance of the vaporizer and to make sure that the composition of the fuel before and after the vaporization is similar, the following test was designed. Two fuel mixtures, 60% methyl decanoate/ 40% n-dodecane and 30% n-butanol/70%n-dodecane (molar basis) were tested. Each one was injected by a syringe pump into the vaporizer followed by the manifold. The temperature of the system was kept similar to the working temperature mentioned in Chapters 3 and 4 (500 F). The schematic of the setup is given in Figure A.2. For both fuel mixtures, the rate of fuel

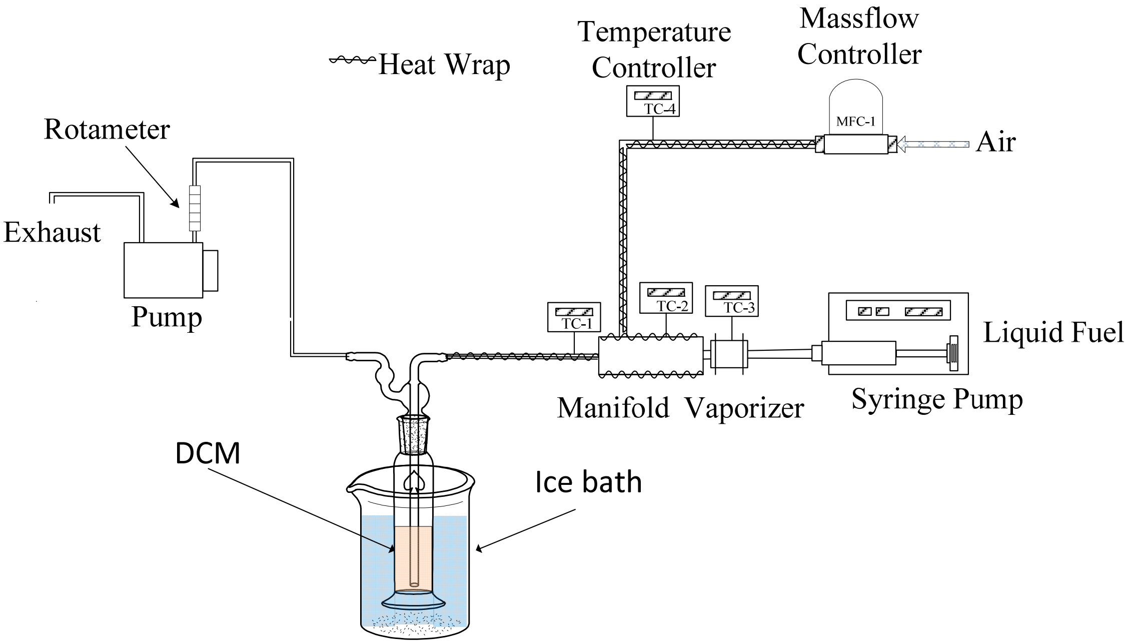

Figure A.2. The setup used to test the vaporizer.

injection was 80 ml/hr, and the air flowrate was 6.3 lit/min. A bubbler was used to re-condense the vaporized fuel into dichloromethane (DCM) as a solvent. Initially, 50 cm^3 of fuel mixtures was loaded into the syringe pump and 200 cm^3 of DCM was placed into the bubbler, surrounded by ice. A pump was used to create a negative pressure and to draw the mixture of air/fuel into the bubbler. When the fuel mixture was completely injected, a small portion of the DCM/fuel was taken for GC analysis.

In order to obtain calibration curves for each compound, a series of standard solutions were prepared and tested with GC to understand how the experimental observable value varies with the concentration. For this experiment, the points on the calibration curve should yield a straight line, and the slope and intercept of that line provide a relationship between absorbance and concentration. Calibration curves for three components, n-butanol, n-dodecane, and methyl decanoate, are given in Figure A.3.

Now, GC results obtained for vaporized fuel samples can be interpreted by using the

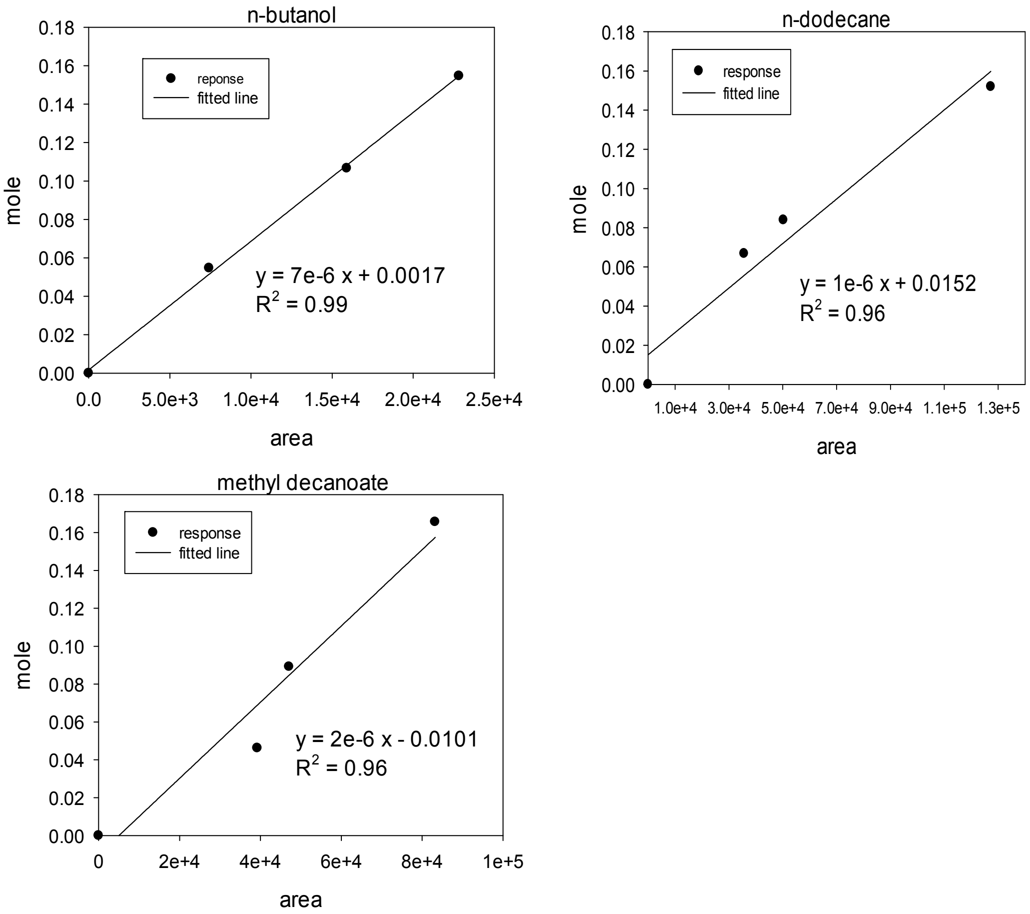

Figure A.3. The calibration curves for n-butanol, n-dodecane, and methyl decanoate

calibration curves. The absorbance of the unknown solution is then used with the slope and intercept from the calibration curves to calculate the concentration of the each compound. For the fuel mixture composed of 60%methyl decanoate / 40% n-dodecane (molar base), the following results were obtained.

The results given in Table A.1 show that the average concentration of the fuel after vaporization is, methyl decanoate: 62.66±4.6 % and n-dodecane: 37.33±4.6 %.

The errors are the result of uncertainty in the sampling process, limitations in the precision of measuring devices, GC measurements, and the vaporizer. This implies that the error of vaporizer may be less than the given error.

The same analysis was performed for the 30%n-butanol/70% n-dodecane, given in Table A.2. The results given in Table A.2 show that the average concentration of the parent fuel, after vaporization, is 28.57% for n-butanol and 71.42% for n-dodecane.

Table A.1. The GC results and the equivalent concentration for 60%methyl decanoate / 40% n-dodecane

Run#1				
Peak #	R.T.	Peak Area	Equivalent mole	**Molar %**
n-dodecane	4.953902	34522.03	0.04972	**40.66**
methyl decanoate	5.727666	41364.34	0.07263	**59.34**
Run#2				
Peak #	R.T.	Peak Area	Equivalent mole	**Molar %**
n-dodecane	4.915173	19210.53	0.03441	**34.02**
methyl decanoate	5.677032	38518.54	0.06694	**65.98**

Table A.2. The GC results and the equivalent concentration for the 30%n-butanol/70% n-dodecane

Run#1				
Peak #	R.T.	Peak Area	Equivalent mole	**Molar %**
n-butanol	1.725949	2856.345215	0.02169	**28.57**
n-dodecane	4.960862	38027.70313	0.05322	**71.42**

APPENDIX B

GAS TEMPERATURE ANALYSIS

When a thermocouple is inserted into a sooting flame, soot is driven to the thermocouple surface due to the thermophoretic gradient between the flame environment and the cold thermocouple surface. As the soot is deposited on the surface, the temperature reading drops continuously. A correlation of the transient response rate, due to the soot deposition, was used to estimate the local gas temperature. The temperature of the gases (Tg) was estimated using a quasi-steady energy balance at the junction between the depositing soot and the thermocouple suggested by McEnally et al. [1] as follows,

$$\epsilon_j \sigma T_j^4 = (k_{g0} \frac{Nu_j}{2d_j})(T_g^2 - T_j^2) \tag{B.1}$$

where T_j is the junction temperature, ϵ_j is the junction/bead emissivity, σ is the Stefan-Boltzmann constant, Nu_j is the junction Nusselt number, d_j is the junction diameter, and k_{g0} is the gas thermal conductivity.

The left-hand side of Eq. B.1 is the radiation heat loss per unit area, and the right-hand side is the convection heat gain per unit area. All flames studied in this work can be considered as low to nonsooting flames, based on the flat transient response of the thermocouple. In low-sooting flames, the parameters in Eq. B.1 are easily obtained. For d_j, the size of the clean junctions is used. k_{g0} is assumed constant and to be $6.54 \times 10^{-5}\, W/mK^2$, which is reasonable for combustion gases at high temperature [1]. The Nusselt number has been evaluated for similar systems in the range from 2.26 to 2.35 [2]. For B-type thermocouples, the emissivity was estimated as a function of the temperature as follows [3],

$$\epsilon_j = 0.1083Ln(T_j\ ) - 0.5644 \tag{B.2}$$

B.1 References

[1] D.C.S. McEnally, U.O. Koylu, L.D. Pfefferle, D.E. Rosner, Combustion and Flame 109 (1997) 701.

[2] A. Acrivos, T.D. Taylor, Physics of Fluids 5 (1962).

[3] C.A. Echavarria, Evolution of Soot Size Distribution during Soot Formation and Soot Oxidation-Fragmentation in Premixed Flames: Experimental and Modeling Study, University of Utah, 2010.

APPENDIX C

X-RAY PHOTOELECTRON SPECTROSCOPY (XPS)

X-ray photoelectron spectroscopy (XPS) was used to quantify the surface properties and bonding states to specify the role of oxygen-bond in the *n*-butanol. Results showed that the high-resolution C1s bond of oxidized carbon has a hump, which represents oxygen functional groups. By increasing the amount of oxygen surface functional group, this hump became more noticeable [1]. The large content of *O*-atoms is associated with the oxygenated functional groups bonded to the carbon on the soot surface. These functional groups, *C=O*, *C–OH*, and *COOH*, are generated as intermediates during the formation and partially oxidation of soot particles [2]. Peak deconvolution of the overlapping C1s identified the relative concentration of oxygenated surface functional groups. Figures C.1 and C.2 summarizes the carbon bond distribution of sp^2 and sp^3 and oxygen functional groups for two fuel mixtures. As seen in the figure, soot derived from both fuel mixtures had very similar surface functional groups. This is expected since *n*-butanol after dehydration, unimolecular decomposition, and dehydrogenation forms PAH precursors and oxygenated intermediates that finally oxidize to *CO* [3]. Therefore, from a kinetic point of view, the oxygen atoms in *n*-butanol should not contribute to changes in surface functionalities.

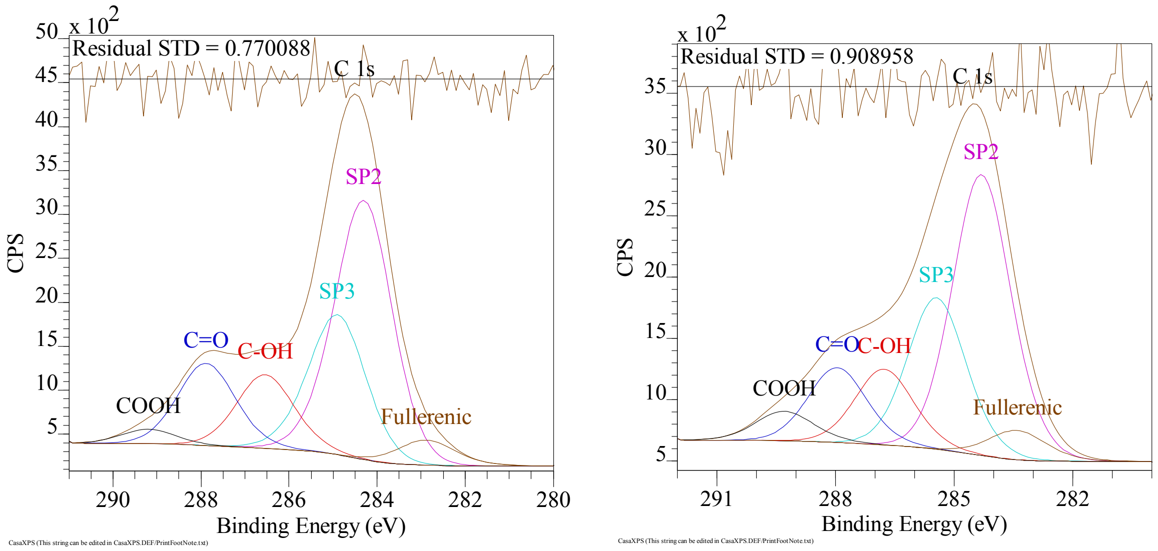

30% n-butanol / 70% n-dodecane before oxidation

60% n-butanol / 40% n-dodecane before oxidation

Figure C.1. XPS-spectrum in the C1s region including measured signal and fitted signal components for *C=O*, *C–OH*, *COOH,* SP^2, and SP^3 carbon chemical embedment

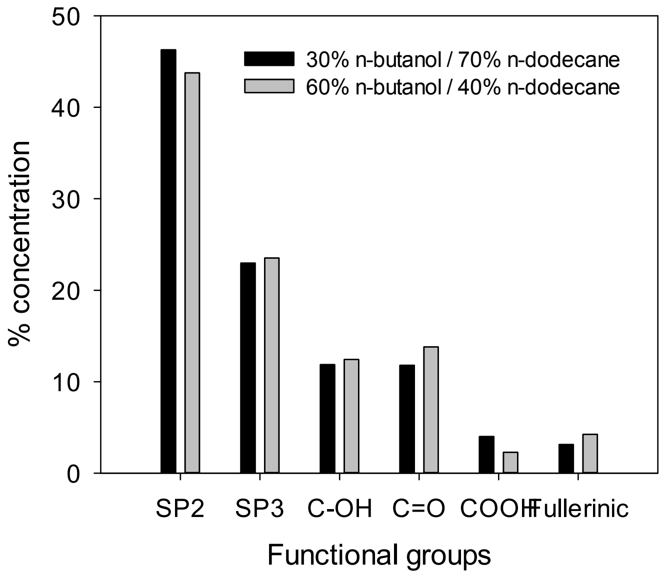

Figure C.2. Summary of functional group concentrations in both fuel mixtures

In order to determine the effect of water on the surface functionalities during the sampling, an experiment was designed. The NIST (SRM 2975) was used as the standard sample. 2 mg of sample was dispersed in 10 cc water by using an ultrasonic dispersion system for 4 hours. Then, the sample was stored over 24 hours. Similar to the methodology explained before, a piece of silicon wafer was placed in the bottom of the bottle. The vacuum system was used to evaporate the water. Finally, a dry piece of silicon wafer with a layer of soot deposited was used for XPS analysis. A standard sample was prepared by directly using NIST sample for XPS analysis. The results given in Figure C.3 show C1s spectrum with fitted components that look similar for both samples. Figure C.4 also shows the subsequent concentration of each functional group.

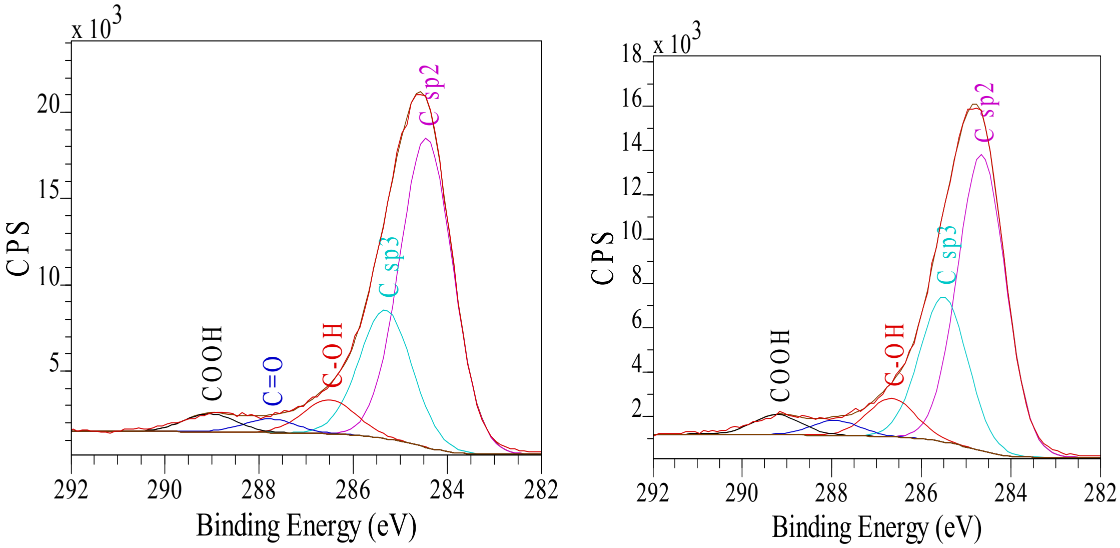

CasaXPS (This string can be edited in CasaXPS.DEF/PrintFootNote.txt)   CasaXPS (This string can be edited in CasaXPS.DEF/PrintFootNote.txt)

Figure C.3. XPS-spectrum of diesel soot in the C1s region including measured signal and fitted signal components for standard sample and the sample after water treatment. The left one shows the sample after water treatment and the right one is the standard sample.

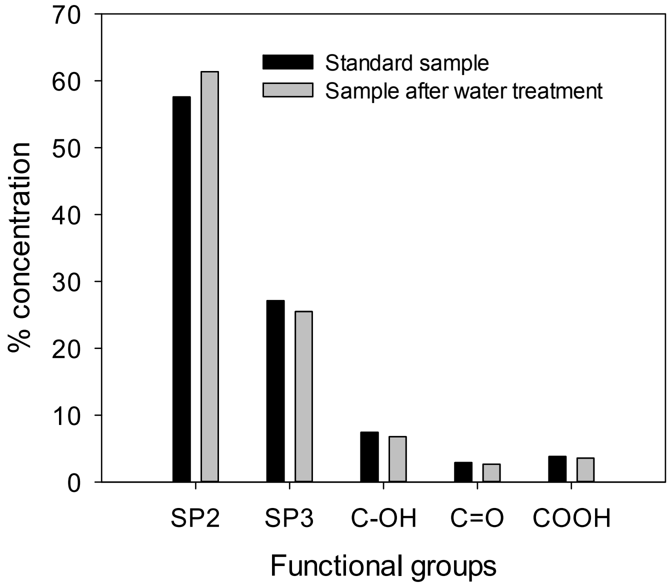

Figure C.4. Summary of functional group concentrations

C.1 References

[1] C. Esangbedo, A.L. Boehman, J.M. Perez, Tribology International 47 (2012) 194.

[2] L. Wang, C. Song, J. Song, G. Lv, H. Pang, W. Zhang, Proceedings of the Combustion Institute 34 (2013) 3099.

[3] C. Esarte, M. Abián, Á. Millera, R. Bilbao, M.U. Alzueta, Energy 43 (2012) 37.

[4] A.B. Palotas, L.C. Rainey, A.F. Sarofim, J.B. Van der Sande, P. Ciambelli, Energy & Fuels 10 (1996) 254.

[5] I.W. Chiang, B.E. Brinson, A.Y. Huang, P.A. Willis, M.J. Bronikowski, J.L. Margrave, R.E. Smalley, R.H. Hauge, The Journal of Physical Chemistry B 105 (2001) 8297.

[6] R.L. Vander Wal, V.M. Bryg, M.D. Hays, Journal of Aerosol Science 41 (2010) 108.

APPENDIX D

SOOT MASS CONCENTRATION

Soot mass concentration was calculated directly from the SMPS size and number concentrations assuming spherical particles following the methodology explained in Chapter 3. Figure D.1 shows the results for different methyl decanoate/*n*-dodecane blends.

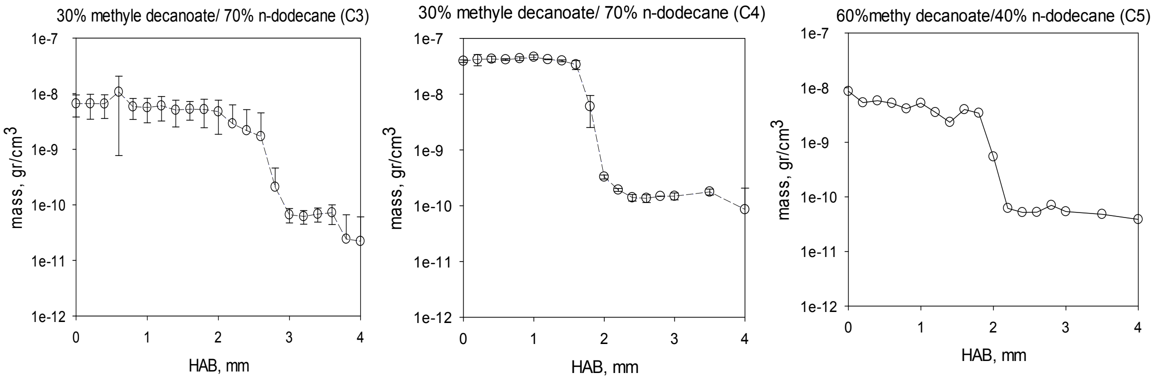

Figure D.1. Soot mass concentrations for different methyl decanoate/*n*-dodecane blends.

APPENDIX E

PARTICLE SIZE DISTRIBUTIONS

The following figure represents the PSDs at some selected HABs measured by SMPS for the ethylene flames in Chapter 6. PSDs are corrected for penetration efficiency into the probe orifice, diffusion losses during transport, and diffusion losses in the SMSP device.

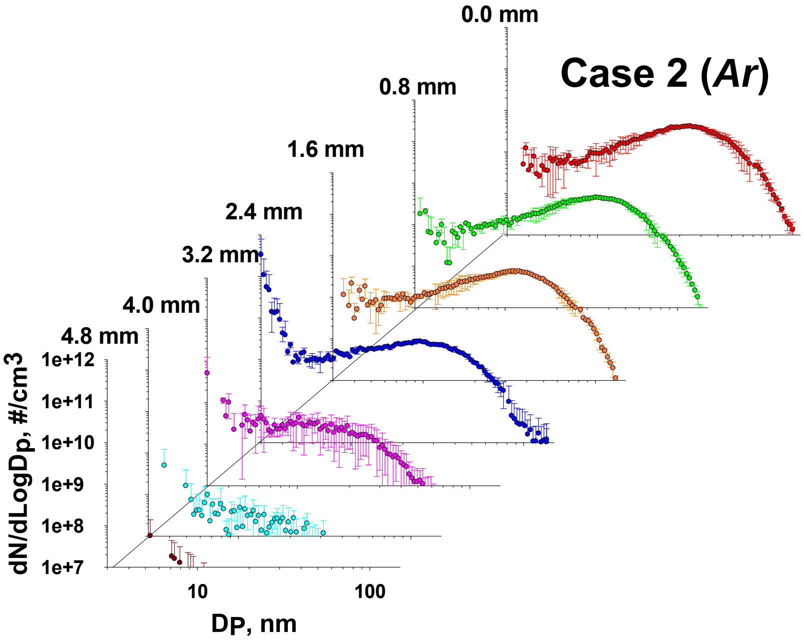
Case 2 (*Ar*)
0.0 mm
0.8 mm
1.6 mm
2.4 mm
3.2 mm
4.0 mm
4.8 mm
1e+12
1e+11
1e+10
1e+9
1e+8
1e+7
dN/dLogDp, #/cm3
10
100
Dp, nm

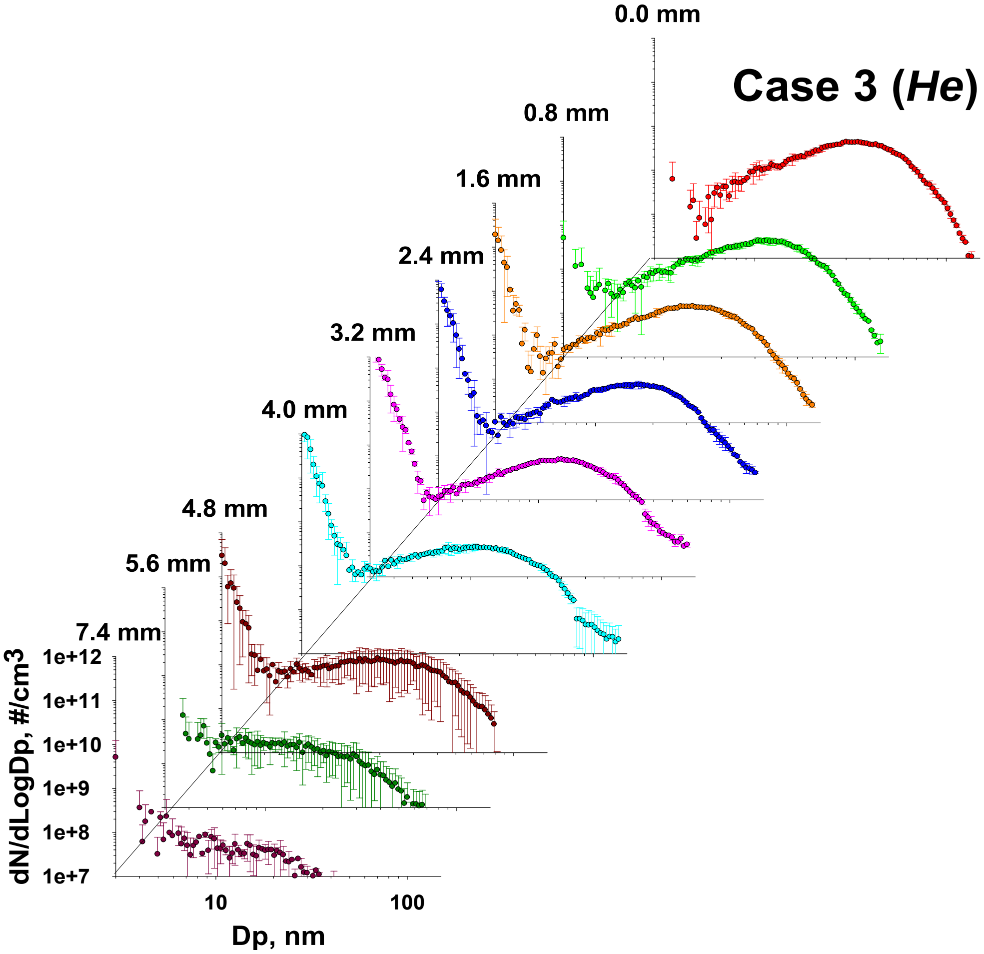
Case 3 (*He*)
0.0 mm
0.8 mm
1.6 mm
2.4 mm
3.2 mm
4.0 mm
4.8 mm
5.6 mm
7.4 mm
1e+12
1e+11
1e+10
1e+9
1e+8
1e+7
dN/dLogDp, #/cm3
10
100
Dp, nm

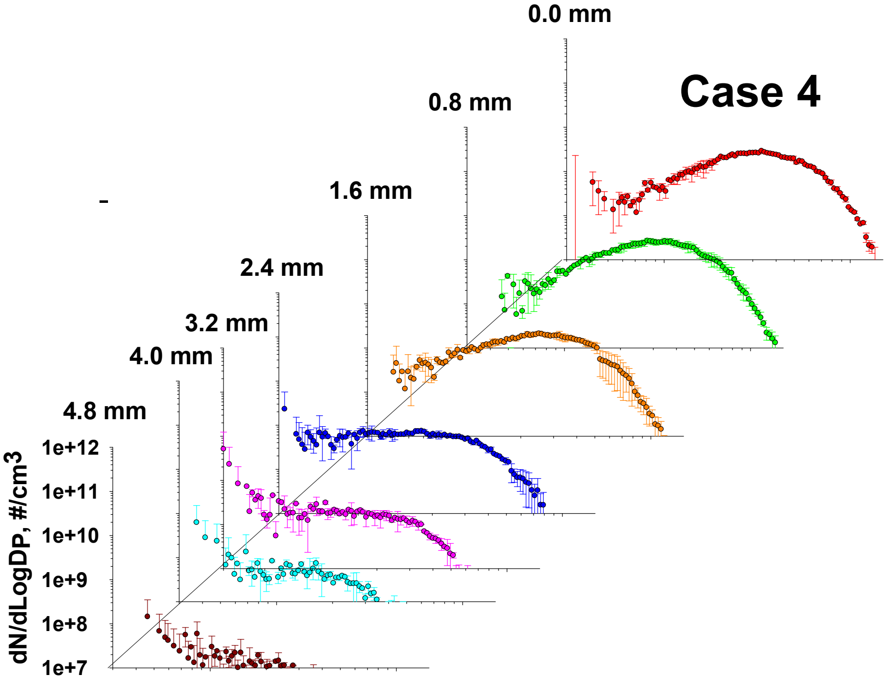
Case 4
0.0 mm
0.8 mm
1.6 mm
2.4 mm
3.2 mm
4.0 mm
4.8 mm
-
1e+12
1e+11
1e+10
1e+9
1e+8
1e+7
dN/dLogDP, #/cm3
10
100
DP, nm

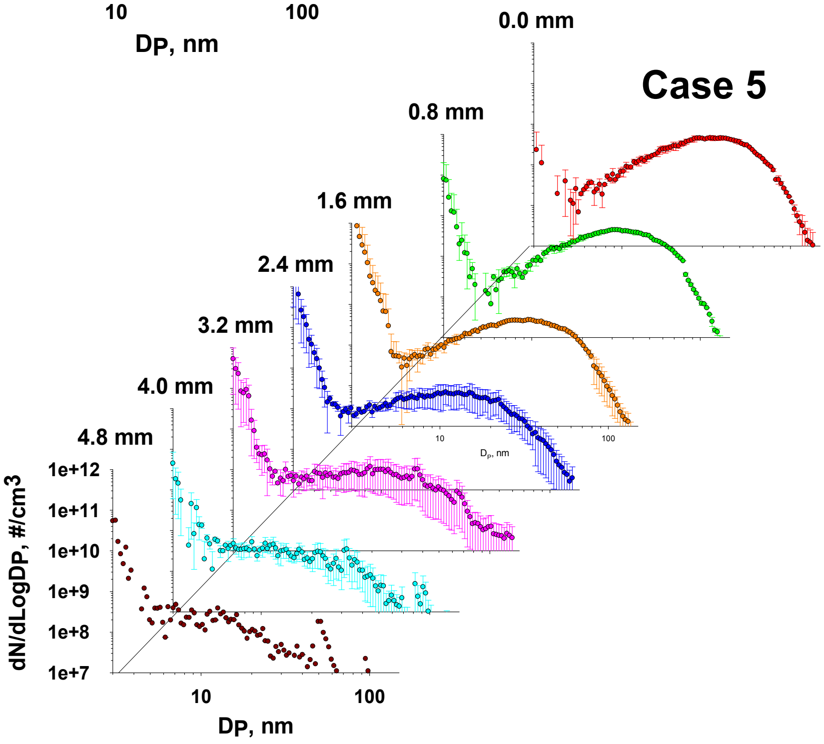
Case 5
0.0 mm
0.8 mm
1.6 mm
2.4 mm
3.2 mm
4.0 mm
4.8 mm
1e+12
1e+11
1e+10
1e+9
1e+8
1e+7
dN/dLogDP, #/cm3
10
100
Dp, nm
10
100
DP, nm

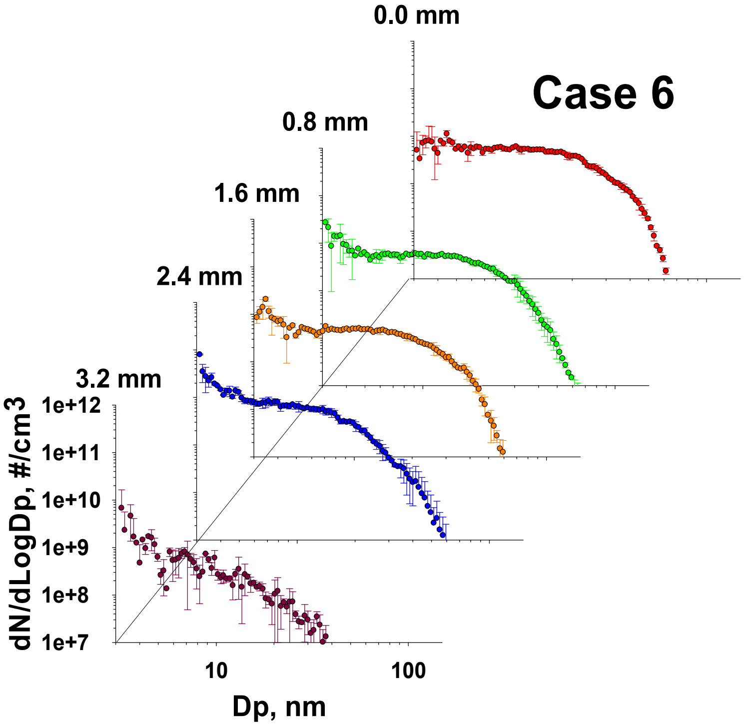

Figure E.1. PSDs at selected HABs for ethylene flames given in Chapter 6